2021-03-24

# Synthesis of Graphene for Wastewater Treatment by Adsorption and Electrochemical Regeneration

Lopez Pablos, Maria Fernanda

.

UNIVERSITY OF CALGARY

# Synthesis of Graphene for Wastewater Treatment by Adsorption and Electrochemical Regeneration

by

Maria Fernanda Lopez Pablos

A THESIS

SUBMITTED TO THE FACULTY OF GRADUATE STUDIES

IN PARTIAL FULFILMENT OF THE REQUIREMENTS FOR THE

DEGREE OF MASTER OF SCIENCE

GRADUATE PROGRAM IN CHEMICAL ENGINEERING

CALGARY, ALBERTA

MARCH, 2021

**Abstract**

Adsorption of pollutants in water is one of the most feasible techniques for water treatment. Several carbon materials have been used as an adsorbent, with graphene being one of the most attractive materials due to its high specific surface and conductivity. In this study, two electrochemically synthesized graphenes were used to investigate the adsorption capacity as well as the corrosion resistance of doped graphene. Electrochemically exfoliated nitrogen-phosphorous-doped graphene (EEG-N-P) showed a higher adsorption capacity compared to electrochemically exfoliated nitrogen-sulfur-doped graphene (EEG-N-S) resulting in a good adsorbent. However, EEG-N-S showed higher charge efficiency, with a shorter time required for electrochemical regeneration.

A regeneration efficiency of more than 100 % was achieved after the first cycle of regeneration using EEG-N-P; this was likely due to the creation of new adsorption sites, due to corrosion of the material. Accelerated corrosion tests and electrochemical techniques were used to analyze the oxidation resistance. Cyclic voltammetry (CV) provided information about the changes of the graphene surface before and after oxidation. A higher increase in gravimetric capacitance was obtained for EEG-N-P, according to CV data, and the calculated corrosion mass loss was greater for EEG-N-P than EEG-N-S based on potential step data. Therefore, EEG-N-S showed a higher corrosion resistance in the two different media used in these studies. Although air oxidation protection was provided by phosphorous doping, this doping did not protect the graphene from electrochemical corrosion.

The increase of electrode dimensions in electrochemical synthesis was also studied in this work. The effect of operating conditions including the current density, electrode area and pH on the yield, energy consumption and quality of graphene obtained were investigated. A higher yield was achieved in all cases with the use of larger electrodes. The pH was found to affect the yield and energy consumption, with bettery performance at higher pH.

Exfoliation with constant current and constant voltage was compared, resulting in a higher graphene doping and higher thermal stability when constant current was used. Different current densities were studied, showing a more cost-effective exfoliation when 100 and 200 mA $cm^{-2}$ was used compared to higher current density.

**Acknowledgments**

I would first like to thank my supervisor Professor Edward Roberts for his guidance, advice, understanding and help throughout this project.

I would also like to thank Ashutosh Singh and Damilola Momodu for sharing their knowledge and always being there to discuss and provide valuable ideas. Also to Derrick Bakuska, who was always curious about my research and contributes with great advice. Special thanks to all the research group members for their constructive feedback, their experience and knowledge that helped me grow professionally.

I wish to express my appreciation to my Examination Committee members Dr. Qingye Gemma Lu and Dr. Kunal Karan.

I express my gratitude to everyone who made this research possible, staff and students who put time and effort to help me to directly or indirectly.

In addition, I would like to thank my family for supporting me in every goal I set and for their unconditional love. Thank to my friends in Calgary who made this time funnier and became my family.

Lastly, I would like to acknowledge Natural Sciences and Engineering Research Council of Canada (NSERC) and Alberta Innovates for the financial support provided that made this research possible.

**Table of contents** Page

**Chapter 1. Introduction**……..... 1

*1.1 Adsorption as a water treatment option*…….. 1

*1.2 Corrosion of graphene*…… 1

*1.2.1 Accelerated corrosion tests of carbons*…….. 2

*1.3 Scale-up of graphene synthesis*…… 3

*1.4 Motivation/ scope/ research objective*…… 4

*1.5 Thesis structure/organization*…….. 4

**Chapter 2. Scale-up of Graphene Production by Electrochemical exfoliation** …….. 6

**2.1 Introduction**…….. 6

*2.1.1 Graphene synthesis techniques*…….. 6

*2.1.2 Electrochemical exfoliation of graphene*…… 8

**2.2 Experimental methods**…… 11

2.2.1 *Materials*…… 11

2.2.2 *Graphene synthesis from ammonium-based salts*…… 11

*2.2.3 Effect of current density on exfoliation*…… 13

*2.2.4 pH effect on exfoliation (yield) efficiency* …… 13

*2.2.5 Materials characterization*…… 14

**2.3 Results and discussion**…….. 15

*2.3.1 Comparison of the thermal stability of EEG-N-P and EEG-N-S at different current densities*…… 15

*2.3.2 Raman spectroscopy* …… 17

*2.3.3 X-ray photoelectron spectroscopy (XPS)* …….. 20

*2.3.4 Transmission Electron Microscopy (TEM)* …….. 23

*2.3.5 Constant current vs. constant voltage at small and large scales…* 25

*2.3.6 Effect of electrolyte pH on yield and energy ……* 27

*2.3.7 Yield and energy consumption at different electrodes areas……..* 29

*2.3.8 Yield and energy consumption in exfoliation at different current densities……* 32

**2.4 Conclusions** …… 34

**Chapter 3. Graphene adsorption and regeneration**…… 36

**3.1 Introduction**…….. 36

*3.1.2 Adsorption with graphene*…… 37

**3.2 Experimental methods**……. 38

*3.2.1 Adsorption*…….. 38

*3.2.2 Dye concentration analysis*…….. 39

*3.2.3 Adsorption capacity*…… 39

*3.2.4 Adsorption isotherms*…… 40

*3.2.5 Adsorption-Regeneration*…… 41

**3.3 Results and discussion**…… 43

*3.3.1 Adsorption mechanism* …… 43

*3.3.2* Regeneration mechanism…… 48

*3.3.3 Regeneration efficiency*…….. 49

**3.4 Conclusions**…….. 52

**Chapter 4. Corrosion of electrochemically exfoliated doped-graphene**…… 54

**4.1 Introduction**…… 54

**4.2 Experimental methods**…….. 58

*4.2.1 Materials*…….. 58

*4.2.2 Graphene synthesis*…….. 58

*4.2.3 Materials Characterization*…….. 59

*4.2.4 Accelerated corrosion experiments in acidic media*…… 60

*4.2.5 Accelerated corrosion experiments in neutral media*…… 64

**4.3 Results and discussion** …… 66

*4.3.1 Characterization of the materials*…… 66

*4.3.2 Accelerated corrosion tests in acidic media*…… 68

*4.3.2.1 Cyclic voltammetry*…… 68

*4.3.2.2 Corrosion calculations from chronoamperometry tests (potential steps)* …… 69

*4.3.2.3 Sample characterization before and after corrosion* …….. 72

*4.3.3 Accelerated corrosion tests in neutral media*…… 76

*4.3.4 Comparison between acidic and neutral media corrosion studies*…… 80

**4.4 Conclusions**…… 82

**Chapter 5. Conclusions and future work**…… 84

**List of figures**


Page

Figure 2.1: (a) Electrochemical exfoliation of graphite (b) Schematic representation of the proposed electrochemical graphite exfoliation mechanism…… 9

Figure 2.2: Schematic diagram showing the (a) 4 $cm^2$ electrodes area and (b) 16 $cm^2$ electrodes area for electrochemical exfoliation of graphite…… 12

Figure 2.3: Exfoliation of (a) EEG-N-S and (b) EEG-N-S at different current densities…… 15

Figure 2.4: TGA of graphene phosphate and sulfate at different current densities. (a) EEG-N-P (b) and (c) EEG-N-S (b) derivative weight loss of EEG-N-P and (d) derivative weight loss of EEG-N-S. …….. 16

Figure 2.5: $I_D/I_G$ ratios of EEG-N-P and EEG-N-S at different current densities… 18

Figure 2.6: Raman spectra of (a) EEG-N-P and (b) EEG-N-S synthetized using different current densities compared to unexfoliated graphite foil. …… 19

Figure 2.7: (a) to (d) TEM images of EEG-N-P, (e) diffraction patterns. …….. 24

Figure 2.8: (a) to (c) TEM images of EEG-N-S, (d) diffraction patterns. …… 24

Figure 2.9: current and voltage behaviour vs. time during exfoliation of EEG-N-P and EEG-N-S when (a) constant current of 200 mA cm-2 is applied (b) constant voltage of 10 V is applied at 16 $cm^2$ scale. …….. 25

Figure 2.10: TGA plot of EEG-N-P and EEG-N-S obtained with constant voltage exfoliation…… 26

Figure 2.11: Raman spectra of (a) EEG-N-S and (b) EEG-N-P obtained using constant voltage. …….. 27

Figure 2.12 energy consumption and yield of EEG-N-S exfoliated at different pH in small scale of 4 $cm^2$…….. 28

Figure 2.13: energy consumption and yield of graphene exfoliated with 0.1 M $(NH_4)_2SO_4$ and $(NH_4)_2HPO_4$ using constant current of 200 mA $cm^{-2}$ or constant voltage of 10 V, with an electrode area of 4 $cm^2$…….. 31

Figure 2.14: energy consumption and yield of graphene exfoliated with 0.1 M $(NH_4)_2SO_4$ and $(NH_4)_2HPO_4$ using constant current of 200 mA $cm^{-2}$ or constant voltage of 10 V, with an electrode area of 16 $cm^2$…… 31

Figure 2.15: energy consumption and yield of graphene exfoliated with 0.1 M

$(NH_4)_2SO_4$ and $(NH_4)_2HPO_4$ using different constant currents of 100, 200 and 300 mA $cm^{-2}$ at of 16 $cm^2$ electrodes area..... 32

Figure 3.1: schematic representation of adsorption-regeneration process or graphene..... 42

Figure 3.2: Adsorption isotherms of Methylene blue on (a) EEG-N-P and (b) EEG-N-S. Langmuir model was fitted to the data by non-linear regression..... 46

Figure 3.3: Adsorption isotherms of Methyl Orange on (a) EEG-N-P and (b) EEG-N-S. Langmuir model was fitted to the data by non-linear regression..... 46

Figure3.4: Regeneration time needed for both EEG-N-S and EEG-N-P..... 50

Figure3.5: Regeneration efficiency achieved in three cycles for EEG-N-S and EEG-N-P..... 51

Figure 4.1: Three-electrode cell configuration used for accelerated corrosion tests. ..... 60

Figure 4.2: Corrosion tests protocol, CV and potential steps..... 61

Figure 4.3: (a) TGA curve and (b) derivative weight loss of EEG-N-S and EEG-N-P in air. ..... 66

Figure 4.4: Raman spectra of (a) EEG-N-S and (b) EEG-N-P..... 67

Figure 4.5: CV before and after accelerated corrosion test (a) EEG-N-S (b) EEG-N-P in acidic media 0.5 M $H_2SO_4$ at a scan rate of 10 mV $s^{-1}$..... 68

Figure 4.6: Current versus time data obtained from potential steps for EEG-N-P ..... 70

Figure 4.7: SEM images of the glassy carbon surface with dropcasted EEG-N-P (a,c) before, and (b,d) after corrosion, at the same location..... 74

Figure 4.8: CV before and after accelerated corrosion test in 1 M $Na_2SO_4$ + 5 mM $K_3Fe(CN)_6$ electrolyte at 10 mV $s^{-1}$ (a) EEG-N-S (b) EEG-N-P..... 77

Figure 4.9: Nyquist plots from EIS in neutral media of (a) EEG-N-S (b) EEG-N-P performed at a fixed potential of 0.2 V vs. SCE, frequency range of 100 kHz - 10 mHz. Nyquist curve 1 was obtained after 6 cycles, curve 2 was after 12 cycles, and plot 3 was after 18 cycles of potential steps between 0.55 and 1.4 V vs. SCE. The inset plot shows a close-up of the Nyquist plot at the high frequency range..... 79

**List of tables**


Page

Table 2.1: comparison of techniques used for graphene production…… 7

Table 2.2: Elemental composition of EEG-N-P and EEG-N-S determined from XPS survey…… 22

Table 2.3: XPS peaks deconvolution data of EEG exfoliated at constant current in this study compared constant voltage exfoliated by Sharif *et al.* (2020)…… 23

Table2.4: conductivity of EEG films, exfoliated with constant current (200 mA $cm^{-2}$) in both ammonium sulfate and ammonium phosphate solutions…… 33

Table 3.1: Adsorption isotherm parameters based on the Langmuir and Freundlich equation for EEG-N-P and EEG-N-S using Methylene blue as contaminant. …… 47

Table 3.2: Adsorption isotherm parameters based on the Langmuir and Freundlich equation for EEG-N-P and EEG-N-S using Methyl orange as contaminant…….. 47

Table 4.1: surface area of EEG-N-P and EEG-N-S…….. 66

Table 4.2: Capacitance EEG samples obtained from CV (–0.2 to 0.85 V vs. SCE, 10 mV $s^{-1}$) before and after corrosion tests by potential steps in 0.5 M $H_sSO_4$…. 69

Table 4.3: charges passed for EEG-N-S and EEG- N-P during 18 potential steps between 1.4 and 0.55 V vs. SCE, accelerated corrosion experiments carried out in an acidic solution…… 72

Table 4.4: Raman $I_D/I_G$ ratio before and after corrosion studies in acidic media. 73

**Supporting information**


Page

Appendix 1: yield and energy consumption of exfoliation at small scale at 200 mA $cm^{-2}$ and different initial pH using 0.1 M $(NH_4)_2SO_4$..... 101

Appendix 2: yield and energy consumption of exfoliation at 16 $cm^2$ electrodes area..... 101

Appendix 3: yield and energy consumption of exfoliation at 4 $cm^2$ electrodes area..... 102

Appendix 4: Yield and energy consumption of graphene produced at large scale with different current densities..... 102

Appendix 5: XPS survey of EEG-N-P (blue) and EEG-N-S (red)..... 103

Appendix 6: (a) Sp2 deconvolution (b) P2p deconvolution..... 103

Appendix 7: (a) N1s peak deconvolution (b) functional groups..... 104

Appendix 8: (a) C1s peak deconvolution (b) functional groups..... 104

Appendix 9: Graphite foil with an exposed surface area of 16 $cm^2$ (a) before exfoliation (b) after exfoliation, incomplete exfoliation of graphite foil..... 105

Appendix 10: Graphite foil with an exposed surface area of 4 $cm^2$ (a) before exfoliation (b) after exfoliation. ..... 105

Appendix 11: (a) spectrum of Methylene blue dye (b) calibration curve of methylene blue used for adsorption tests..... 106

Appendix 12: (a) spectrum of Methyl orange dye (b) calibration curve of Methyl orange used for adsorption tests..... 106

Appendix 13: XRD of (a) EEG-N-S and (b) EEG-N-P before and after adsorption and anodic electrochemical regeneration..... 107

Appendix 14: XRD values of EEG-N-S and EEG-N-P before and after adsorption-regeneration test..... 107

Appendix 15: CV of EEG-N-S (a) before and (b) after accelerated corrosion test in neutral media at different scan rates..... 107

Appendix 16: EEG-N-S before and after accelerated corrosion in 1 M $Na_2SO_4$ at scan rate of 10 mV $s^{-1}$..... 108

Appendix 17: CV of EEG-N-P in acidic media 0.5 M $H_2SO_4$ with added

$K_3Fe(CN)_6$. …… 108

Appendix 18: CV before and after accelerated corrosion test in the absence of graphene, using acidic media 0.5 M $H_2SO_4$ at a scan rate of 10 mV $s^{-1}$…….. 109

Appendix 19: XRD of (a) EEG-N-S and (b) EEG-N-P before and after corrosion tests. …… 109

Appendix 20: XRD values of EEG-N-S and EEG-N-P before and after corrosion tests. …… 110

Appendix 21: calculated values of fitted EIS parameters using CNLS fitting method based on the equivalent circuit shown in figure 4.9 (a) after 1: 1 to 6 steps, 2: 7 to 12 and 3: 13 to 18 steps for EEG-N-S exposed to accelerated corrosion. …… 110

Appendix 22: calculated values of fitted EIS parameters using CNLS fitting method based on the equivalent circuit shown in figure 4.9 (b) after 1: 1 to 6 steps, 2: 7 to 12 and 3: 13 to 18 steps for EEG-N-P exposed to accelerated corrosion. …… 110

Appendix 24: charge passed for glassy carbon, EEG-N-S and EEG- N-P during 18 potential steps between 1.4 and 0.55 V vs. SCE, accelerated corrosion experiments carried out in an acidic solution…… 110

Appendix 23: Capacitance of glassy carbon and EEG samples obtained from CV (–0.2 to 0.85 V vs. SCE, 10 mV $s^{-1}$) before and after corrosion tests by potential steps in 0.5 M $H_sSO_4$. …… 110

**List of symbols and abbreviations**

| Symbol | Description | Unit |
|---|---|---|
| $\phi$ | Regeneration efficiency | **%** |
| $q_r$ | Adsorption capacity of the regenerated adsorbent | mg $g^{-1}$ |
| $q_i$ | Initial adsorption capacity | mg $g^{-1}$ |
| $Q_m$ | Highest amount of adsorption | mg $g^{-1}$ |
| $C_e$ | Final concentration | mg $L^{-1}$ |
| $C_o$ | Initial concentration | mg $L^{-1}$ |
| $K_L$ | Langmuir constant | L $mg^{-1}$ |
| $K_F$ | Freundlich constant | $mg^{1-1/n}$ $L^{1/n}$ $g^{-1}$ |
| $m$ | mass of adsorbent/graphene | g |
| $q_e$ | Equilibrium adsorption capacity | mg $g^{-1}$ |
| $V$ | Volume | L |
| $C_G$ | Gravimetric capacitance | F $g^{-1}$ |
| $A$ | Integrated charge from CV | A V |
| $\mu$ | scan rate | V $s^{-1}$ |
| $\Delta V$ | potential window | V |
| $Q_+$ | Anodic gravimetric charge | C $g^{-1}$ |
| $I$ | Current | A |
| $t_+$ | Duration of the potential holding at 1.4 V | s |
| $Q_-$ | Cathodic gravimetric charge | C $g^{-1}$ |
| $t_-$ | duration of the potential holding at 0.55 V | s |
| $Q_C$ | Corrosion gravimetric charge | C $g^{-1}$ |
| $t$ | Time required for 100% regeneration | s |
| Ш | Corrosion mass loss | % |
| $F$ | Faraday constant | C $mol^{-1}$ |
| $Mc$ | atomic mass of carbon | g $mol^{-1}$ |
| $Q_{C\ ECSA}$ | Corrosion gravimetric charge per real-time ECSA | - |
| $-Z''$ | Imaginary impedance | Ω |
| $Z'$ | Real Impedance | Ω |

| | | |
|---|---|---|
| $T$ | frequency independent constant | F $cm^{-2}$ |
| $\omega$ | angular frequency | - |
| $a$ | exponent | - |

# Chapter 1. Introduction

## *1.1 Adsorption as a water treatment option*

Carbon materials are used for several applications, including catalyst support in fuel cells and electrode in batteries and capacitors (Forouzandeh *et al.*, 2018), as well as water treatment using carbon as adsorbent. In water treatment application, various carbon materials such as activated carbon (AC), carbon nanotubes (CNT) and graphene have been employed as adsorbent (Li *et al.*, 2013). Particular attention is given to graphene as an adsorbent or graphene-based adsorbents due to its high surface area and affinity towards diverse organic contaminants (Ersan *et al.*, 2017).

Graphene has been used as an adsorbent in different studies; one of its advantages is the simple electrochemical regeneration that can be carried out after adsorption, therefore making graphene reusable for various cycles. Previous studies of graphene adsorption and electrochemical regeneration have shown that commercial graphene and graphene composite G-magnetite corroded after regeneration, and there was a loss of adsorbent due to oxidation (Sharif *et al.*, 2017; Sharif and Roberts, 2020). This degradation of the materials represents a difficulty in performing adsorption-regeneration cycles with the same efficiency as the fresh graphene.

In this work, the adsorption capacity of graphene was studied by using an anionic and cationic dye (methyl orange and methylene blue). The graphene was regenerated and the charge and regeneration efficiency were evaluated.

## *1.2 Corrosion of graphene*

Carbonaceous materials tend to experience carbon corrosion, which decreases the lifetime of the materials. The cause of the corrosion is the thermodynamic instability of carbon when it is exposed to oxidative conditions (Qiao *et al.*, 2018). Most studies on corrosion mechanism in carbon materials have focused on highly porous and disordered materials used as catalyst supports for fuel cell electrodes and supercapacitors. However, little work has been done to identify the corrosion mechanism in doped-graphene materials. Surface area and crystallinity are elements that have an impact on the oxidation rate on the carbon material (Forouzandeh *et al.*,

2015); thus, the corrosion resistance of graphene may be different from the amorphous carbon frequently studied.

One of the applications of graphene is water treatment, where graphene is used as an adsorbent. Graphene can also be regenerated and reused for several adsorption cycles. However, the corrosion of graphene during electrochemical regeneration is a challenge; this corrosion may decrease the number of graphene adsorption-regeneration cycles.

Electrochemical exfoliated graphene (EEG) doped with Phosphorous has shown high thermal stability according to TGA analysis; this type of doping protects the graphene from oxidation in air, hence there is an interest to study the corrosion resistance of this material compared to other electrochemically synthesized graphene. This EEG was studied in this work and its corrosion resistance was compared to the corrosion resistance of EEG doped with other heteroatoms.

### *1.2.1 Accelerated corrosion tests of carbons*

Corrosion experiments used different protocols to oxidize the carbon materials and study their resistance to corrosion. One of the corrosion protocols used was based on the fuel cell environment, where high potentials are reached during a start/stop operation (Forouzandeh *et al.*, 2018). These fuel cell-based corrosion studies have been performed to study mesoporous colloid imprinted carbon (CIC) (Forouzandeh *et al.*, 2018), Vulcan carbon (VC) (Forouzandeh *et al.*, 2018) and ordered mesoporous carbons (OMCs) (Forouzandeh *et al.*, 2015) by using a short accelerated corrosion protocol consisting of several potential steps and cyclic voltammetry (CV) in an acidic electrolyte.

Most of the studies were performed in an acidic environment, such as the analysis of Multiwall Carbon Nanotubes (MWCNTs) degradation (Yi *et al.*, 2015) and OMC (Pérez-Rodríguez *et al*., 2019). The mechanism of degradation was found to be different depending on the electrolyte used.

This work is focused on accelerated corrosion tests consisting of potential steps that expose the carbon to corrosion; cyclic voltammetry was carried out before and after the corrosion tests to observe changes on the carbon surface. The data obtained from cyclic voltammetry and potential steps was compared to determine the resistance to corrosion of EEG.

Electrochemical techniques were mainly used to study the corrosion resistance of the two different EEG using two different electrolytes. Some characterization was also carried out to better understand the mechanism of graphene corrosion.

*1.3 Scale-up of graphene synthesis*

Studies on scale-up of electrochemical anodic graphene exfoliation are needed in order to reach a mass production and understand the main parameters that have an effect on exfoliation process.

Few studies have focused on the scale-up of a reactor and the main parameters to take into account when a larger scale is needed. Achee and colleagues (2018) proposed the use of graphite flakes in order to produce exfoliated graphene and showed results from a prototype reactor. Another study used several anodes and cathodes in order to produce greater amount of graphene (Yang *et al.*, 2015). However the study of important parameters on for scale-up such as current density or cell voltage, as well as the quality of graphene obtained by changing these parameters has not been the objective of these studies.

In this study two different electrode areas were used for electrochemical exfoliation of graphene in a batch reactor. The yield, energy consumption and graphene obtained were compared. The exfoliation with both constant current and constant voltage was carried out. In addition, different current densities were applied during exfoliation, and the obtained material was characterized. The impact of pH is also discussed in this study, mainly focused on the yield and energy consumption.

*1.4 Motivation/ scope/ research objective*

- Up-scaling of the electrochemical graphene synthesis process, evaluating parameters such as constant current density compared to constant voltage, pH and various current densities.
- Evaluate properties of the graphene obtained when different current densities were used for electrochemical exfoliation.
- Evaluate energy consumption and yield variations at 4 $cm^2$ electrodes area and 16 $cm^2$ electrodes area.
- Analysis of the adsorption capacity using cationic and anionic dyes and regeneration of electrochemical exfoliated graphene.
- Study the corrosion resistance of two different electrochemically exfoliated doped- graphene by using various electrochemical techniques.

*1.5 Thesis structure/organization*

The thesis is separated into chapters, containing introduction, experimental methods, results and conclusions. The chapters contain the following topics:

Chapter 1. Introduction of graphene applied as an adsorbent for water treatment and regeneration. Corrosion/oxidation of graphene and techniques frequently used for corrosion studies of different carbons. Lastly, different synthesis of graphene commonly used and scale-up.

Chapter 2. Includes the process of the anodic electrochemical exfoliation of graphene using different electrodes area, methodology followed for the synthesis, evaluation of different parameters and several characterizations of the material. Analysis of the yield and energy consumption is also included in this chapter.

Chapter 3. Explains the adsorption tests performed using graphene powder, adsorption capacity and regeneration efficiency of electrochemically exfoliated graphene Nitrogen-phosphorous-doped (EEG-N-P) and electrochemically exfoliated graphene Nitrogen-sulfur-doped (EEG-N-S).

Chapter 4. Presents the results of corrosion resistance comparison between the two different graphene used and their electrochemical properties. Two different methods of corrosion studies are presented using different electrolytes. Characterization of graphene before and after corrosion is presented.

Chapter 5. This section provides a summary of the work that has been presented and main contributions, suggestions for future work are also included in this section.

# Chapter 2. Scale-up of Graphene Production by Electrochemical Exfoliation

## 2.1 Introduction

Graphene is a two-dimension material formed by $sp^2$ carbon hexagon networks (Dresselhaus *et al.,* 2010) with adjacent carbon atoms attached together by covalent bonds. This carbon material has exceptional electrical conductivity, mechanical strength (Roscher *et al.*, 2019), thermal conductivity, and tensile strength (Hack *et al.*, 2018). Graphene can be used for many applications including water treatment, batteries and super capacitors (Yu *et al.*, 2015).

### *2.1.1 Graphene synthesis techniques*

Conventional methods for graphene synthesis include: Hummers' method, being one of the most widely used for large scale production (Hack *et al.*, 2018); Chemical Vapor Deposition (CVD) involving growth of graphene on metals such as Cu and Ni (Yang *et al.*, 2019); mechanical exfoliation (Dresselhaus *et al.*, 2010); and electrochemical exfoliation (Momodu *et al.*, 2021), used in this work.

Each technique has their own advantages and disadvantages; table 2.1 presents a comparison between the different techniques commonly used for graphene exfoliation. CVD requires high temperature and sacrificial metal, chemical exfoliation by Hummer's method is a good option to produce Graphene oxide (GO), but it requires a further reduction in order to remove oxygen functional groups and recover the properties of graphene; these characteristics of the methods for exfoliation prevent the production of graphene from reaching a cost-effective mass production (Parvez *et al.*, 2014). The graphene production method also influences the amount and nature of defects in graphene, which influences the properties of the graphene for different applications (Eckmann *et al.*, 2013).

Table 2.1: comparison of techniques used for graphene production

| Technique for graphene production | Advantages/ strengths | Disadvantages/ weaknesses | Reference |
|---|---|---|---|
| Chemical Vapor Deposition (CVD) | ●Large-area ultrathin 2D material is obtained.<br>●Crystalline 2D nanomaterial with flexible thickness and size. | ●Expensive<br>●Requires high temperature and high vacuum<br>●Sacrificial metal is needed | (Yang *et al.*, 2019) (Khan *et al.*, 2017) (Zhang *et al.*, 2013) |
| Mechanical exfoliation | ●Single layer graphene can be obtained from a highly oriented pyrolytic graphite cristal. | ●Low production yield<br>●Poor control on size, shape and thickness of the exfoliated nanosheets<br>●Requires a substrate to support the nanosheets. | (Khan *et al.*, 2017) (Novoselov *et al.*, 2005) |
| Electrochemical exfoliation | ●Cost-effective<br>●Produce relatively high-quality, functionalized graphene.<br>●High yield.<br>●Can be carried out under ambient conditions.<br>●Environmental friendly | ●Not possible to control the homogeneous size and layer distribution of the exfoliated Nanosheets<br>●Anodic exfoliation may results in unwanted oxidation that can disrupt the sp2-hybridized carbon network of graphite. | (Khan *et al.*, 2017) (Zhong *et al.*, 2015) (Abdelkader *et al.*, 2015) |
| Hummer's method | ●Large scale production | ●Requires a further reduction in order to remove oxygen functional groups and recover the properties of graphene.<br>●High oxygen content. | (Hack *et al.*, 2018) (Allen *et al.*, 2010) |

Electrochemical exfoliation of graphite is considered to be a clean process because no removal of spent chemical oxidants is needed after exfoliation (Yu *et al.*, 2015). It is a cost-effective technique that can produce relatively high-quality, functionalized graphene. This technique is promising for large scale production as it produces high yield, it is cost effective (Zhong *et al.*, 2015), which is important for scale-up purposes (Yu *et al.*, 2015).

Zhong and coworkers investigated some challenges for mass production of graphene focusing on wet chemical processes (Zhong *et al.*, 2015). Their analysis included the production of graphene by electrochemical exfoliation; irregular exfoliation and electrical connectivity to graphite were two challenges identified for this technique.

An electrochemical cell (~20 x 30 cm) was evaluated for exfoliation with additives in the electrolyte, using more than one graphite foil as anodes (Yang *et al*., 2015). A continuous exfoliation with a prototype flow-through reactor was proposed using graphite flakes by (Achee et al., 2018).

### *2.1.2 Electrochemical exfoliation of graphene*

The mechanism of electrochemical exfoliation will change depending on the potential applied; exfoliation can be carried out under anodic (positive) or cathodic (negative) potentials. In anodic exfoliation, the bulk material is oxidized when a positive potential is applied; as a result negatively charged ions from solution will start to intercalate into the layers of graphite (Khan *et al.*, 2017), this will increase the interlaying spacing and exfoliation will happen. The opposite happens in cathodic exfoliation where the cations intercalate between the negatively charged graphene layers; as the cations introduce more, they cause the expansion of the interlayer spacing (Yang *et al.*, 2013).

Anodic graphite exfoliation (figure 2.1) is known to be the most frequently used of the electrochemical exfoliation techniques as a result of its high efficiency of exfoliation related to a better intercalation and expansion compared to cathodic exfoliation (Yu *et al.*, 2015). In addition, anodic exfoliation can be accomplished in short times, even minutes (Paredes and Munuera, 2017). On the contrary, cathodic exfoliation approaches generally require longer intercalation times of several hours (Yang *et al.*,

2016) and sonication treatment in proper solvents of more than 10 hours has been used to complete exfoliation (J. Wang *et al.*, 2011).

Besides, anodic exfoliation is highly versatile, electrolytes and concentration can be varied, additive can also be used. This gives opportunities to adjust the graphene characteristics during exfoliation (Paredes and Munuera, 2017).

The attention given to anodic exfoliation as a production technique possible to industrial scale-up is caused by the graphene nanosheets with a quality close to pristine graphene that can be achieved, despite of the oxidizing conditions. In addition, doping and functionalized graphene can be produced by using anodic exfoliation, making this method attractive for graphene production (Paredes and Munuera, 2017).

For this reason, this study will focus on anodic electrochemical exfoliation and results of studies using this technique. The mechanism of the anodic electrochemical exfoliation process is illustrated in in figure 2.1.

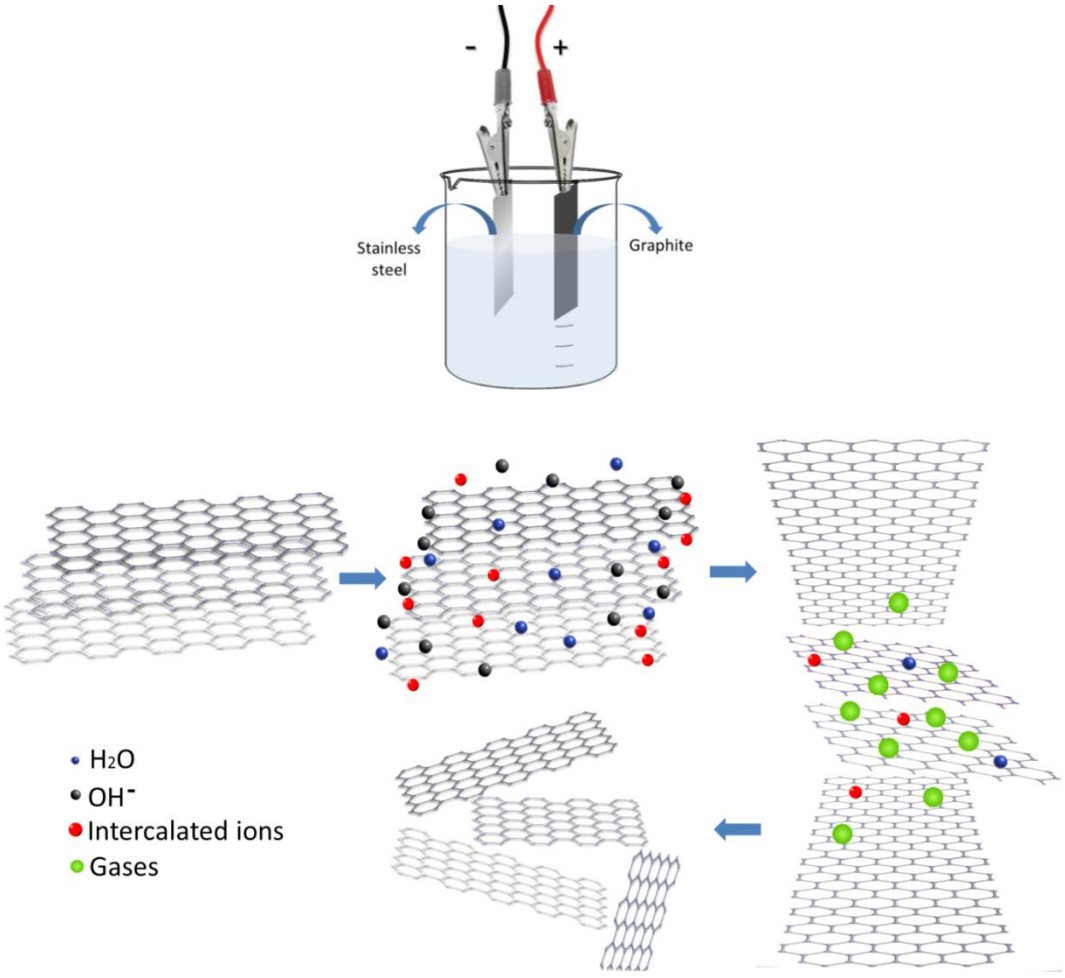


Figure 2.1: (a) Electrochemical exfoliation of graphite (b) Schematic representation of the proposed electrochemical graphite exfoliation mechanism (Parvez *et al.*, 2014).

When constant current or bias voltage is applied, the oxidation of water at the cathode creates hydroxyl ions ($OH^-$) in solution; these ions attack the edges of the graphite sheet and grain boundaries (Parvez *et al.*, 2014). Oxidation occurs at the edges and grain boundaries, expanding the graphene layers; some ions, such as sulfate, start to intercalate inside the graphene layers along with associated water molecules. Oxidation of water produce gas that is observed during exfoliation; these gas production can have enough force to separate the graphene layers exfoliating the graphite to produce graphene (Parvez *et al.*, 2014).

Graphene particles formed during the exfoliation process may remain suspended at the top of the solution due to the attachment of generated gas bubbles such as $O_2$ and $CO_2$ (Ali, 2019). A study of the gases produced during anodic exfoliation using 1 M $(NH_4)_2SO_4$ as electrolyte found $H_2O$ vapour, $N_2$, and $O_2$ as well as CO and $CO_2$ as a result of electrochemical oxidation of the graphite electrodes (Lou *et al.*, 2016).

The effect of the salt concentration in the electrolyte has also been studied using anodic electrochemical exfoliation. A low concentration of 0.01 M showed a low yield of less than 5 wt% due to low availability of ions in solution, while the yield also decreased to below 50 wt% at high concentrations of 3 to 5 M due to lower water content that is needed to produce $OH^-$ ions. The optimum salt concentration was found to be around 0.1 M at an applied cell voltage of 10 V with a$(NH_4)_2SO_4$ electrolyte (Parvez *et al.*, 2014).

Different electrolytes have been used to exfoliate graphite, including $(NH_4)_2SO_4$ , $Na_2SO_4$, $K_2SO_4$, $NH_4Cl$, $NaNO_3$ and $NaClO_4$, salts (Parvez *et al.*, 2014). It has been found that salts that contained the anions $NO_3^-$, $ClO_4^-$, and $Cl^-$ did not exhibit effective exfoliation, while salts containing sulfate ions showed high exfoliation efficiency, thin graphene sheets were obtained in less than 5 minutes. Different graphite sources have been employed in other studies such as graphite flakes, graphite rod, pencil core (Ali, 2019), and graphite foil (Momodu *et al.*, 2021).

In the present study, $(NH_4)_2SO_4$ and $(NH_4)_2HPO_4$ were used as electrolytes for electrochemical exfoliation method with a concentration of 0.1 M. In this chapter, we aim to investigate the scale up of the electrochemical exfoliation for production of

graphene based on the laboratory batch protocol as there are very few studies on scale-up of graphene production. Constant voltage is commonly used in electrochemical exfoliation studies. However, constant current is rarely mentioned. The fact that constant voltage is used makes scale-up difficult as the anode conditions are dependent on the arrangement of the electrodes, such as electrode gap and electrode size. On the contrary, by using constant current different sizes of electrodes can be used with one current density and studies will be comparable. Constant current or chronopotentiometry is simple and requires less operation considerations (Abdelkader *et al.*, 2015).

In this study, constant current is used and different current densities were applied to evaluate the defects produced in graphene and energy efficiency of the exfoliation process, and therefore define the best quality graphene and cost-effective graphene protocol.

## 2.2 Experimental methods

### 2.2.1 *Materials*

All chemicals were used as received without further purification. Deionized (DI) water was used for the preparation of the aqueous electrolytes, graphite foil ($5 \times 1$ $cm^2$, 0.05 cm thick, 99.8% purity, metal basis) was purchased from Alfa Aesar, manufactured by Thermo Fisher Scientific Chemicals, ammonium sulfate $(NH_4)_2SO_4$ 99.5% purity and ammonium phosphate $(NH_4)_2HPO_4$ 99-100% purity were purchased from VWR Canada.

### 2.2.2 *Graphene synthesis from ammonium-based salts*

Electrochemical exfoliated graphene (EEG) was synthesized via a one-step exfoliation technique using two different aqueous electrolytes composed of 0.1 M ammonium sulfate $(NH_4)_2SO_4$, and 0.1 M ammonium phosphate $(NH_4)_2HPO_4$.

For the laboratory scale synthesis figure 2.2 (a), graphite foil with an exposed area of 4 $cm^2$ was used as the anode, and a stainless steel grade 316 was used as the cathode (4 $cm^2$). The electrodes were immersed in 100 ml of electrolyte solution. The separation distance between the cathode and anode was fixed at 1.5 cm. The time required for complete exfoliation was recorded for each electrolyte. Constant current and constant

voltage were employed for exfoliation. The conductivity of the solution was measured with a conductivity meter that was introduced in the solution until the conductivity value was stable.

The laboratory-scale electrochemical exfoliation process was scaled-up to an electrode area of 16 $cm^2$, and the electrolyte volume was increased to 300 ml (figure 2.2 (b)). Initially electrode areas greater than 16 $cm^2$ were studied, however the exfoliation was poor and slow, and an area of 16 $cm^2$ was chosen for this study. The electrode separation was maintained at 1.5 cm in all cases.

For electrochemical exfoliation at a constant applied voltage of 10 V, the corresponding average current density was around 200 mA $cm^{-2}$. To investigate electrochemical exfoliation using a constant current, experiments were carried out at a range of current densities from 100 to 300 mA $cm^{-2}$. Constant voltage exfoliation using 10 V is also carried out for comparison.

The exfoliation experiments were repeated at least three times, and the error bars in the graphs were obtained from the standard deviation of these three repetitions.

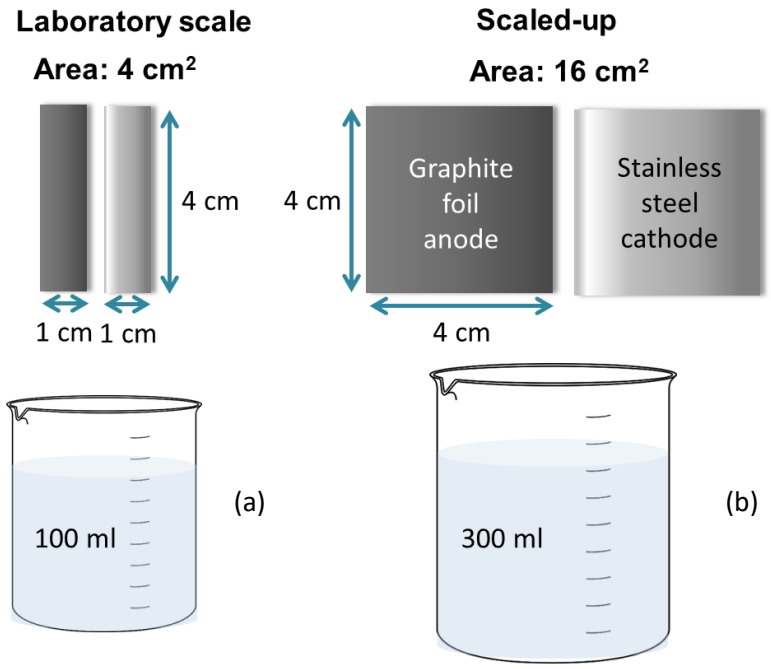


Figure 2.2: Schematic diagram showing the (a) 4 $cm^2$ electrodes area and (b) 16 $cm^2$ electrodes area for electrochemical exfoliation of graphite.

After complete exfoliation, the solution containing EEG and unexfoliated graphite was filtered and washed several times with DI water, using a vacuum filter with a 0.1 µm membrane filter in order to remove the remaining salts. The washed powder was re-dispersed in DI water, and sonicated for 30 minutes using a sonication bath.

Subsequently, the dispersed product was centrifuged (Avanti J-26S) at 2,000 rpm for 5 minutes to separate unexfoliated graphite from the EEG. The precipitate was discarded, and the supernatant was centrifuged at 20,000 rpm for 30 minutes to recover the graphene particles. Finally, the product was freeze-dried to obtain the final EEG powder form for characterization.
The yield was calculated as follows:

$$\text{Yield (\%)} = \frac{\text{Exfoliated material} - \text{precipitate}}{\text{Exfoliated material}} \times 100 \qquad (2.1)$$

Exfoliated material is the calculated graphene combined with graphite in suspension obtained after exfoliation; it is calculated as the initial weight of the graphoil before exfoliation minus the weight of the remaining not exfoliated graphoil.

Precipitate is the graphite-like material obtained after the sample was centrifuged. The subtraction of the precipitate weight from the exfoliated material gives an amount of ideal graphene weight obtained.

*2.2.3 Effect of current density on exfoliation*

A range of applied current densities from 100 to 300 mA $cm^{-2}$ were used to determine the effect of current density on the characteristics of the synthesized EEG.

*2.2.4 pH effect on exfoliation (yield) efficiency*

Ammonium sulfate $(NH_4)_2SO_4$ presented a pH of around 5.46 while Ammonium phosphate $(NH_4)_2HPO_4$ electrolyte presented a pH of 8.12. In order to study the effect of pH on the yield, the $(NH_4)_2SO_4$ electrolyte was adjusted to acid pH 4.04, and alkaline, pH 9.95 conditions.

*2.2.5 Materials characterization*

Sample characterizations were performed to determine the effect of varying current density on the material properties of synthesized EEG such as the nature of defects, morphology, and thermal stability.

Raman spectroscopy of the samples was carried out to confirm the successful exfoliation of graphite sheets into graphene and to determine the quality of the exfoliated material in terms of the defects content. A WITec Alpha 300R confocal micro-Raman instrument was used, operated with a 532 nm laser operated at 5.0 mW power.

The sample preparation involved dissolving the exfoliated graphene powder in ethanol, with a sonication step for 5 minutes to evenly disperse the flakes, followed by drop-casting of the suspension on a silicon wafer substrate. Raman mapping and imaging was carried out on a 5 × 5 µm area, with a 100x magnification microscope objective. The peaks obtained were deconvoluted and fitted to a Lorentzian function using the WITec Project 5 software.

X-ray photoelectron spectroscopy (XPS) was carried out to obtain information about the doping of heteroatoms and surface elemental composition on the exfoliated graphene samples. A Kratos Axis ULTRA photoelectron spectrometer (Kratos analytical limited, UK) was used.

Scanning Electron Microscopy (SEM) was used to observe the surface morphology of the EEG samples, using a Phenom ProX Desktop SEM system operated at 15 keV. A JEOL (JEM-ARM200CF Atomic Resolution) Transmission Electron Microscope (TEM) was used to obtain high magnification micrographs of the graphene flakes as well the associated selected area diffraction patterns (SAEDs) to estimate the number of layers.

Thermogravimetric analysis (TGA) was performed to study the thermal stability of the EEG samples. The TGA was carried out in air, with a temperature range of operation from 25 °C to 1000 °C and a heating rate of 10 °C $min^{-1}$.

The electrical conductivity of graphene was calculated from graphene films, a piece of the film thickness was measured at 10 kV using a Quanta FEG 250 (FEI) SEM with at

different spots in order to take an average thickness, a 4 probe method using a Loresta- GX MCP-T700 resistivity meter (Mitsubishi, Japan). Variations of thickness will have an impact on the measured conductivity. For this reason, three films of 3.7 cm diameter were prepared in order to obtain an average thickness of each graphene film when measuring the conductivity.

## 2.3 Results and discussion

### *2.3.1 Comparison of the thermal stability of EEG-N-P and EEG-N-S at different current densities*

Based on the data obtained for EEG synthesized at different current densities, a current density of 200 mA $cm^{-2}$ was selected for graphene characterization and for studying exfoliation at two different scales. This current density provided a more stable voltage over the exfoliation compared to the highest current density, and less time was required for exfoliation compared to 100 mA $cm^{-2}$ as can be seen in figure 2.3. According to this figure the synthesis of EEG-N-P requires shorter times and higher cell voltage were recorded compared to EEG-N-S.

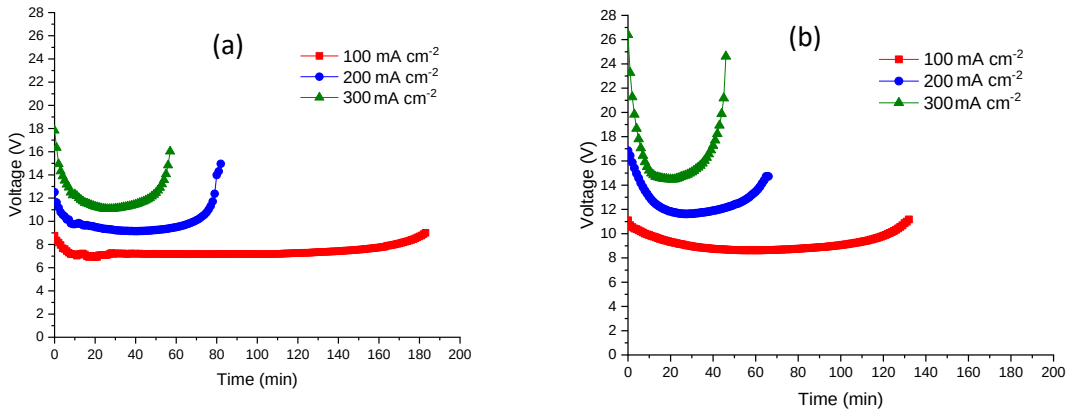


Figure 2.3: Exfoliation of (a) EEG-N-S and (b) EEG-N-S at different current densities

Slight differences in the thermal stability of the EEG-N-P figure 2.4 (c) were observed when they were prepared at different current densities, no clear trend is observed in the effect of current density on thermal stability. Compared to EEG-N-P, a more

significant variation in the thermal stability of EEG-N-S (b) was observed at different current densities. A decrease in thermal stability was observed when the highest current density of 300 mA $cm^{-2}$ was used. Figure 2.4 (b) and (d) shows the derivative of the curves, the weight loss related to different oxidation steps can be identified.

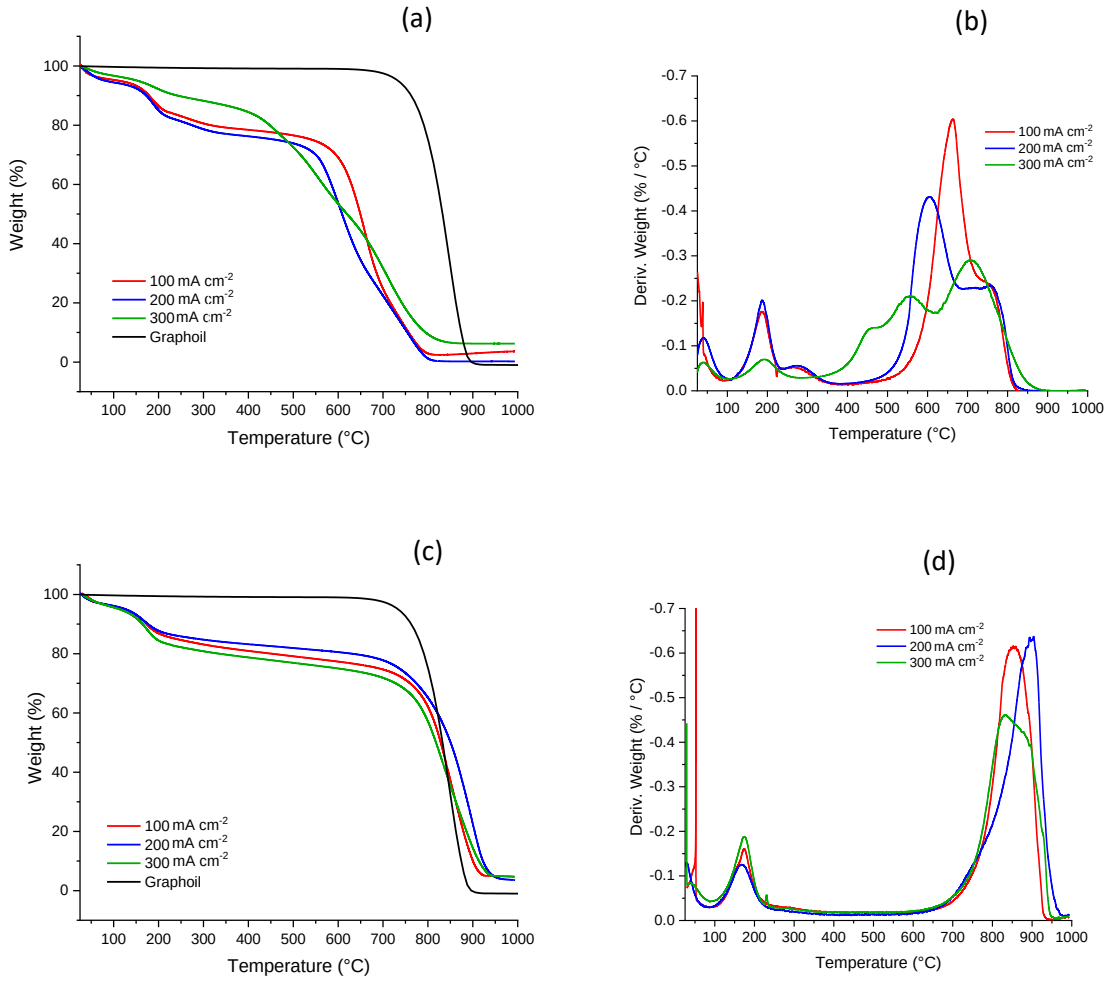


Figure 2.4: TGA of graphene phosphate and sulfate at different current densities. (a) EEG-N-P (b) and (c) EEG-N-S (b) derivative weight loss of EEG-N-P and (d) derivative weight loss of EEG-N-S.

The weight loss in different temperature ranges indicates the different functional groups in the graphene structure. The first zone from room temperature to around 100 - 120 °C is related to loss of water molecules adsorbed on the graphene (Ren *et al.*, 2011); from 120 °C until 300 °C the weight loss is related to oxygen functional groups that are not stable and can break down easily. The weight loss in the third zone from 300 °C to around 500 °C indicates the presence of more stable oxygen functional

groups like carbonyl and phenol, the last region from above 500 °C represents the breakdown of the carbon structure and mass loss due to pyrolysis (Chang *et al.*, 2012).

The curve (figure 2.4 (b)) shows a lower concentration of water and unstable oxygen functional groups in EEG at a current density of 300 mA $cm^{-2}$ compared to the other two lower current densities, this suggest that the increase of current density gives less defects or functional groups possibly due to poor exfoliation or fast exfoliation resulting in insufficient time for intercalation, and therefore bigger exfoliated particles.

It has been reported that when a high DC is used, the exfoliation process becomes more intense, this can cause incomplete exfoliation of graphite (Xue *et al.*, 2016). Low values of DC may also not be ideal for exfoliation, as it reduces the ionization of water molecules, slowing down the production of $OH^-$ ions known to be responsible for the attack of graphite flakes/foil at the grain boundaries and edges.

*2.3.2 Raman spectroscopy*

Raman spectroscopy was carried out to obtain structural information for the EEG samples. Figure 2.6 shows the Raman spectrum of EEG-N-S samples. The D peak (~ 1350 $cm^{-1}$) is caused by the breathing mode of six-atoms rings and is associated with the presence of defects in the graphene structure (Ferrari and Basko, 2013). The G peak (~1580 $cm^{-1}$) is related to the longitudinal optical (LO) phonon mode (Dresselhaus *et al*., 2010). The 2D peak (~ 2680 $cm^{-1}$) is due to a second-order Raman scattering by in-plane transverse optical phonons close to the boundary of the Brillouin zone (Roscher *et al.*, 2019). The ratio of intensities of the D and G peaks ($I_D/I_G$) provides information about the graphene quality and defects in the sample; it is often used to compare the amount of defects from different samples. In addition, $I_D/I_G$ ratio can be used to determine the in-plane crystallite size in the sample (Dresselhaus *et al.*, 2010).

The EEG samples (figure 2.5) showed $I_D/I_G$ ratios between 1.1 and 1.7, suggesting significant content of defects in the graphene structure. Some authors have reported a $I_D/I_G$ ratio of 0.25 for exfoliated graphene with sulfate salts and applying +10 V as cell voltage (Parvez *et al.*, 2014). A study of exfoliation with ammonium sulfate salts reported $I_D/I_G$ of 0.83 using 10 V as bias voltage and graphite rod (Y. Z.N. Htwe *et al.*,

2019). An $I_D/I_G$ ratio of 0.85 was obtained when ammonium sulfate was used as electrolyte and 1 A was applied to a 5 cm long graphite rod (Parvez *et al.*, 2016).

It can be difficult to make a distinction between the contributions of doping and other defects such as oxygen functional groups in the samples. Previous studies have reported that the doping of heteroatoms in the graphene structure, such as nitrogen, has shown an increase in the D peak intensity (Zafar and Ni, 2013). A study of carbon paper has also shown increasing intensity of the D band and consequently the $I_D/I_G$ ratio with nitrogen-doping (Singh *et al.*, 2019). The 2D peak can also be suppressed by surface defects found in few-layer wrinkled graphene (FLwG) (Kaniyoor and Ramaprabhu, 2012), where a small amount of doping has also shown to have an effect on the 2D peak (Zafar and Ni, 2013).

Figure 2.5 shows that graphene synthesized at 300 mA $cm^{-2}$ had the lowest $I_D/I_G$ ratio, validating the results of TGA analysis that indicate lower defects as a result of less oxygen functional groups; this lower ratio can also be related to a reduced amount of doped atoms in the graphene structure. Figure 2.6 shows the Raman spectra.

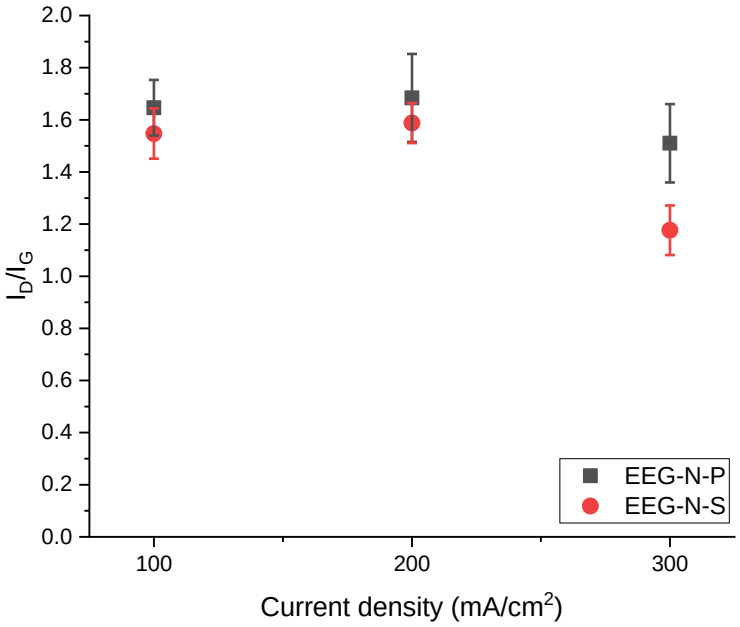


Figure 2.5: $I_D/I_G$ ratios of EEG-N-P and EEG-N-S at different current densities.

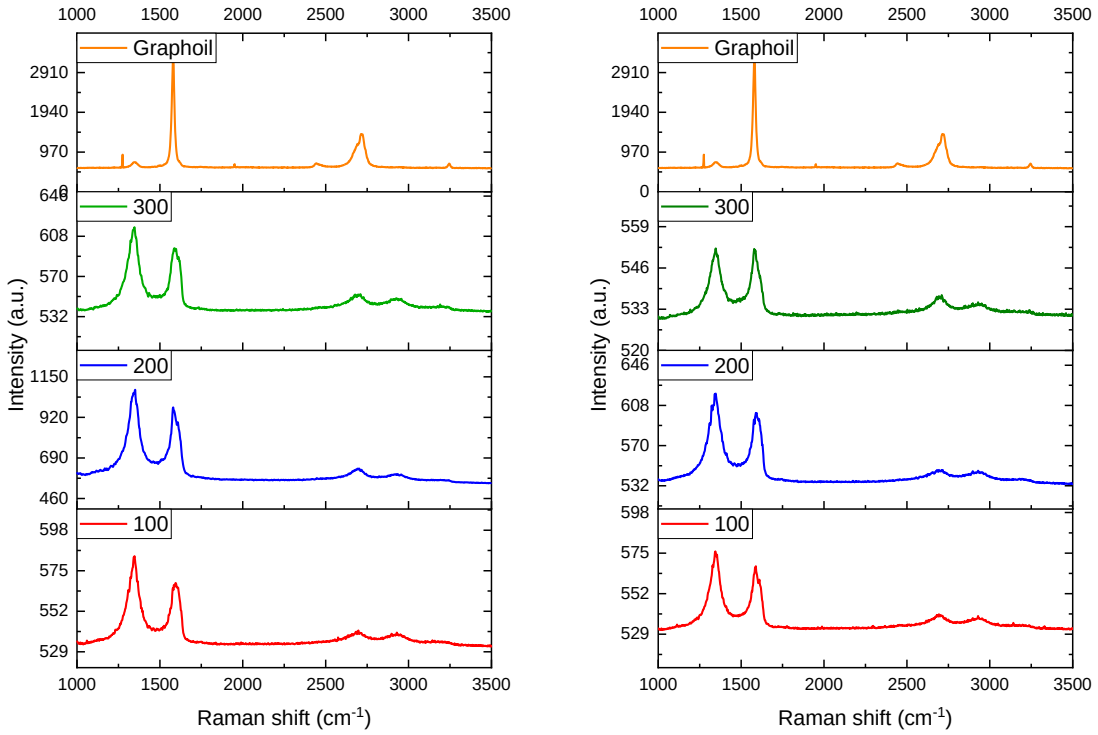


Figure 2.6: Raman spectra of (a) EEG-N-P and (b) EEG-N-S synthetized using different current densities compared to unexfoliated graphite foil.

The Raman spectra are consistent with the TGA data. For EEG-N-P, the $I_D/I_G$ ratio varies only slightly with current density, similar to the thermal stability observed from the TGA. In contrast, for EEG-N-S the $I_D/I_G$ ratio changed significantly with current density. The higher $I_D/I_G$ ratios in EEG-N-P at all currents can be related to the higher amount of doping, such as N-doping (Choi *et al.*, 2011).

It is clear that the electrolyte used for exfoliation played an important role in the characteristics of the graphene obtained. In addition, the current density also led to changes in the amount of defects and the stability when an ammonium sulfate electrolyte was used (EEG-N-S).

EEG synthesized with different salts, 0.1 M ammonium sulfate and ammonium phosphate were observed to have different stability based on the TGA data. EEG-P had a much higher thermal stability than EEG-S, which is related to doping of phosphorous in the graphene structure (Sharif *et al.*, 2020). For example, the sample weight is reduced to 50% of its initial weight at temperatures of 592 ± 21 °C and 818 ± 15 °C for

EEG-N-S and EEG-N-P respectively. The trends are consistent with a previous study showing thermal stability results of using the same electrolytes at constant voltage (Sharif *et al.*, 2020). However, a slightly lower thermal stability was found in the present study.

*2.3.3 X-ray photoelectron spectroscopy (XPS)*

XPS is a tool commonly used to characterize graphene materials. The analysis gives information about the atomic composition of the material as well as information about oxidative states of the elements in the material. The C/O ratio is obtained with this characterization technique. Therefore, the degree of oxidation of the sample can be evaluated (Ambrosi *et al.*, 2014). XPS is also used for graphene characterization to obtain information about the types of carbon and oxygen bonds (Y. Z.N. Htwe *et al.*, 2019).

Table 2.2 shows the composition of the EEG samples. It was found that both EEG-N-P and EEG-N-S were doped with nitrogen. The doping of heteroatoms has been previously reported when these salts were used during electrochemical exfoliation. Doping of nitrogen of up to 4.9 % has been achieved with 5M $NH_3{\cdot}H_2O$ and 1 M $(NH_4)_2SO_4$ electrolyte (Lou *et al.*, 2016) and graphene synthesized using constant voltage and 0.1 M $(NH_4)_2SO_4$ and $(NH_4)_2HPO_4$ electrolytes showed similar doping percentages (Sharif *et al.*, 2020). The carbon/oxygen ratios of the samples in this study were not significantly different, 3.8 and 3.67 for EEG-N-S and EEG-N-P respectively, and were similar to the ratios reported by Sharif et al. of 3.37 and 2.97 (2020). Similar C/O ratios of around 3.45 have been reported for anodic electrochemical exfoliated graphene when a phosphate buffer solution was used (Zeng *et al.*, 2011) and 3.42 when a 0.1 $(NH_4)_2SO_4$ electrolyte was used (Y. Z.N. Htwe *et al.*, 2019). A higher C/O of 4.98 was reported for electrochemically exfoliated graphene obtained in an $H_2SO_4$ electrolyte (Y. Z.N. Htwe *et al.*, 2019). The use of electrolyte combinations has shown a higher C/O ratio of 7.47 in N-doped graphene obtained by using a 5M $NH_3{\cdot}H_2O$ and 1 M $(NH_4)_2SO_4$ electrolytes with a cell voltage of 7.5 V (Lou *et al.*, 2016). Survey scan analysis shows the percentage of doping form the different heteroatoms (appendix 5) and percentages of oxygen content in graphene.

XPS data shows that there is significant doping of phosphorous, which is known to provide thermal stability to carbon. The XPS deconvolution can be found in appendix 6,7 and 8; table 2.3 shows the percentages of the bond types. According to the S2p deconvolution in of the samples, C-$SO_X$-C bonding is found in EEG-N-S, indicating that sulphate in the electrolyte was incorporated in the graphene during exfoliation with a concentration of 0.58% S. Co-doping of sulphur and nitrogen in carbon has shown a relatively greater performance for electrochemical activity when it is compared to doping with nitrogen alone, increasing the onset potential and the reactivity for oxygen reduction (Choi *et al.*, 2011).

In the case of P2p peak deconvolution (appendix 6 (b)), C-P (28.7%) and C-P-O (71.3%) bonding was found in EEG-N-P. This was expected as phosphate ions are present in the electrolyte during exfoliation, and as a result P was incorporated in the graphene structure. This type of bonding has been analysed when a C-$PO_3$ compound was present and it was found that they were able to survive temperatures higher than 1000 °C in air as they act as blocking sites (Wu and Radovic, 2006). Inhibition of catalytic oxidation was observed due to the effect of phosphorous doping where oxygen-containing P groups were found to block oxidation (Wu and Radovic, 2006).

The N1s peak deconvolution shows that nitrogen was incorporated in both graphene samples. The nitrogen content found in EEG-N-P was higher than EEG-N-S. Pyrrolic and quaternary N was found to be the dominant N configurations in the two samples, with percentages of pyridinic N around 10 to 15%. More pyrrolic groups (47.2%) were found on the EEG-N-S whereas EEG-N-P was found to yield more quaternary N functional groups (48.6%). These differences can be related to the differences in the exfoliation conditions.

Deconvolution of the C1s peak indicates a similar percentage of C=C bonding, 63.5% for EE-N-S and 64.6% for EEG-N-P. A greater composition difference was observed for the C-O bonds, with 31.1% for EEG-N-S and 27.5% for EEG-N-P. A minor change (0.1 %) was found related to the composition of C=O, O-C=O bonding between the two samples.

Compared to studies performed at constant voltage in a previous study of our group (Sharif *et al.*, 2020), samples exfoliated with $(NH_4)_2HPO_4$ electrolyte at constant current showed a higher doping of phosphorous, with around 0.6% higher P content than that observed for EEG-N-P prepared at constant voltage. Samples exfoliated at constant current with $(NH_4)_2\ SO_4$ showed almost twice as much doping of Sulphur as the samples exfoliated using constant voltage in the study carried out by Sharif et al. (2020).

The percentage of C=C carbon bonding were higher in both EEG-N-P and EEG-N-S exfoliated at constant current by approximately 6% compared to samples exfoliated using CV suggesting that the samples presented less oxidation.

Phosphorous doping was observed for the EEG-N-P at 1.29 wt% P, which is the main difference in composition between the two graphenes, while the C/O ratio was very similar. Therefore, it can be concluded that the stability is given by the doping of Phosphorus; this effect was expected and has been reported previously by our group (Roberts et al. 2020).

XPS data shows that a reaction of heteroatoms with graphene occurred resulting in different bonding. The mechanism of doping has been suggested to occur by redox reactions in aqueous solution, these reactions involve changes in the charge state of the participants (Pinto *et al.*, 2010). Nitrogen atoms are mainly incorporated into the graphene lattice through the interaction between nitrogen and groups containing oxygen, later rearrangement occurs (Long *et al.*, 2010; Wang *et al.*, 2012).

Table 2.2: Elemental composition of EEG-N-P and EEG-N-S determined from XPS survey.

| Element | EEG-N-S Weight (%) | EEG-N-P Weight (%) |
|---|---|---|
| C | 77.7 | 76.18 |
| O | 20.41 | 20.79 |
| N | 1.25 | 1.82 |
| S | 0.58 | - |
| P | - | 1.29 |
| C/O | 3.8 | 3.67 |

Table 2.3: XPS peaks deconvolution data of EEG exfoliated at constant current in this study compared constant voltage exfoliated by Sharif *et al.* (2020).

| Sample | N1s | | | C1s | | | P2p | |
|---|---|---|---|---|---|---|---|---|
| | Pyridinic | Pyrrolic | Graphitic | C=C | C-O | C=O/ O-C=O | P-C | C-P-O |
| EEG-N-S constant current | 14.8 | 47.2 | 38.1 | 63.5 | 31.1 | 3.6 | - | - |
| EEG-N-P constant current | 10.1 | 43.2 | 46.8 | 64.6 | 27.5 | 3.7 | 28.7 | 71.3 |
| | | | | C=C | C=O | O-C=O | | |
| EEG-N-S constant voltage (Sharif *et al.*, 2020) | 34.9 | 9.9 | 55.2 | 56.2 | 26.7 | 5.4 | - | - |
| EEG-N-P constant voltage (Sharif *et al.*, 2020) | 37.0 | 6.4 | 56.6 | 58 | 27.5 | 5.5 | | |

### *2.3.4 Transmission Electron Microscopy (TEM)*

TEM was used to obtain high-resolution images of graphene, as shown in Figure 2.7 and 2.8, sheets of graphene can be observed at different magnifications. Figure 2.7 (a) shows two overlapping graphene sheets, and the edges of the graphene are visibly folded. Figure 2.7 (d) shows a higher magnification image, the fringes at the edges of the graphene show that this sheet is not single-layer graphene; more than five fringes can be seen, indicating few layer graphene. The selected area electron diffraction (SAED) shows a hexagonal structure. From this diffraction pattern in figure 2.7 (e) the number of layers can be analyzed by nanoarea electron diffraction patterns, they are determined by shifting the incidence angle between the electron beam and the graphene sheet (Meyer *et al.*, 2007); the intensity profile difference indicates a single layer, double layer graphene or multilayer. In this case, the diffraction intensities indicate multilayer graphene; as they change depending on the selected angle. Bilayer graphene intensities vary greatly and some peaks are entirely suppressed at certain angles, on the contrary, monolayer graphene changes in profile intensity are relatively small (Meyer *et al.*, 2007). A study of graphene exfoliated using ammonium sulfate as electrolyte reported a diffuse diffraction ring pattern, indicating polycrystalline characteristics in an amorphous material, it was suggested that the amorphous nature was related to the surface functionalization of graphene (Y. Z.N. Htwe *et al.*, 2019).

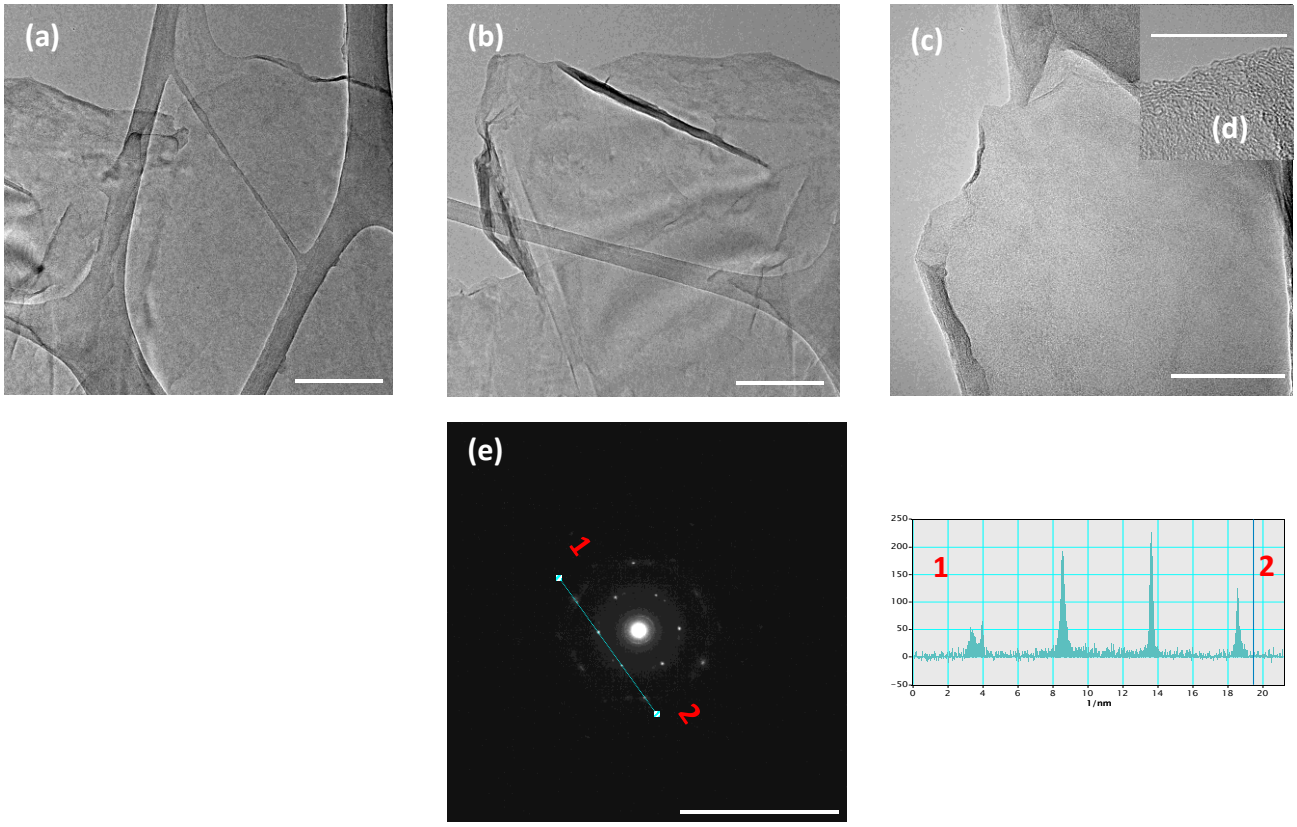


Figure 2.7: (a) to (d) TEM images of EEG-N-P, (e) diffraction patterns.

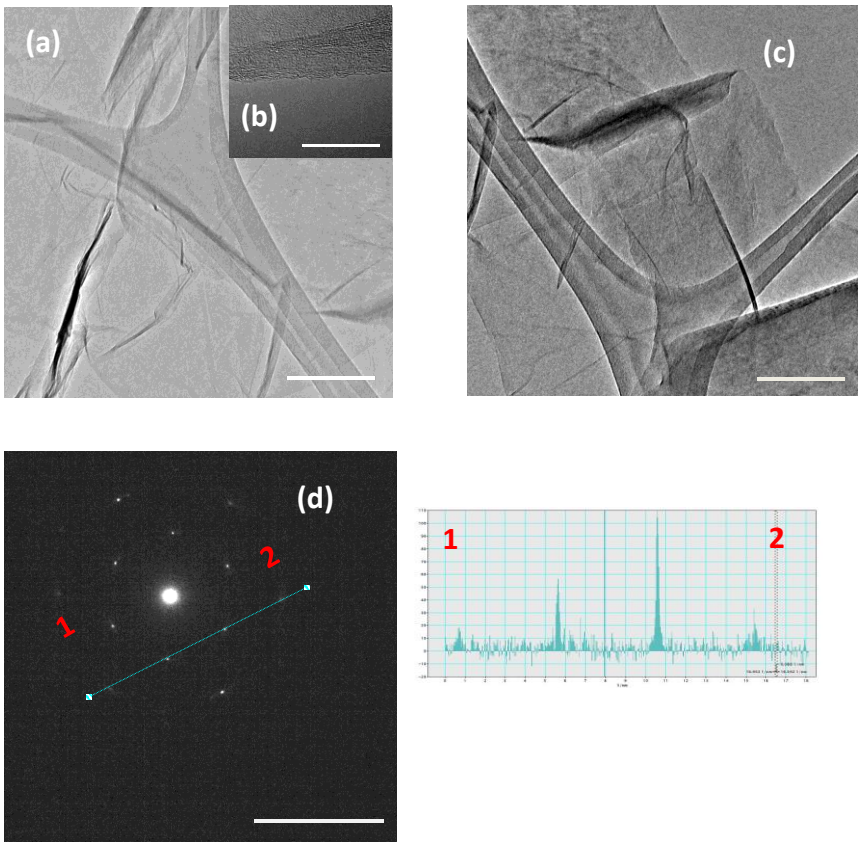


Figure 2.8: (a) to (c) TEM images of EEG-N-S, (d) diffraction patterns.

*2.3.5 Constant current vs. constant voltage at small and large scales.*

Anodic graphene exfoliation at constant voltage and constant current was carried out and the obtained material was characterized to analyze the possible differences between constant voltage and constant current.

Figure 2.9 shows the cell voltage- time and current-time plots obtained when constant voltage or constant current was used. It is evident that the average current and voltage was different for the EEG-N-S and EEG-N-P and this difference also impacts the exfoliation time, where exfoliation time is lower for the sample with the highest average cell voltage or average current.

At the beginning of the exfoliation the resistance is high as the graphene layers are just starting to expand; after few minutes the voltage decreases because the intercalation and exfoliation becomes easier. At the end of exfoliation, the resistance and voltage increase as a result of lower area in solution.

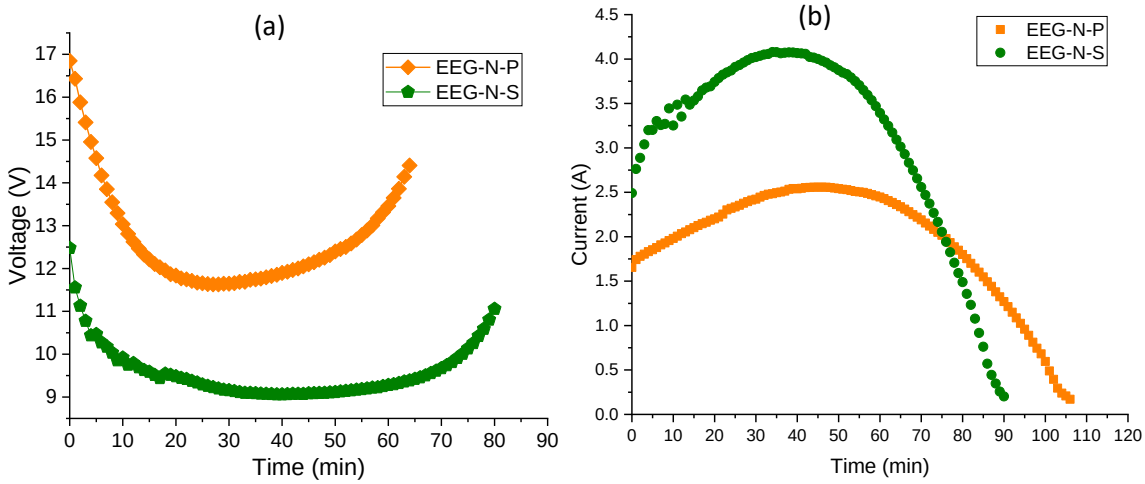


Figure 2.9: current and voltage behaviour vs. time during exfoliation of EEG-N-P and EEG-N-S when (a) constant current of 200 mA cm-2 is applied (b) constant voltage of 10 V is applied at 16 $cm^2$ scale.

In order to determine the thermal stability of the samples, TGA of graphene exfoliated at constant voltage was performed (figure 2.10). The sample exfoliated in $(NH_4)_2SO_4$ (EEG-N-S) retained 80% of its weight at a temperature of 195 ± 17 °C and 50% weight

at a temperature 480 ± 21°C. As expected, the samples exfoliated at constant voltage with $(NH_4)_2HPO_4$ (EEG-N-P) showed higher thermal stability, retaining 80% of its weight at 171 ± 6 °C and 50% at 712 ± 27 °C. Comparing these results with previous studies of graphene exfoliation using constant voltage (Sharif *et al.*, 2020), these samples showed a lower stability, losing 50% of their weight at temperatures around 160 to 200 °C lower than those observed by (Sharif *et al.*, 2020). The differences in exfoliation such as electrode area that was higher in this study, as well as the 0.5 cm lower spacing between electrodes may have influenced these results of lower thermal stability.

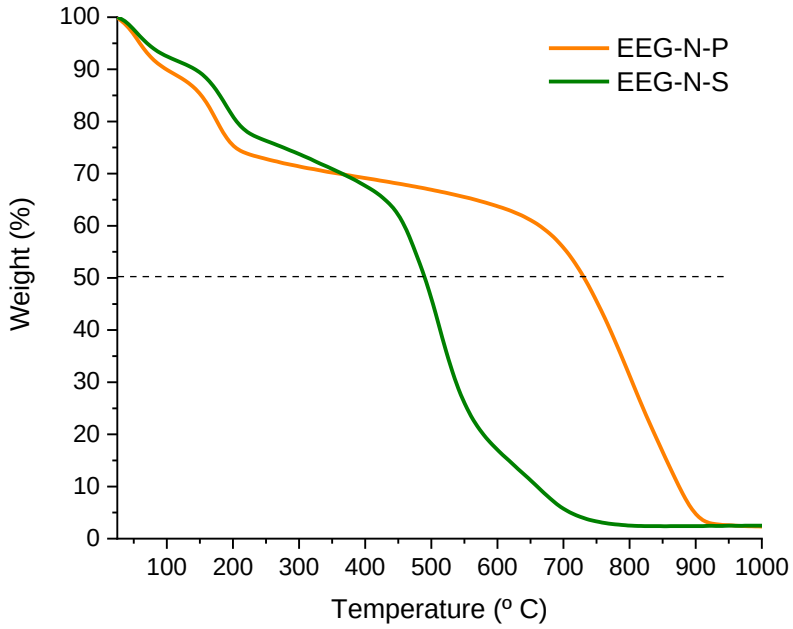


Figure 2.10: TGA plot of EEG-N-P and EEG-N-S obtained with constant voltage exfoliation.

Raman spectroscopy was also carried out, an $I_D/I_G$ ratio of 1.27 ± 0.08 was obtained for EEG-N-P exfoliated at constant voltage and a $I_D/I_G$ ratio of 1.61 ± 0.06 for graphene exfoliated at CV in $(NH_4)_2SO_4$, as shown in figure 2.11. The $I_D/I_G$ ratio of the samples of graphene synthesized under the same conditions were less than 0.5 (Sharif *et al.*, 2020), suggesting less defects compared to the graphene exfoliated in this study. This may explain the lower thermal stability obtained from the TGA experiments likely due to the difference of area, electrode spacing and higher doping of heteroatoms.

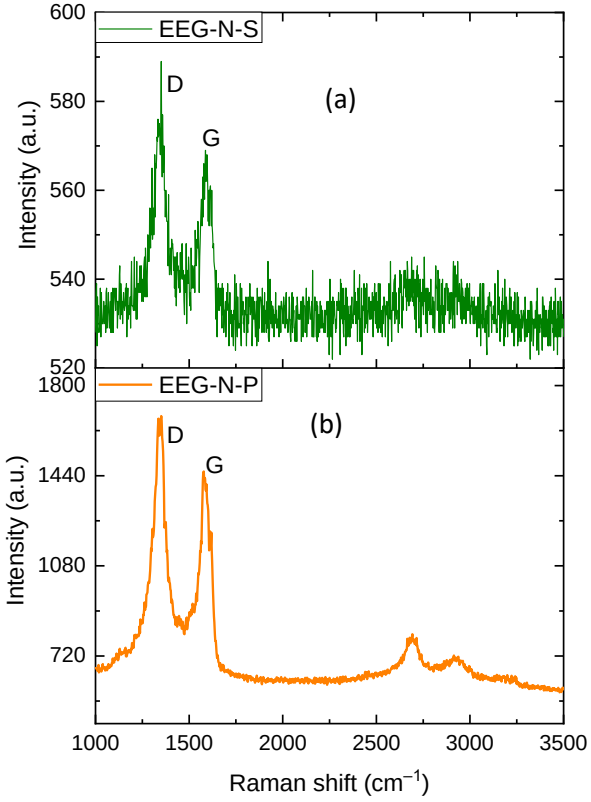


Figure 2.11: Raman spectra of (a) EEG-N-S and (b) EEG-N-P obtained using constant voltage.

### *2.3.6 Effect of electrolyte pH on yield and energy consumption*

The initial pH of the two electrolytes used for exfoliation was found to be significantly different; 0.1 M ammonium phosphate solution had a pH of 8.12, and 0.1 M ammonium sulfate had a pH of 5.45. The graphene yield from exfoliation of graphene in ammonium sulfate was found to depend on the pH (see Figure 2.12), with the highest yield obtained at the highest pH tested of 9.95 (yield 64 ± 6.8**%**). Exfoliation at a pH of 4.04 resulted in a yield of 53 ± 1.6% and the neutral pH of 7.03 had the lowest yield of 40 ± 15.5%.

This effect can be explained by the lower potential needed for oxygen evolution in alkaline media, facilitating the exfoliation. The differences in the mechanism of exfoliation between using acidic and alkaline electrolytes for exfoliation has been reported to be related to the size of the ions (Bakunin *et al.*, 2019). Sulfate ions have a size of 4.60 Å, while the interlayer spacing between graphite layers is approximately 3.35 Å, while, $OH^-$ ions have a size of around 2.50 Å (Bakunin *et al.*, 2019). This small

size compared to the interlayer space makes exfoliation simpler as the ions are able to intercalate easier.

The exfoliation of graphene in acidic media starts fast and the first exfoliated particles start to fall apart, mainly consisting of graphitic particles which have not been completely exfoliated. This has been discussed in a previous study (Abdelkader *et al.*, 2015) where the exfoliation in acidic electrolyte also showed more graphitic particles and lower yield, independent of the type of graphite anode used. (Abdelkader *et al.*, 2015)

A recent study of electrochemical exfoliation at different pH reported a higher expansion achieved but low exfoliation with a pH of 1.0, on the contrary, a lower expansion and higher exfoliation was found with a pH 10.0 solution (Tamgadge and Shukla, 2019). This suggests that electrolytes with different pH can be used for two-step electrochemical exfoliation where expansion and exfoliation occurs separately.

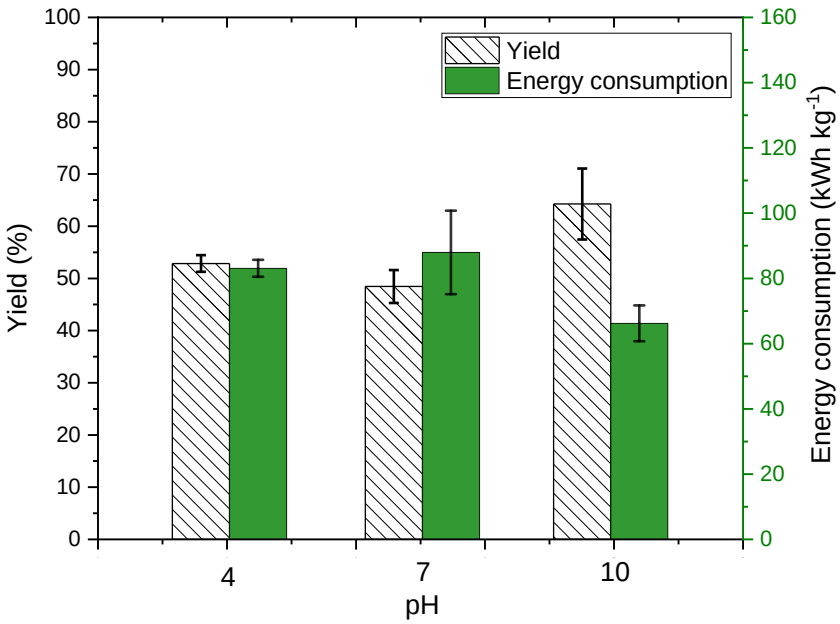


Figure 2.12 energy consumption and yield of EEG-N-S exfoliated at different pH in small scale of 4 $cm^2$.

*2.3.7 Yield and energy consumption at different electrodes areas*

The exfoliation of graphite in ammonium phosphate and ammonium sulfate required different amount time to be completed. As shown in figure 2.3, with ammonium phosphate as the electrolyte, the cell voltage was higher, and the exfoliation was completed after around 65 min. In an ammonium sulfate electrolyte the cell voltage was lower, and exfoliation took around 80 min.

The specific energy consumption can be calculated from the cell voltage, current, exfoliation time and amount of graphene obtained. This energy consumption per kg of graphene product was calculated (Appendix 1-4), and the lowest energy consumption was achieved with the use of an ammonium phosphate electrolyte, as shown in figure 2.13 and 2.14. The energy consumption reported in this study only includes the energy used for graphene exfoliation, and not the energy consumed in the post processing of graphene (sonication, centrifugation). The reason for the difference in energy consumption can be related to the yield of exfoliated material; with an ammonium phosphate electrolyte the graphene yield was higher than that obtained with ammonium sulfate. Previous studies have reported that the properties and yield of graphene obtained depend on the electrolyte composition (Y Z N Htwe *et al.*, 2019).

Electrochemical exfoliation of graphene foil studies in aqueous solutions of ammonium salts typically reported yields between 38 and 60% (Sharif *et al.*, 2020 ; Nagyte *et al.*, 2020 ; Achee *et al.*, 2018) which is consistent with the yield obtained in this study. A yield of 65% was achieved by using compressed graphite flakes and a redesigned electrochemical reactor (Achee *et al.*, 2018).

The yield of the 4 $cm^2$ electrodes area exfoliation was around 40 to 50% as shown in figure 2.13, whereas for the 16 $cm^2$ electrodes area exfoliation the yield was always higher than 55% (see figure 2.14). This increase in yield may be due to the incomplete exfoliation of graphite foil observed with the larger area exfoliation. Appendix 9 and 10 show the graphoil before and after anodic exfoliation at 4 $cm^2$ and 16 $cm^2$ electrode area. Exfoliation of the graphoil in contact with solution was not complete as the current dropped (in constant voltage exfoliation) even though a large electrode area was still in solution, this decrease in exfoliation and incomplete exfoliation was present

in both constant current and constant voltage for 16 $cm^2$ electrode area. This may explain why more of what was exfoliated was graphene-like material instead of graphite-like thicker flakes. During 4 $cm^2$ electrode area exfoliation all the graphite foil in contact with solution is exfoliated, but a higher percentage corresponds to graphite-like material, decreasing the graphene yield.

The specific energy for exfoliation of EEG-N-S was lower with the larger 16 $cm^2$ electrodes than with the 4 $cm^2$ graphite foil. For constant current exfoliation of EEG-N-S, the exfoliation time did not change significantly with the increased electrode area. With constant voltage exfoliation of EEG-N-S, the exfoliation time increased when the electrode area was increased, but with a smaller electrode the average current density was higher, resulting in higher energy consumption.

In most cases the yield and specific energy consumption obtained with larger 16 $cm^2$ electrodes was about the same with both constant current and constant voltage exfoliation. This was not the case for EEG-N-P energy consumption, which was lower at constant voltage exfoliation. By analyzing the average current (appendix 2) at constant voltage exfoliation it can be noticed that the current density is lower, this suggests that lower current density between 100 and 200 mA $cm^{-2}$ for EEG-N-P exfoliation may result in higher yield comparable to constant voltage. With smaller 4 $cm^2$ electrodes, the EEG-N-P exfoliation exhibited lower energy consumption mainly due to the lower exfoliation time required and greater amount of graphene obtained.

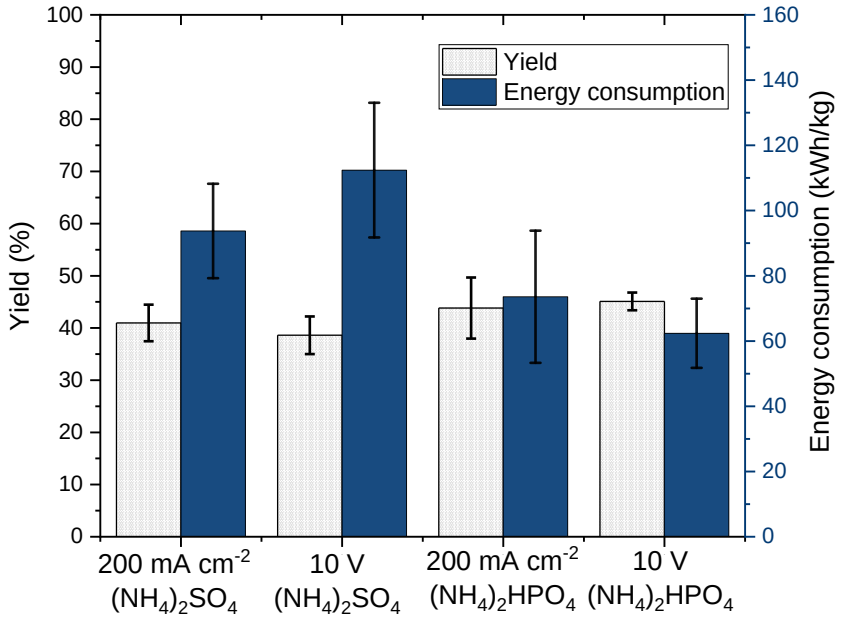


Figure 2.13: energy consumption and yield of graphene exfoliated with 0.1 M $(NH_4)_2SO_4$ and $(NH_4)_2HPO_4$ using constant current of 200 mA $cm^{-2}$ or constant voltage of 10 V, with an electrode area of 4 $cm^2$.

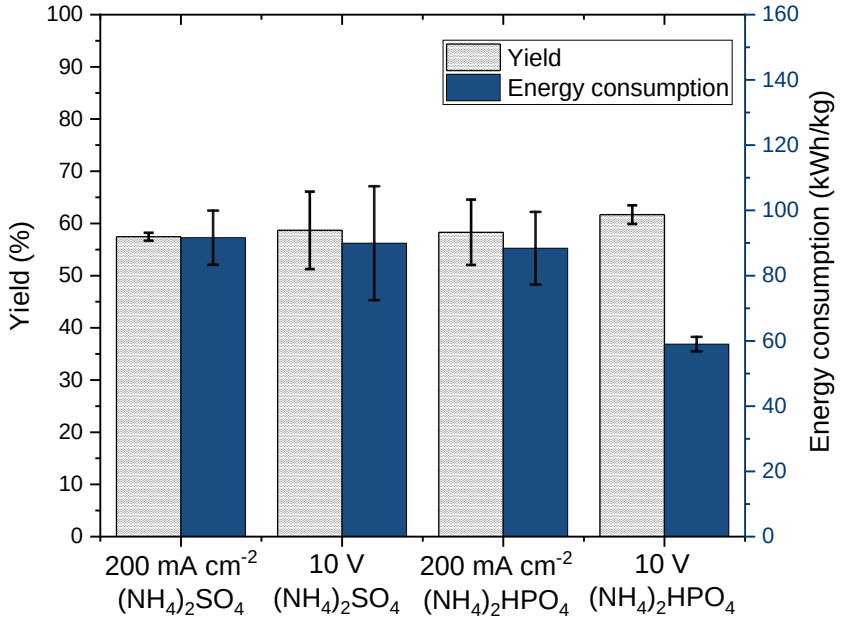


Figure 2.14: energy consumption and yield of graphene exfoliated with 0.1 M $(NH_4)_2SO_4$ and $(NH_4)_2HPO_4$ using constant current of 200 mA $cm^{-2}$ or constant voltage of 10 V, with an electrode area of 16 $cm^2$.

*2.3.8 Yield and energy consumption in exfoliation at different current densities*

Figure 2.15 shows the effect of current density on the specific energy consumption and graphene yield. As expected, the specific energy consumption increased with current density for both EEG-N-P and EEG-N-S graphene. The effect was more significant for EEG-N-P. The current density had only a small effect on yield, with slightly higher yield observed at low current densities for both EEG-N-S and EEG-N-P.

At a current density of 200 mA $cm^{-2}$ samples, the yield and specific energy consumption were about the same for EEG-N-S and EEG-N-P, as discussed above. At the highest current density of 300 mA $cm^{-2}$, the yield decreased and the energy consumption were highest. This may due to the faster exfoliation of graphene, where less time may be available for intercalation, leading to more multilayered graphene and graphite particles. In this case, at high current density, the increased energy consumption is likely due to a combination of higher ohmic losses and lower yield of graphene.

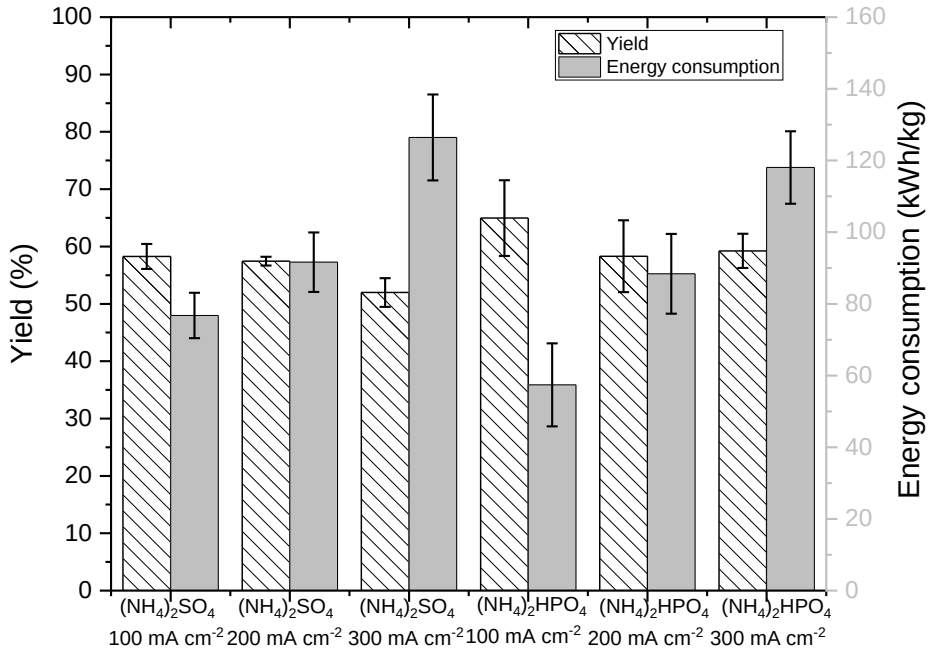


Figure 2.15: energy consumption and yield of graphene exfoliated with 0.1 M $(NH_4)_2SO_4$ and $(NH_4)_2HPO_4$ using different constant currents of 100, 200 and 300 mA $cm^{-2}$ at of 16 $cm^2$ electrodes area.

The incomplete exfoliation of the graphite foil when a larger electrode area was used can be a reason of the higher yield obtained, the non-uniform current density more significant in smaller electrodes could have played a role in the higher yield. The exfoliation was stopped when the potential started to increase rapidly, to avoid further exfoliation of low quality graphene and graphite particles at both scales. This process results in incomplete exfoliation, but a higher percentage of the exfoliated material is obtained as graphene.

Temperature changes were recorded during exfoliation. It was found that when using larger electrodes, the temperature increased during exfoliation due to higher currents or cell potentials. With a smaller, 4 $cm^2$ graphite foil anode, the temperature was 36 ± 2 °C, while with the larger 16 $cm^2$ electrodes the temperature reached 68 ± 1.5 °C, for the same current density of 200 mA $cm^{-2}$.

As expected, the increase in temperature observed also increased with current density. At 300 mA $cm^{-2}$, the temperature reached 84 ±2 °C for exfoliation in $(NH_4)_2HPO_4$ solution, and 73 ± 0.5 °C in $(NH_4)_2SO_4$ electrolyte; while at low current density of 100 mA $cm^{-2}$, the temperature was 37 ± 5 °C for exfoliation in $(NH_4)_2HPO_4$ and 35 ± 4 °C in $(NH_4)_2SO_4$. The higher temperatures observed for exfoliation of EEG-N-P are presumably due to the lower conductivity of the solution (being 13.7 mS for $(NH_4)_2HPO_4$ and 17.3 mS for $(NH_4)_2SO_4$), and hence higher cell voltage and ohmic heating, compared to the EEG-N-S exfoliation.

The conductivity of exfoliated graphene films were obtained using a four point probe, as described in Section 2.2, and the results obtained are shown in table 2.4. EEG-N-S showed higher conductivity than EEG-N-P for constant current exfoliation.

Table2.4: conductivity of EEG films, exfoliated with constant current (200 mA $cm^{-2}$) in both ammonium sulfate and ammonium phosphate solutions.

| **EEG** | **Conductivity (S $cm^{-1}$)** |
|---|---|
| EEG-N-S Constant current | 302.12 ± 107 |
| EEG-N-P Constant current | 200.6 ± 85 |

## 2.4 Conclusions

Electrochemical exfoliation of graphene using larger electrode area of 16 $cm^2$ was achieved; a greater amount of graphene of approximately 4 to 5 times higher was obtained compared to the smaller 4 $cm^2$ electrodes typically used.

The yield increased in all the cases for the larger electrode area, and was around 55-65% compared to 40-50% with smaller electrodes. Further work is needed to determine the factors influencing the yield and study the incomplete exfoliation of graphene at 16 $cm^2$.

The specific energy consumption was lower with larger electrodes, except for exfoliation in $(NH_4)_2HPO_4$ at constant current. The data suggests that a lower current density between 100 and 200 mA $cm^{-2}$ should be investigated to determine if there can be an increase in the yield of EEG-N-P at constant current and decrease in the specific energy consumption for both smaller and larger electrode area.

Constant voltage vs. constant current exfoliation was investigated; yield and energy consumption did not present significant variations. However, higher thermal stability was achieved with EEG exfoliated at constant current. This is important as it suggests that constant current may be a better option for electrochemical exfoliation as it presents advantages and simplifications to scale-up and also provides doped EEG with higher thermal resistance.

The study of exfoliations at different current densities showed interesting results, the EEG-N-S showed variations on weight loss at different temperatures ranges during TGA analysis. This suggests that different functional groups were present in the samples depending on the current density used. Further sample characterizations, such as XPS are needed to identify additional differences in sample composition.

It was found that pH had an effect on the electrochemical exfoliation of graphene. The pH likely affects the properties of the graphene, and could be used to adjust the desired properties, improve the yield or reduce the specific energy consumption. Characterization of EEG at different pH was not carried out in this study; further work

is needed to determine the differences in EEG exfoliated at different initial pH, such as flake size and elemental composition.

Graphite foil was used as the anode for this work; however, different graphite electrodes can be studied to determine the yield and energy consumption and compare with the results obtained in this study. It would be interesting to see if all the graphite electrodes such as graphite flake and graphite present incomplete exfoliation at larger areas.

Future work should also focus on the different electrode arrangements or multiple electrode exfoliations. Electrochemical exfoliation with larger electrodes areas need to be explored to study incomplete graphene exfoliation, yield and energy consumption.

The scale-up of graphene production needs further development to be able to reach mass production. This study provides some insights of main parameters that need to be controlled during anodic exfoliation and some challenges that require future studies such as temperature control and incomplete exfoliation. This incomplete exfoliation may not be a waste as it can be reused in a new exfoliation with a fresh electrolyte by adjusting the dimensions and start a new exfoliation. Temperature could be controlled with an ice bath or by using continuous process where fresh electrolyte is used along the exfoliation process.

## Chapter 3. Graphene adsorption and regeneration

### 3.1 Introduction

Water is a resource of great importance, it has been recognized as a right to every human being by the United Nations General Assembly in July 2010, and it needs to be safe, adequate, and affordable (United Nations, 2020). Fresh water can contain pollutants from natural sources and also from industrial wastewater such as mining industries (Velizarov, 2005). The application of suitable techniques for the treatment of industrial wastewater and drinking water is essential.

Industries such as metal plating facilities, mining and fertilizers are sources of wastewater and pollution (Fu and Wang, 2011; Jagtap *et al.*, 2012). The textile finishing and dye industries are water consumers, and present a source of water pollution from dyes that are a challenge to remove (Kyzas *et al.*, 2017).

Some techniques commonly used for water treatment are chlorination (Shen *et al.*, 2011), ozonation (Robinson *et al.*, 2001), coagulation-flocculation, biodegradation, membrane separation, advanced oxidation and ion exchange (Crini, 2006), among others. However, these methods have some drawbacks; the performance of biological treatment can be affected by contaminants that are resistant to biological degradations, some toxic contaminants can also interfere with biological treatment processes. In addition, techniques such as ozonation, coagulation-flocculation, reverse osmosis, chlorination, and ultrafiltration can produce hazardous by-products with mutagenic, carcinogenic, and genotoxic nature (Tijani *et al.*, 2014). Most physicochemical and biological treatments are unsuitable for the removal of dyes from water, as the majority of dyes present stability to oxidizing agents, photodegradation, and biodegradation. Adsorption is one of the most effective methods for the removal of organic dyes (C. Wang *et al.*, 2011).

Among the methods mentioned above, adsorption is well suited for removal of low concentrations of toxic or recalcitrant organic contaminants and is adaptable, cost-effective, rapid, and provides easy separation for these applications (Kim *et al.*, 2018) (Chowdhury and Balasubramanian, 2014) (Kyzas *et al.*, 2017). Adsorption is useful for

the removal of insoluble organic pollutants, adsorbents were reported to remove diverse organic pollutants with a removal capacity of 80 to 99.9%; for this reason, adsorption has been widely used to remove different types of organic pollutants from diverse polluted water sources (Ali *et al.*, 2012).

The main disadvantages of adsorption as water treatment technique are the elimination of the material where regeneration of the material incineration or replacement is required. In the case of commercial activated carbons, the performance will be dependent on the type of material used and the regeneration is expensive and results in material loss (Crini and Lichtfouse, 2020). The adsorption process for drinking water treatment has the disadvantage that spent adsorbent media must be disposed or regenerated. Regeneration can be expensive and lead to further environmental impacts.

Adsorption can be described as the accumulation of a substance on a surface. For water treatment, it is the process whereby a solid adsorbent removes contaminants from polluted water: the pollutant that is adsorbed on the solid is defined as the adsorbate (Ali *et al.*, 2012).

*3.1.2 Adsorption with graphene*

The properties of graphene make it a good candidate to be used as an adsorbent; it presents a theoretical specific surface area of 2630 $m^2 g^{-1}$ (Zhu *et al.*, 2010), it is highly efficient in the control of diverse contaminants mainly due to the large surface area and fast electron transfer (Shen *et al.*, 2015). In addition, the graphene composites such as graphene oxide can be used as adsorbents as well with different characteristics such as lower surface hydrophobicity and differences in adsorption mechanisms (Ersan *et al.*, 2015).

Graphene nanosheets can be compared with other types of carbon-based adsorbents such as activated carbon (AC) and Carbon Nanotubes (CNT). Differences in the structure and chemistry of these adsorbents can lead to different interactions between adsorbent and organic contaminants (Ersan *et al.*, 2017). It has been found that the adsorption capacity of MB on activated carbon was higher than that for GO most

probably as a result of its higher surface area (Li *et al.*, 2013); but once adsorption was normalized with the BET surface area of the adsorbent, graphene oxide showed a better adsorption capacity (Yang *et al.*, 2011).

One advantage of using graphene as adsorbent is the possibility of regeneration. Graphene oxide/magnetite and graphene/titanium dioxide nanocomposites have been used as adsorbents in previous studies, and the regeneration has been studied (Sharif *et al.*, 2017; Sharif and Roberts, 2020). One of the studies used graphene oxide synthesized using Hummers' method and reduced to create graphene-iron oxide nanocomposites with different iron oxide weight percentages. A recovery of graphene after regeneration higher than 96% was obtained when anodic regeneration was used with a current density of 10 mA $cm^{-2}$ (Sharif *et al.*, 2017). The adsorption capacity increased to 200% of its initial value after regeneration, suggesting that more adsorption sites were available for methylene blue, possibly due to corrosion of the material (Sharif *et al.*, 2017).

In this work, the adsorption of EEG was evaluated with two different dyes, methylene blue (MB), a cationic dye, and methyl orange (MO), an anionic dye. The adsorption capacity and electrochemical regeneration of electrochemically exfoliated graphene prepared under a range of conditions has been evaluated compared to previous studies.

## 3.2 Experimental methods

### *3.2.1 Adsorption*

Dyes were used as a model pollutant for adsorption tests. There is a need to remove such dyes from waste water as they are considered a pollutant and removal is required before discharge (Kyzas *et al*., 2017). In this study, two different dyes (anionic and cationic) were chosen as organic contaminants in order to investigate the adsorption capacity of the EEG: methylene blue and methyl orange. The pH of all the adsorption test solutions was kept neutral at pH 7.

In order to determine the time necessary to reach equilibrium, batch adsorption tests were performed. A known amount of EEG was dispersed in 300 ml of an aqueous

solution of MB and/or MO solution at 25 ppm concentration. Thereafter, the solution was sonicated with a bath sonicator for 5 min and placed in a Fisherbrand™ Multi-Platform shaker at 200 rpm. Samples were taken at different times and analyzed with a UV-Vis spectrometer until equilibrium was achieved.

Batch adsorption test were performed in order to determine the adsorption capacity of the different EEGs. A known amount of EEG was dispersed in 200 ml of an aqueous solution of MB and/or MO solution at different initial concentrations. Thereafter, the solution was sonicated with a bath sonicator for 5 min and placed in a Fisherbrand™ Multi-Platform shaker at 200 rpm for the time needed. All adsorption tests were performed at least three times.

3.2.2 *Dye concentration analysis*

Ultraviolet-visible spectroscopy (UV–Vis) analysis was carried out to determine the concentration of each dye in solution before and after adsorption, using a UV-Vis Spectrophotometer (Shimadzu UV-2600i) at a wavelength of 464 nm for the MO and 664 nm for MB. These wavelengths were used as they showed the higher adsorption according to the spectrums (Appendix 11 (a) and 12 (a)). A calibration curve was created for both dyes (Appendix 11 (b) and 12 (b)) and with a $R^2$ of 0.999 % in both cases. According to the calibration of methylene blue and methyl orange, the detection limit was around 0.01 ppm for methylene blue and 0.18 ppm for methyl orange.

*3.2.3 Adsorption capacity*

The adsorption capacity can be calculated from the dye concentrations obtained in batch adsorption experiments, based upon a mass balance for the dye, as follows: (Tien, 1994):

$$q_e = \frac{(C_0 - C_e)V}{m} \qquad (3.1)$$

Where:

$q_e$ = equilibrium adsorption capacity (mg $g^{-1}$)

$C_0$ = initial dye concentration (mg $L^{-1}$)

$C_e$ =equilibrium concentration (mg $L^{-1}$)

$m$ = mass of adsorbent, EEG (g)

*3.2.4 Adsorption isotherms*

In order to obtain the adsorption isotherms, a fixed amount of EEG was added to solutions at different initial concentrations of adsorbate, in this case the two dyes methylene blue and methyl orange. The initial concentrations started from 4 ppm to 10 ppm in a 300 ml volume.

Adsorption isotherms are used to describe the equilibrium relationship between the adsorbent and adsorbate. Commonly the relationship between the quantity adsorbed and the quantity remaining in solution at an established temperature (El-Khaiary, 2008).

The equilibrium adsorption isotherms are used to design adsorption systems and the constants of the isotherms express the adsorbents capacity and surface properties. In addition, the shape of the isotherm provides information to determine the adsorption mechanism (El-Khaiary, 2008).

The most common adsorption isotherm equations are the Langmuir and Freundlich isotherms (Kyzas *et al.*, 2017), as shown in equations 3.1 and 3.2 respectively. These two isotherms will be used in this work to study the adsorption capacity ($Q_e$) of the adsorbent.

Langmuir

$$Q_e = \frac{Q_m K_L C_e}{1 + K_L C_e} \qquad (3.2)$$

Freundlich

$$Q_e = K_F (C_e)^{1/n_f} \qquad (3.3)$$

where: $Q_m$ (mg/g) is the maximum loading of adsorbate on the adsorbent; $K_L$ (L $mg^{-1}$) is the Langmuir adsorption equilibrium constant; $K_F$ ($mg^{1-1/n}$ $L^{1/n}$ $g^{-1}$) is the Freundlich constant describing the adsorption capacity; and $n_f$ is dimensionless and is the Freundlich constant that represents the adsorption intensity (Kyzas *et al.*, 2017).

The Langmuir isotherm is based on monolayer adsorption of adsorbate on the adsorbent and represents chemisorption on a limited number of adsorption sites, where the adsorption energies are the same and do not depend of surface coverage, and no interaction between the adsorbate molecules. In contrast, the Freundlich isotherm is used for heterogeneous surfaces with an exponential distribution of energies and active sites (Kyzas *et al.*, 2017). Freundlich isotherm does not predict a maximum loading of adsorbate on the surface of the adsorbent; therefore multilayer adsorption is implied, associated with physisorption (Kyzas *et al.*, 2017).

It is known that morphological characteristics and chemical properties of the graphene need to be considered in order to associate the physicochemical properties of graphene nanosheets and the adsorbate molecules, including the number or layers, wrinkles, polarity, and surface chemistry, among others (Ersan *et al.*, 2017). Raman, TEM and other characterization data (see section 2.2.5) was used to describe the EEG used in this study, including the surface charge and chemistry, surface area and pore size distribution, to provide a better understanding of the adsorption of the organic dyes on the EEG.

*3.2.5 Adsorption-Regeneration*

The adsorption and regeneration study was carried out studying the adsorption of methylene blue only. 20 mg of EEG was dispersed in 200 ml of a 25 ppm MB solution, the final concentration of methylene blue in solution after adsorption was around 3 ppm when using EEG-N-P as the adsorbent and around 13 ppm when using EEG-N-S. The concentration of MB used was chosen in order to compare with other studies and the adsorbate dose was chose by the adsorption capacity of EEG.

After adding the EEG adsorbent, the solution was sonicated for 5 minutes to disperse the EEG and stirred for 30-40 minutes at 200 rpm to achieve equilibrium. The solution was filtered using a vacuum filter and 0.1 μm membrane filter paper to recover the spent adsorbent. Electrochemical regeneration was performed with a two-electrode cell using a graphite plate as the anode, stainless steel cathode, and the filter paper with the EEG cake between the two electrodes, with the EEG cake in contact with the anode. The EEG cake was saturated with few drops of a 2 wt % NaCl solution in order

to increase the conductivity. The regeneration cell area was 8.04 $cm^2$. Figure 3.1 shows a schematic representation of the adsorption and regeneration process. A current density of 10 mA $cm^{-2}$ was used to regenerate the graphene (Sharif *et al.*, 2017; Sharif, 2017).

In order to obtain the regeneration time, initial adsorption test was carried out with fresh EEG, the spent EEG of each of the adsorption tests was recovered and a certain amount of time was selected for regeneration of the different batches. A second adsorption test was carried out by all of them to measure the adsorption capacity compared to the initial capacity of fresh EEG. The regeneration time was selected as the time when the adsorbent recovered the initial adsorption capacity after regeneration considering that full mineralization of the dye was achieved. Variation of EEG regeneration time might present changes from batch to batch due to resistance in the electrochemical cell and possible changes in the adsorbent mass.

After regeneration, the graphene was used for another cycle of batch adsorption under the same conditions of the initial adsorption. After the adsorption tests, EEG was recovered and the concentration of the dye solution was measured by using UV-Vis in order to determine the regeneration efficiency. Adsorption tests were carried out again with the regenerated EEG for three complete cycles. Each cycle consisted on adsorption and electrochemical regeneration as shown in figure 3.1.

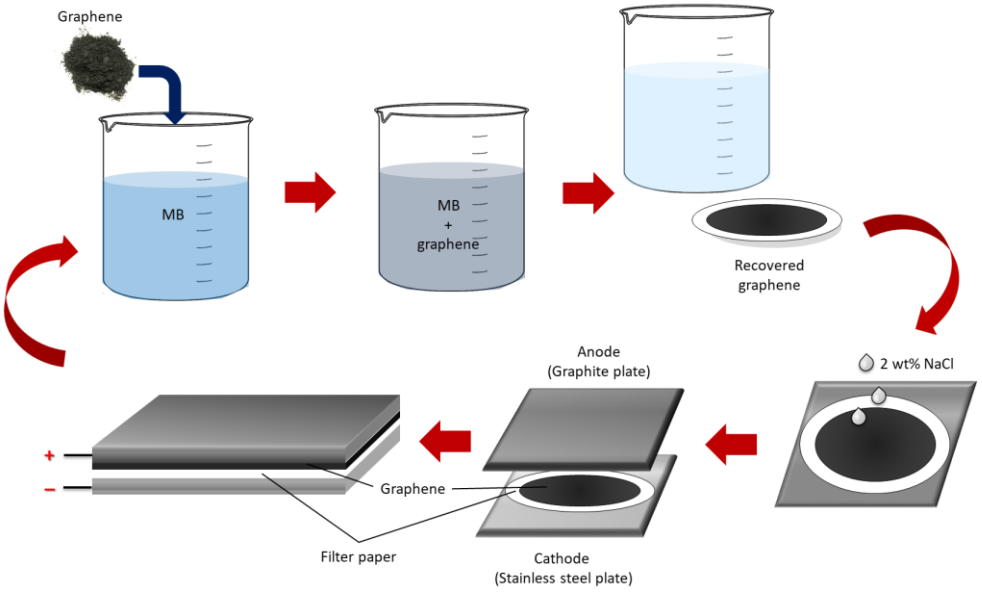


Figure 3.1: schematic representation of adsorption-regeneration process or graphene.

The regeneration efficiency was determined by comparing the adsorption capacity of the regenerated adsorbent with the initial adsorption capacity, measured under the same adsorption conditions (Brown *et al.*, 2002):

$$\phi = (q_r/q_i) \times 100 \qquad (3.4)$$

Where:

$\phi$ = regeneration efficiency (%)
$q_r$= adsorption capacity of the regenerated adsorbent (mg $g^{-1}$)
$q_i$= initial adsorption capacity (mg $g^{-1}$)

Conditions for adsorption were identical for initial and final adsorption tests, and both EEG-N-P and EEG-N-S were exposed to adsorption and regeneration tests.

X-ray diffraction analysis (XRD) was carried out in order to determine changes in crystalline structure of the EEG samples. A Powder x-ray diffraction (PXRD) patterns were collected using a Bruker D8 Advance ECO instrument equipped with Cu Kα source (λ = 1.54178 Å, kV = 40, mA = 25) and a LYNXEYE XE detector. Scans were collected from 5-60° 2θ at a scan speed of 2.0s/0.04° step.

## 3.3 Results and discussion

### *3.3.1 Adsorption mechanism*

The two types of graphene showed a higher adsorption capacity for MB compared to MO, EEG-N-P showed a maximum adsorption capacity of 391 mg $g^{-1}$ for MB and 34 mg $g^{-1}$ for MO, while EEG-N-S achieved a maximum adsorption capacity of 166 mg $g^{-1}$ for MB and 21 mg $g^{-1}$ for MO according to the adsorption tests performed.

The Langmuir and Freundlich models were fitted to the experimental adsorption isotherm data obtained with EEG-N-P and EEG-N-S for MB and MO adsorbates. In all cases, the Langmuir model provided a better fit compared to Freundlich, therefore the results obtained by using this model are presented in this study. Figure 3.1 and 3.2 show the adsorption isotherm and table 3.1 and 3.2 show the fitting parameters of Langmuir and Freundlich model, for EEG-N-S there is no difference on the fitting of

both isotherms, showing the same $R^2$ values, in the case of EEG-N-P, the best fit was found in Langmuir model for both methylene blue and methyl orange adsorption.

These results suggest that the adsorption follows the Langmuir model for EEG-N-P, meaning monolayer adsorption and the adsorption using EEG-N-S could be explained by both Langmuir and Freundlich model.

The Langmuir isotherm is based on monolayer adsorption of adsorbate on the adsorbent and represents chemisorption on a limited number of adsorption sites, where the adsorption energies are the same and do not depend of surface coverage, and no interaction between the adsorbate molecules. In contrast, the Freundlich isotherm is used for heterogeneous surfaces with an exponential distribution of energies and active sites (Kyzas *et al.*, 2017). Freundlich isotherm does not predict a maximum loading of adsorbate on the surface of the adsorbent; therefore multilayer adsorption is implied, associated with physisorption (Kyzas *et al.*, 2017).

As expected, both EEG materials showed a higher adsorption capacity of MB compared to MO, higher values of adsorption for the cationic dye MB can be explained by the electrostatic interaction between the negatively charged EEG surface and the adsorbate. It has been found that GO is negatively charged due to the oxygen-contain groups; therefore, graphene presents a preference for positively charged pollutants such as cationic dyes and heavy metal ions (Kyzas *et al.*, 2017). As a result, higher removal efficiency is obtained with cationic dyes, some studies had shown removal as high as 95%, while removal efficiency was considerably lower when anionic dyes were used (Ramesha *et al.*, 2011). Pi-pi interactions are also possible for adsorption of methylene blue, but they are considered to be significantly weaker than electrostatic interactions; (Kyzas *et al.*, 2017; Amft *et al.*, 2011).

A higher adsorption capacity was achieved with EEG-N-P than EEG-N-S adsorbent, for both cationic and anionic dyes. The BET Surface area was found to be 10.4 $m^2\ g^{-1}$ for EEG-N-P and 17.9 $m^2\ g^{-1}$ for EEG-N-S. Higher adsorption capacity was expected for EEG-N-S due to its higher surface area; however it presented lower adsorption capacity. Differences in average pore diameter and micropore volume of the two EEG were found. EEG-N-S has an average pore diameter of 160 Å, while EEG-N-P has an

average pore diameter of 558 Å. In addition, EEG-N-S showed a micropore volume of 0.001678 $cm^3\ g^{-1}$ while EEG-N-P micropore volume was 0.000355 $cm^3\ g^{-1}$. Thus the higher EEG-N-S surface area may be due to the increased micropore volume compared to EEG-N-P that may be too small to adsorb dyes. By calculating the porosity from the pore volume and graphite density, EEG-N-S results in a porosity of 0.38% while it is just 0.08% for EEG-N-P.

BET surface area was lower for EEG-N-P, this suggests that this EEG was more prone to restacking than EEG-N-S and that BET data does not give the real volume of surface area due to the restacking of EEG and it does not reflect the adsorption behavior. Therefore, this area is lower than the area available for adsorption.

This restacking of graphene is a result of van der Waals forces (Ersan *et al.*, 2017), therefore obstruction of adsorption sites can be caused (Yang *et al.*, 2011). Different amounts of restacking might be expected for the two different EEG; in addition, restacking is likely less severe during adsorption tests where EEG is dispersed in water than in dry BET tests.

The two different EEG materials were doped with different heteroatoms. It is known that graphene adsorption capacity of contaminants removal in water depends on adsorbent properties, such as functional groups, surface charge, and shape (Kim *et al.*, 2018). These changes in properties coming from the different element, and doping may explain the difference in adsorption capacity.

The percentage of oxygen present in the EEGs used in this study is shown in table 2.2. The presence of oxygen functional groups is the most common type of graphene functionalization, these groups makes the surface more hydrophilic and thus more easily dispersed in water (Ersan *et al.*, 2017). Studies have shown that oxygen functional groups can contribute to adsorption of organic contaminants, however at the same time, some water clusters will be created on the graphene oxide sheets decreasing the amount of available adsorption sites (Apul *et al.*, 2013; Beless *et al*., 2014; Ersan *et al.*, 2015).

The isotherms in this study give the maximum adsorption capacity, but further tests at lower concentration might be needed in order to have more data points and accurately fit the parameters ($K_L$/ $K_F$), as seen in the table 3.2 and 3.3 , both Freundlich and Langmuir models fitted the data equally well.

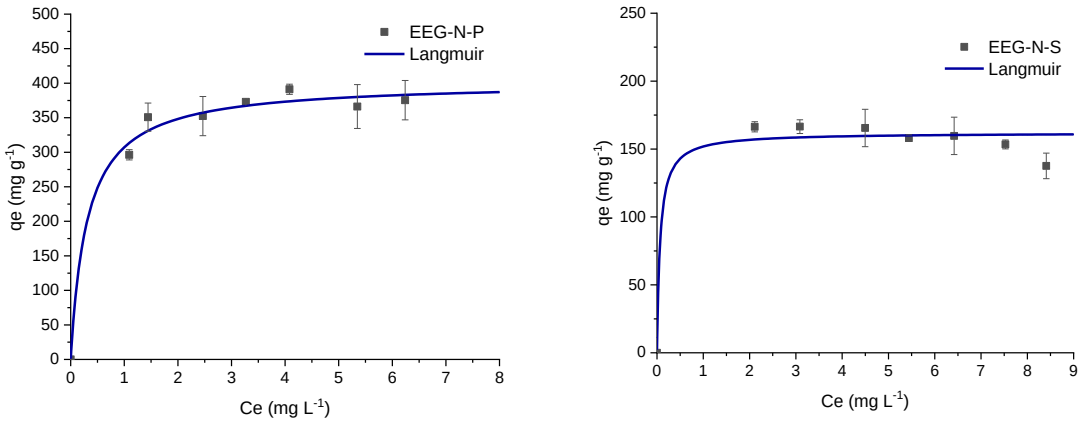


Figure 3.2: Adsorption isotherms of Methylene blue on (a) EEG-N-P and (b) EEG-N-S. Langmuir model was fitted to the data by non-linear regression.

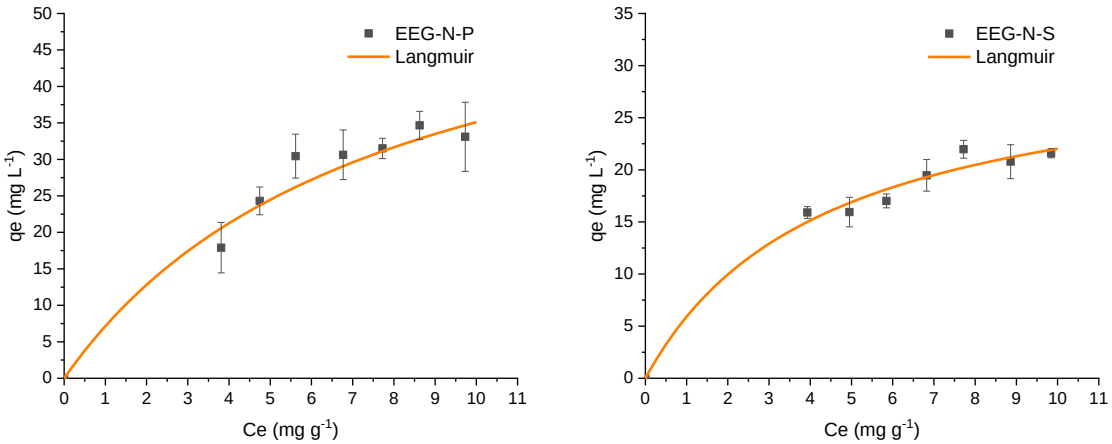


Figure 3.3: Adsorption isotherms of Methyl Orange on (a) EEG-N-P and (b) EEG-N-S. Langmuir model was fitted to the data by non-linear regression.

Table 3.1: Adsorption isotherm parameters based on the Langmuir and Freundlich equation for EEG-N-P and EEG-N-S using Methylene blue as contaminant.

| | Langmuir | | | Freundlich | | |
|---|---|---|---|---|---|---|
| **EEG** | $Q_m$ (mg $g^{-1}$) | $K_L$ (L $mg^{-1}$) | $R^2$ | $K_F$ ($mg^{1-1/n}$ $L^{1/n}$ $g^{-1}$) | $n_f$ | $R^2$ |
| EEG-N-P | 402 | 3.24 | 0.989 | 319 | 9.51 | 0.983 |
| EEG-N-S | 162 | 15 | 0.966 | 158 | 70 | 0.966 |

Table 3.2: Adsorption isotherm parameters based on the Langmuir and Freundlich equation for EEG-N-P and EEG-N-S using Methyl orange as contaminant.

| | Langmuir | | | Freundlich | | |
|---|---|---|---|---|---|---|
| **EEG** | $Q_m$ (mg $g^{-1}$) | $K_L$ (L $mg^{-1}$) | $R^2$ | $K_F$ ($mg^{1-1/n}$ $L^{1/n}$ $g^{-1}$) | $n_f$ | $R^2$ |
| EEG-N-P | 62.1 | 0.13 | 0.967 | 10.4 | 1.85 | 0.959 |
| EEG-N-S | 31.6 | 0.23 | 0.982 | 8.8 | 2.49 | 0.982 |

The adsorption capacity obtained with the EEGs used in this study is comparable with other studies. Adsorption of MB on graphenes with initial contaminant concentration of 60-100 ppm, pH 3 to 10 and temperatures from 293 to 333K have shown an adsorption capacity of 154 to 204 mg $g^{-1}$ (Liu *et al.*, 2012), while MB adsorption on GO at 600 ppm MB concentration, pH 2-9 and 295 K showed an adsorption capacity of 48.7 to 598 mg $g^{-1}$ (Yan *et al.*, 2014). Both EEG were between this ranges, this suggests that the graphene at this study is a good adsorbent at low concentrations and EEG-N-P showed a higher adsorption capacity compared to EEG-N-S.

The adsorption capacity of EEG-N-P in the adsorption of methylene blue was higher than compared to graphene (Liu *et al.*, 2012), and in the middle compared to GO at higher concentrations (Yan *et al.*, 2014). In addition, the adsorption capacity of methylene blue of both EEG-N-S and EEG-N-P compared to graphene nanocomposites such as Graphene-$Fe_3O_4$ and Graphene - carbon nanotubes is higher at similar initial dye concentrations (10-30 ppm)(Kim *et al.*, 2018). The present study focused on the

adsorption at low dye concentrations, further work is needed to determine the adsorption capacity of these materials at high dye concentrations.

Adsorption of dyes including MB on EEG has been studied previously, and it has been shown that it is possible to obtain an adsorption capacity around 511 mg $g^{-1}$ at concentrations of MB of 500 mg $L^{-1}$ (Xue *et al.*, 2016), however there have been few studies focused on lower concentrations of contaminants, (~ 10-25 ppm) and neutral pH values. This EEG can be used for the treatment of water with low concentrations of dyes, with a better performance on the adsorption of cationic dyes.

*3.3.2 Regeneration mechanism*

Anodic regeneration of EEG was carried out with the purpose of achieving mineralization of the methylene blue and reusing the EEG adsorbent. In this study, the by-products were not characterized. However, the mechanism of methylene blue electrochemical oxidation has been studied previously.

Mineralisation of methylene blue by electrogenerated $OH^{\bullet}$ radicals has been explained as follows (Panizza *et al.*, 2007):

$$C_{16}H_{18}ClN_3S \xrightarrow{51OH^{\bullet}} 16CO_2 + 6H_2O + H_2SO_4 + 3HNO_3 + HCl \qquad (3.5)$$

During electrochemical regeneration, two types of oxidation can happen: direct and indirect oxidation. Direct oxidation occurs due to electron transfer between organic matter and the surface of the anode. Indirect oxidation can also occur due to oxidizing agents such as hydroxyl radicals produced in the electrolytic decomposition of water (equation 3.6) as intermediate of oxygen evolution (equation 3.8) (Acuña-bedoya *et al.*, 2020). Radicals can oxidize organic matter and mineralize it (equation 3.7, where M represents the electrode or active site (De Moura *et al.*, 2016)

$$M + H_2O \rightarrow M\,(^{\bullet}OH) + H^+ + e^- \qquad (3.6)$$

$$R + M\,(^{\bullet}OH) \rightarrow M + CO_2 + H_2O \qquad (3.7)$$

$$M\,(^{\bullet}OH) \rightarrow M + \frac{1}{2}O_2 + H^+ + e^- \qquad (3.8)$$

Indirect oxidation happens as a result of oxidants electro generation at the surface of the electrode (Acuña-bedoya *et al.*, 2020). When NaCl is used as the electrolyte, as in

this study, strong oxidants can be produced (Najafpoor *et al*., 2017). Hypochlorous acid is produced in acidic in neutral media, chlorine gas in acidic media and hypochlorite ions in basic media (Equations 3.9-312), and these active chlorine species can oxidize organic contaminants (M. H. Zhou and Lei, 2006; M. Zhou and Lei, 2006)

$$2Cl^- \leftrightarrow Cl_2 + 2e^- \quad (3.9)$$

$$Cl_2 + H_2O \leftrightarrow HOCl + H^+ + Cl^- \quad (3.10)$$

$$HOCl \leftrightarrow H^+ + OCl^- \quad (3.11)$$

$$Cl + {}^{\bullet}OH \rightarrow Cl + OH^- \quad (3.12)$$

*3.3.3 Regeneration efficiency*

The time needed to achieve 93 ± 7.2 % regeneration was 50 min for EEG-N-P. After 10 min 60 % regeneration efficiency was achieved. Compared to EEG-N-S, EEG-N-P only achieved 43 % regeneration efficiency in 5 minutes. This implies that a significantly longer regeneration time is required for EEG-N-P, suggesting that the process occurring during regeneration of both EEG is different. The longer time of regeneration will also have an impact on energy consumption; long time will require more energy and therefore the cost will increase. The calculated charge efficiency for the regeneration of MB in EEG-N-S is 5 C $mg^{-1}$ and 48 C $mg^{-1}$ for EEG-N-P.

After the initial adsorption, the EEG adsorbent underwent three cycles of regeneration and re-adsorption. The required time for regeneration was found to be different for the two EEGs. For EEG-N-S, 5 minutes of anodic regeneration were required to obtain a regeneration efficiency of above 93%, while at 3 minutes only 58 % regeneration efficiency as shown in figure 3.3. For EEG-N-P, longer regeneration times were required.

Figure 3.4 shows the regeneration efficiency of three cycles for both EEG. The regeneration efficiency of EEG-N-P after 50 minutes of regeneration was 104 ± 6.9 % in the first cycle, 110 ± 5.4 % in the second cycle and 83 ± 4.1 % in the third cycle. Regeneration efficiency higher than 100 % can be due to increase of surface area and thus an increase in the number of adsorption sites. This increase in regeneration efficiency after the first cycle of adsorption and regeneration has been previously

reported and corrosion was proposed as the cause of regeneration efficiencies higher than 100 % (Sharif *et al.*, 2017).

EEG-N-S was exposed to regeneration for 5 minutes and it showed a regeneration efficiency of 93 ± 7.2 % in the first cycle, 87 ± 7.7 % in the second cycle and 72 ± 2.7 % in the third cycle. It is possible that the shorter times of regeneration were not long enough time to corrode the graphene compared to the longer time needed to regenerate EEG-N-P. Corrosion of the EEG rather than dye oxidation could be another possible explanation of the short regeneration time.

According to figure 3.5, the regeneration efficiency of EEG-N-S decreased with each cycle; this may be related to the loss of material during vacuum filtration or during the regeneration. The amount of material lost during each cycle of regeneration was not measured in this study, as the amount of material was very low.

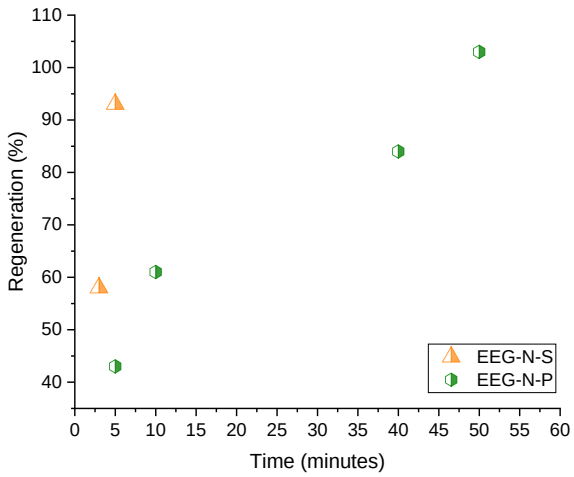


Figure3.4: Regeneration time needed for both EEG-N-S and EEG-N-P.

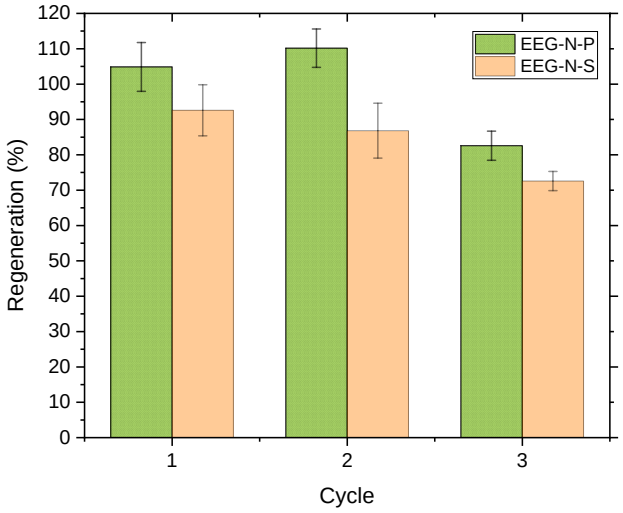


Figure3.5: Regeneration efficiency achieved in three cycles for EEG-N-S and EEG-N-P.

Heteroatom doping of graphene has showed benefits related to the oxidation of organic contaminants. The dual-doping of nitrogen and phosphorus in graphene-carbon nanosheets has been shown to be a great catalyst for oxygen evolution reaction (OER) and it was found that dual or multiple doping provided more benefits than single elements doping (Li *et al.,* 2015). This shows great importance and useful data because OER on the surface of the electrode is essential in the electrochemical degradation of organic compounds as a result of the creation of hydroxyl radicals, along with the electrochemical reactivity of the electrode (Kapalka *et al.,* 2010). As mentioned earlier, the oxidation of dyes, in this case methylene blue is improved with the presence and creation of $^{\bullet}OH$ radicals, this suggests that the doping of heteroatoms enhances a rapid oxidation and likely shorter regeneration times.

X-ray diffraction (XRD) analysis was performed in order to study the crystallinity of the samples and study changes before and after corrosion. Appendix 13 shows the x-ray diffraction spectra and Appendix 14 shows the peak shifts. EEG-N-S showed almost no shift in the 002 peak, while EEG-N-P showed a very low shift of around 0.01 2theta degrees. This suggests that crystallinity in both adsorbents did not change significantly after 145 minutes exposure to electrochemical regeneration.

### 3.4 Conclusions

Differences in adsorption capacity were achieved when using two different EEGs. EEG-N-P showed a higher adsorption capacity than EEG-N-S with both cationic and anionic organic dyes (MB and MO respectively). The adsorption capacities achieved by this type of graphene is comparable to that reported in the literature for other types of graphene (Kim *et al.*, 2018) and higher than graphene composites. As expected, the adsorption capacity of the MB was significantly higher.

The regeneration of 100 % of EEG-N-S was achieved in a much shorter time compared to EEG-N-P, with an order of magnitude increase in the regeneration time required to achieve complete regeneration for EEG-N-P. At the end of the third cycle, EEG-N-S has been exposed to high voltages for only 15 minutes, while EEG-N-P has been exposed for 150 minutes. It is important to notice that the adsorption capacity of the EEG-N-P was more than twice the adsorption capacity of EEG-N-S, meaning that a higher amount of contaminant is present in the EEG, therefore a greater amount of contaminant must be oxidized. The charge efficiency of both EEG also showed that a significantly higher amount of energy will be consumed in the regeneration of EEG-N-P compared to EEG-N-S, this suggests that the EEG-N-S may be a better adsorbent, with lower adsorption capacity but lower cost of regeneration.

These two different EEGs have been previously characterized; both graphene showed similar C/O ratio according to XPS. It is interesting to see that doping of graphene with less than 2% sulfur and nitrogen heteroatoms can change the properties of the EEG and impact greatly on the adsorption capacity and the regeneration time necessary to achieve complete regeneration.

Further work is needed in order to further investigate the regeneration mechanism for the EEGs. Surface area analysis after regeneration of graphene should be carried out to define if new adsorption sites were created. Chemical oxygen demand is another test that can be performed to determine if corrosion products were present after accelerated corrosion tests and evaluate the stability of EEG. Previous studies have exposed the graphene material to electrochemical oxidation without any adsorbate, after the oxidation, the material was washed and filtered. The Chemical oxygen

demand of the filtrates and untreated graphene was compared (Sharif *et al.*, 2017). An increase of COD will indicate oxidation. TEM and XPS characterization of the regenerated material would provide information about changes in morphology and elemental composition.

## Chapter 4. Corrosion of electrochemically exfoliated doped-graphene

### 4.1 Introduction

Carbon materials are used for several applications, including catalyst support in fuel cells, electrodes in batteries and capacitors (Forouzandeh *et al.*, 2018), as well as in water treatment using carbon as adsorbent (Sharif *et al.*, 2017). Carbonaceous materials tend to experience carbon corrosion, which decreases their lifetime when used in some of these applications. The cause of the corrosion is due to the thermodynamic instability of carbon when it is exposed to oxidative conditions (Qiao *et al.*, 2018). Most studies on corrosion mechanism in carbon materials have focused on highly porous and disordered materials used as catalyst supports for fuel cell electrodes and supercapacitors (Yu *et al.*, 2015). Vulcan carbon, reinforced-graphene (Castanheira *et al.*, 2015), ordered mesoporous carbon (Pérez-Rodríguez *et al*., 2019) and carbon black (Shao *et al.*, 2006) are some of the most studied materials. However, little work has been done to identify the corrosion mechanism in doped-graphene materials. Surface area, wettability and crystallinity are factors that impact the oxidation rate of the carbon material (Forouzandeh *et al.*, 2015). Carbons with a greater degree of crystallinity in their structure showed a higher corrosion resistance (Forouzandeh *et al.*, 2015). Thus, the corrosion resistance of graphene may differ from already established results obtained with frequently studied amorphous carbons.

Several protocols have been used to oxidize carbon materials and study their resistance to corrosion such as: electro-Fenton (EF), anodic oxidation (AO) assisted $O_2$ oxidation (Qiao *et al.*, 2018) and potential holding steps (Kangasniemi *et al.,* 2004). Kangasniemi and co-workers studied surface electrochemical oxidation of Vulcan carbon at different temperatures by holding the potential at 1.2 V vs. RHE for up to 120 hours under fuel cell conditions. This was repeated for various potential values in order to fully understand corrosion kinetics on the material surface (Kangasniemi *et al.,* 2004).

In a similar study, corrosion of carbon black and carbon nanotubes was also studied using potential holding process for 120 hours at 1.2 V vs. RHE (Shao *et al.*, 2006). This approach is an option for studying the oxidation in carbon materials.

However, it has been reported that applications of potential steps results in higher carbon oxidation current compared to potential holding (Shao *et al.*, 2009a). Moreover, potential stepping provides the advantage that the voltage window can be changed; an increase between the lower and upper potential limits has also shown an increase in the oxidation current and therefore enhances carbon corrosion (Shao *et al.*, 2009b). Castanheira et al. (2015) carried out similar accelerated stress tests to study the corrosion resistance of high surface area carbons. Potential steps to different values ranging from 0.6 V - 1.5 V vs. RHE were applied for 96 hours (Castanheira *et al.*, 2015). It was concluded that the type and concentration of the oxygen-containing functional groups produced by the oxidation reactions were dependent on the potential applied during the accelerated stress tests (Castanheira *et al.*, 2015).

Cyclic voltammetry (CV) is one of the main techniques used to analyze and estimate the degree of corrosion in carbon materials. In acidic media, redox peaks corresponding to electroactive oxygen-containing surface groups are visible, and they increase in area with the time of exposure to carbon oxidation conditions (Kangasniemi *et al.,* 2004). However, CV may not be the best option for quantitatively analyzing corrosion. Although, CV provides information about the amount of electroactive surface functional groups and variations in the electrochemical surface area, it does not provide data on carbon losses due to oxidation (Forouzandeh *et al.*, 2018). It is important to note that CV of carbon materials can be affected by wettability, the amount of surface functional groups and the existence of micropores (Forouzandeh *et al.*, 2018).

Accelerated corrosion studies methods are usually time-dependent and last for long periods of time; for e.g. 96 hours (Castanheira *et al.*, 2015), 120 hours (Kangasniemi, *et al.,* 2004) (Shao *et al.*, 2006) or 168 hours (Wang *et al.*, 2006). For this reason, shorter corrosion protocols have been used based on a fuel cell environment, simulating conditions where high potentials are reached during a start/stop operation. (Forouzandeh *et al.*, 2018).

These fuel cell-based corrosion studies have been performed to study mesoporous colloid imprinted carbon (CIC) (Forouzandeh *et al.*, 2018), Vulcan carbon (VC)

(Forouzandeh *et al.*, 2018) and ordered mesoporous carbons (OMCs) (Forouzandeh *et al.*, 2015) using a short accelerated corrosion protocol consisting of several potential steps and CV in an acidic electrolyte. In order to study the corrosion rate, these studies (Forouzandeh *et al.*, 2015) used cyclic voltammetry (CV) to calculate the changes in capacitance of different carbons, before and after the accelerated corrosion tests by using the following expression to determine capacitance (Forouzandeh *et al.*, 2015):

$$C_G = \frac{A}{2\mu m \Delta V} \qquad (4.1)$$

Where:

$C_G$= gravimetric capacitance (F $g^{-1}$)

$A$= integrated charge from CV (A ·V)

$\mu$= scan rate (V $s^{-1}$)

$m$= mass of graphene deposited on Glassy Carbon surface (g)

$\Delta V$= potential window (V)

The method used to analyze the corrosion resistance by using an accelerated corrosion protocol is a promising tool for studying different carbon materials. Most corrosion studies were performed in acidic media; however, when other alkaline or neutral media were used to study corrosion resistance, the mechanism of carbon oxidation changed (Yi *et al.*, 2017). It was found that the oxidation mechanism was faster on alkaline media, and the lowest oxidation kinetics was found to be in neutral media; at low pH oxidation led to the formation of surface oxides while at high pH the mechanism was oxidation and dissolution (Yi *et al.*, 2017).

For water treatment, graphene can be used as an efficient adsorbent that can be regenerated and reused (Sharif *et al.*, 2017; Sharif and Roberts, 2020). Previous studies by Sharif *et al*. demonstrated graphene adsorption and electrochemical regeneration with graphene-based composites containing magnetite-$Fe_2O_3$ (Sharif *et al.*, 2017) and anatase-$TiO_2$ (Sharif and Roberts, 2020). The results showed an increase in adsorption capacity as compared to the pristine graphene material. The extent of corrosion/oxidation of the material before and after the regeneration as well as the subsequent loss of adsorbent was related to the mass fraction of iron oxide loading

and the annealing temperature of titanium oxide respectively. These discoveries suggest that there is a need to further explore graphene materials with higher corrosion resistance to ensure longer cycling lifetime of the material during regeneration.

Another promising route for improving the corrosion resistance of graphene-based materials is through the insertion of different heteroatoms via electrochemical synthesis. It is expected that the presence of heteroatoms in the $sp^2$-lattice will effectively tune the intrinsic properties of pristine graphene.

Electrochemically exfoliated graphene (EEG) with phosphorous-doping has shown high thermal stability according to TGA analysis (Sharif *et al.*, 2020). The thermal stability was found to be linked to the C-P bonding effect which provides some form of oxidation resistance (Oh, S.G. Rodriguez, 1993). The presence of nitrogen doping in graphene has also shown significant improvement in its electrical conductivity (Li *et al*., 2015). Thus, it will be interesting to further study other material properties to determine if doping of carbon with other similar atoms will affect the corrosion resistance.

The current study aims to perform a quantitative analysis of the corrosion resistance of nitrogen-phosphorous-doped electrochemical exfoliated graphene (EEG-N-P) and nitrogen-sulfur-doped electrochemical exfoliated graphene (EEG-N-S) with an accelerated corrosion method performed in both acidic and neutral media.

The doped-graphene materials will be used in water treatment application as adsorbents being exposed to high cell voltages values with an electrochemical regeneration step applied after adsorption. Thus, a high corrosion resistance is essential in order to withstand such high applied potentials.

## 4.2 Experimental methods

### *4.2.1 Materials*

All chemicals were used as received without further purification. Deionized (DI) water was used for the preparation of the aqueous electrolytes, graphite foil ($5 \times 1$ $cm^2$, 0.05 cm thick, 99.8% purity, metal basis) was purchased from Alfa Aesar, manufactured by Thermo Fisher Scientific Chemicals, ammonium sulfate $(NH_4)_2SO_4$ 99.5% purity and ammonium phosphate $(NH_4)_2HPO_4$ 99-100% purity were purchased from VWR Canada.

### *4.2.2 Graphene synthesis*

Electrochemical exfoliated graphene (EEG) was synthesized via a one-step exfoliation technique using two different aqueous electrolytes composed of 0.1 M ammonium sulfate $(NH_4)_2SO_4$, and 0.1 M ammonium phosphate $(NH_4)_2HPO_4$ (Momodu *et al.*, 2021).

For the graphene synthesis a graphite foil with an exposed area of 16 $cm^2$ was used as the anode, and 16 $cm^2$ stainless steel grade 316 was used as the cathode. The electrodes were immersed in 300 ml of electrolyte solution. The separation distance between the cathode and anode was fixed at 1.5 cm. A different time for complete exfoliation was recorded for each electrolyte at an applied current density of 200 mA $cm^{-2}$ (or 3.2 A).

After complete exfoliation, the solution containing EEG and unexfoliated graphite was filtered and washed several times with DI water, using a vacuum filter with a 0.1 µm cellulose membrane filter in order to remove the remaining unreacted salts. The washed powder was re-dispersed in DI water, and sonicated for 30 minutes using a sonication bath.

Subsequently, the dispersed product was centrifuged (Avanti J-26S) at 2,000 rpm for about 5 minutes to separate unexfoliated graphite from the EEG. The precipitate was discarded, and the supernatant was centrifuged at 20,000 rpm for 30 minutes to recover the graphene particles. Finally, the product was freeze-dried to obtain the final EEG powder for characterization.

*4.2.3 Materials Characterization*

Sample characterization was performed to determine the material properties of the synthesized EEG, such as the nature of defects, doping content, morphology and textural properties.

X-ray photoelectron spectroscopy (XPS) was carried out to obtain information about the doping of heteroatoms and surface elemental composition on the exfoliated graphene samples. A Kratos Axis ULTRA photoelectron spectrometer (Kratos Analytical Limited, UK) was used with high resolution scans obtained at lower step-sizes and pulse energies over a longer duration.

The textural analyses were performed with a Micromeritics Gemini VII nitrogen-sorption analyzer on equal masses of pre-weighed exfoliated graphene samples in quartz tubes. Degassing was performed prior to the actual analysis by heating for 18 hours in a flow of nitrogen gas at 110 °C. Specific surface area (SSA) and pore-size distribution (PSD) measurements were obtained using the Brunauer–Emmett–Teller (BET) and Barrett–Joyner–Halenda (BJH) models, respectively.

Raman spectroscopy of the samples was performed to confirm the successful exfoliation of graphite sheets into graphene and to determine the quality of the exfoliated material in terms of the defects content. A WITec Alpha 300R confocal micro-Raman instrument was used, operated with a 532 nm laser at 5.0 mW power.
Raman analysis was also performed after the corrosion tests and after the electrochemical regeneration of graphene to compare the changes in the defects and graphene structure.
The sample preparation for Raman tests involved dispersing the exfoliated graphene powder in ethanol, with a sonication step for 5 minutes to evenly disperse the flakes, followed by drop-casting of the suspension on a silicon wafer substrate. Raman mapping and imaging was carried out on a $5 \times 5\ \mu m^2$ area, with a 100x microscope objective. The peaks obtained were deconvoluted and fitted to a Lorentzian function using the WITec Project 5 software.

Scanning Electron Microscopy (SEM) was used to observe the surface morphology of the EEG samples, using a Phenom ProX Desktop SEM system operated at 15 keV. A JEOL (JEM-ARM200CF Atomic Resolution) Transmission Electron Microscope (TEM) was used to obtain high magnification micrographs of the graphene flakes as well the associated selected area diffraction patterns (SAEDs) to estimate the number of layers.

### *4.2.4 Accelerated corrosion experiments in acidic media*

The corrosion resistance of the EEG was evaluated using a method adapted from prior studies (Forouzandeh *et al.*, 2015) to determine the corrosion resistance of carbon materials in acidic medium. The method was originally employed for analysis related to fuel cell technology, where an acidic environment is needed. In this work, the corrosion resistance was evaluated using a variety of electrochemical methods to determine the electrochemical stability of the EEG samples.

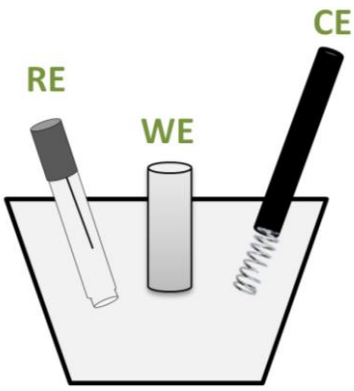


Figure 4.1: Three-electrode cell configuration used for accelerated corrosion tests.

For the test, a three-electrode cell configuration (Figure 4.1) was assembled composed of a platinum wire counter electrode (CE), saturated calomel electrode (SCE) reference electrode (RE) and glassy carbon (GC) working electrode (WE). Graphene was deposited on the GC surface by drop casting 50 µL of graphene suspension (1 mg $ml^{-1}$ solution of graphene in ethanol) on the GC surface; the GC was then dried to remove the ethanol.

A 0.5 M aqueous $H_2SO_4$ was used as electrolyte. Before each test, the electrolyte in the cell was de-aerated for 20 minutes by bubbling argon into the solution, after which the argon was supplied at the top of the cell where no electrolyte was present during the

entire test. In order to extract the gas trapped in the GC surface after being drop-casted, the GC was kept in vacuum for 5 min. After this procedure, no bubbles were observed on the graphene at the beginning of each test.

Electro-analytical experiments were performed to analyze the electrochemical properties of the EEG samples drop-casted on the GC substrate. Cyclic Voltammetry was carried out from a potential of −0.2 V to 0.85 V (vs SCE) at a scan rate of 10 mV $s^{-1}$. After the first set of CV scans, an accelerated corrosion procedure was applied to corrode the drop-casted graphene material and estimate the corrosion current.

The corrosion procedure consisted of 18 potential steps from 0.55 V (10 s) to 1.4 V (50 s) vs. SCE (Forouzandeh *et al.*, 2018). This high potential was used to promote fast oxidation of the carbon. During regeneration, graphene is exposed to high potentials around 3 V vs. SCE. For this reason a relatively high potential of 1.4 V vs. SCE was used for corrosion tests, higher potentials were not used to prevent damage of the glassy carbon electrode. The last set of CV test was completed after the corrosion tests with the same conditions as the initial CV cycles to analyze the nature of electrochemical changes on the drop-cast GC surface as shown in Figure 4.2.

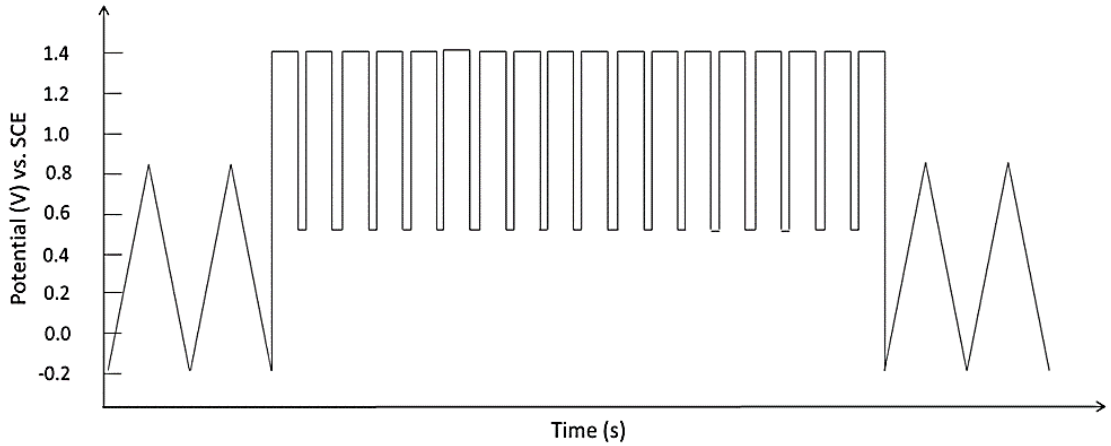


Figure 4.2: Corrosion tests protocol, CV and potential steps.

The upper potential limit was slightly modified from that used by Forouzandeh et al. (2015) (1.15 V vs. SCE) (Forouzandeh *et al.*, 2018). These values of upper limit in both studies were selected in order to ensure that carbon oxidation was likely, as it is known that an increasing potential values in aqueous electrolyte systems above the

potential for oxygen evolution (> 1.23 V vs. SHE at pH 0), will lead to the oxidation of the carbon (Yi *et al.*, 2015).

Equation 4.1 was used to calculate the capacitance from CV. A scan rate of 0.01 V $s^{-1}$ was used for the CV test, the mass of graphene was calculated to be 0.0005 g, the upper limit was 0.85 V vs. SCE and the lower limit was -0.2 V vs. SCE.

Anodic gravimetric charge was obtained by integrating the total charge after each potential step from 0.55- 1.4 V vs. SCE.

$$Q_{+} = \frac{\int_{t_a}^{t_c} I \, \mathrm{d}t}{m} \qquad (4.2)$$

Where:

$Q_+$ = anodic gravimetric charge (C $g^{-1}$)

$I$ = current (A)

$t$ = time

$t_a$= time at which the potential is switched to 1.4 V vs. SCE

$t_c$= time at which the potential is switched from 1.4 V to 0.55 V vs. SCE

$m$ = mass of graphene (g)

The total anodic charge was calculated from the integration of the area under the current-time curve of the all the 18 anodic steps from 0.55 to 1.4 V vs. SCE. Similarly, the total cathodic gravimetric charge was obtained by integrating the area under the current-time curve of the all the 18 cathodic steps from 1.4 to 0.55 V vs. SCE.

Cathodic gravimetric charge: integrated charge from potential steps (cathodic current) 1.4 to 0.55 V vs. SCE.

$$Q_{-} = \frac{\int_{t_c}^{t_a} I \, \mathrm{d}t}{m} \qquad (4.3)$$

Where $Q_-$ = cathodic gravimetric charge (C $g^{-1}$)

It was assumed that during the anodic steps oxidation of graphene and double layer charging occur, while during cathodic steps only double layer discharging occurs. Thus,

the difference between the anodic and cathodic charge gives the gravimetric charge due to graphene corrosion.

The corrosion gravimetric charge was estimated by subtracting the calculated cathodic gravimetric charge (negative) from the anodic gravimetric charge:

$$Q_C = Q_+ + Q_- \quad (4.4)$$

Where:

$Q_C$=Corrosion gravimetric charge (C $g^{-1}$)

The corrosion mass loss can be estimated from the corrosion gravimetric charge based on Faraday's law (equation 4.5), assuming that carbon was oxidized only to $CO_2$ (requiring 4 electrons per carbon atom).

$$\text{Ш} = \left(\frac{Q_C}{4F}\right) \text{x } Mc \text{ x } 100\% \quad (4.5)$$

Where:

Ш =Corrosion mass loss (%)

*Mc* = atomic mass of carbon (12 g $mol^{-1}$)

*F*= Faraday's constant 96485 C $mol^{-1}$

The corrosion charge can be normalized based on the real-time electrochemically active surface area (ECSA), =which is proportional to the cathodic gravimetric charge ($Q_-$).

$$Q_{C\ ECSA} = \left(\frac{Q_C}{Q_-}\right) \quad (4.6)$$

Where:

$Q_{C\ ECSA}$= Corrosion gravimetric charge per real-time ECSA, normalized charge.

This method to compare the amount of corrosion of carbon materials is convenient for obtaining quantitative results. However, it has not been widely adopted for corrosion studies in the literature, and data on the corrosion resistance of carbons is limited. For this reason, the EEG-N-P and EEG-N-S samples were also studied with commonly used methods, such as the peak separation for redox reactions observed with cyclic

voltammetry before and after corrosion, or electrochemical impedance spectroscopy (EIS).

Cyclic voltammetry with a redox couple added in solution was not used in acid conditions since the interest was to analyze the peaks related to quinone-hydroquinone and not changes in $Fe(CN)_6^{-3}/^{-4}$ redox couple. If a redox couple is added in acidic media tests, then the quinone-hydroquinone peaks are hidden by the $Fe(CN)_6^{-3}/^{-4}$ redox couple, as shown in figure appendix 17, and changes to the quinone functional groups will not be visible.

*4.2.5 Accelerated corrosion experiments in neutral media*

A second method for studying corrosion resistance was performed in order to compare the previous studies in the literature. Contrary to the study in acidic media discussed in section 4.2.4, a redox couple was added for this method. This second investigation will enable evaluation of the corrosion resistance of the two doped EEGs and compare the trends observed from the experiments in acidic media discussed in section 4.2.4.

Since it has been shown that corrosion behavior can vary depending on the media (Yi *et al.*, 2017) (Bauer *et al.*, 2020), a neutral media was used to compare the corrosion resistance of the two different EEGs. An aqueous solution of 1 M $Na_2SO_4$ was used as the neutral electrolyte with 5 mM $K_3Fe(CN)_6$ added to provide the redox couple. The redox couple $Fe(CN)_6^{-3}/^{-4}$ was used as it has been adopted in corrosion studies (Yang *et al.*, 2018; Qiao *et al.*, 2018; Kusmierek, 2019; Yi *et al.*, 2015) to analyze the variations in microstructure of the carbon material due to carbon oxidation reaction (Yang *et al.*, 2018). This redox couple is sensitive to the condition of the carbon surface (Chen *et al*., 1995; Chen and Mccreery, 1996). For this reason, in this study $Fe(CN)_6^{-3}/^{-4}$ was used to track changes of the carbon surface before, during and after the potential steps.

For this study, the accelerated corrosion conditions were similar to those used for acid conditions (section 4.2.4), with CV analysis carried out before and after the potential steps. The 18 potential steps were divided into three sections with each set of six potential steps followed by EIS performed to analyze changes in the kinetics of charge

transfer related to the corrosion of the material. EIS was performed at a fixed potential of 0.2 V vs. SCE after the electrode had been held at the low potential (0.55 V) step, in the frequency range of 100 kHz - 10 mHz.

The CV before and after the corrosion protocol were compared and the separation between the cathodic and anodic peaks in the CV ($\Delta E_p = E_{pa} - E_{pc}$) associated with the $Fe(CN)_6^{-3}/^{-4}$ redox couple was determined. The peak separation $\Delta E_p$ can be used to estimate the charge transfer kinetics, and changes in $\Delta E_p$ are associated with the oxidation or corrosion of the carbon surface (Nicholson, 1965).

### *4.3 Results and discussion*

#### *4.3.1 Characterization of the materials*

The exfoliated doped-graphene samples were characterized using XPS; the elemental composition is presented in Table 2.2 (the XPS scans are shown in Appendix 5) and the discussion can be found in chapter 2.

Surface area measurements were performed and the values of surface area obtained as shown in table 4.1 are lower than theoretical specific surface area of graphene; it is possible that graphene is aggregated and that BET measurement results did not provide a real surface area of dispersed graphene as it is known that aggregation of graphene nanosheets can cause obstruction of the adsorption sites (Yang *et al.*, 2011).

Table 4.1: surface area of EEG-N-P and EEG-N-S.

| **Carbon** | **BET surface area** $m^2\ g^{-1}$ |
|---|---|
| EEG-N-S | 17.94 |
| EEG-N-P | 10.35 |

TGA analysis showed the expected higher thermal stability in EEG-N-P. A superior thermal stability is observed in the entire temperature range (figure 4.3). A discussion on TGA can be found in chapter 4. However, this image is used to illustrate the differences in the thermal stability of the two samples studied in this chapter only.

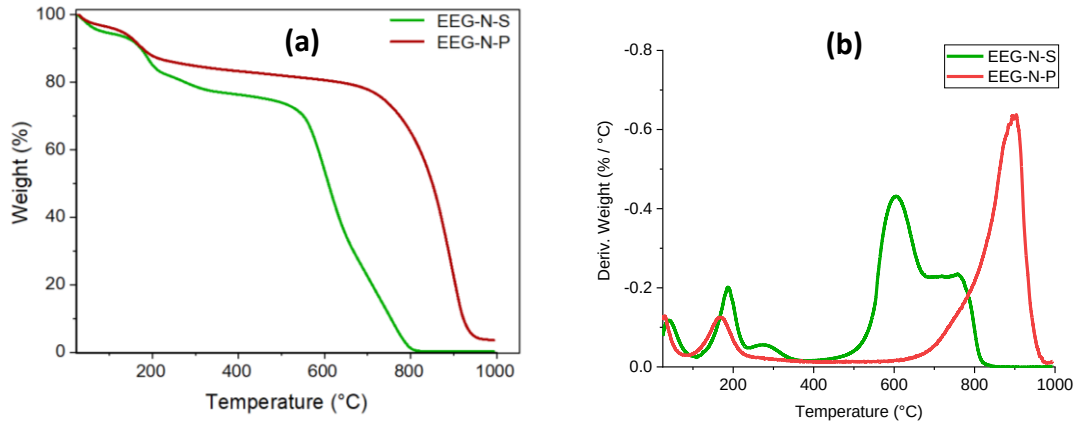


Figure 4.3: (a) TGA curve and (b) derivative weight loss of EEG-N-S and EEG-N-P in air.

Raman spectroscopy was used to obtain structural information for the EEG samples, as shown in Figure 4.4. The peak at around 1580 $cm^{-1}$ is known as the G band, it is associated with in-plane vibration of $sp^2$ bonded carbon (Ambrosi *et al.*, 2014). The peak observed at a Raman shift of approximately 1360 $cm^{-1}$ is the D band, which originates from out-of-plane vibrations of $sp^2$ carbon and it is activated when defects are present, such as edges, vacancies and $sp^3$ carbons (Ambrosi *et al.*, 2014). Doping of heteroatoms can also generate defects such as vacancies (Lee *et al.*, 2014).

The $I_D/I_G$ ratio is often used to characterize the amount of defects in the graphene. The $I_D/I_G$ ratio was 1.58 ± 0.07 for EEG-N-S and 1.68 ± 0.16 for EEG-N-P, suggesting that there were slightly fewer defects in the EEG-N-S graphene structure. This can be related to the higher percentages of doping found in this exfoliated graphene.

Table 2.2 presents the percentages of doping and carbon/ oxygen ratios found in EEG samples. XPS discussion can be found in chapter 2 and XPS deconvolution is included in appendix 6.-8.

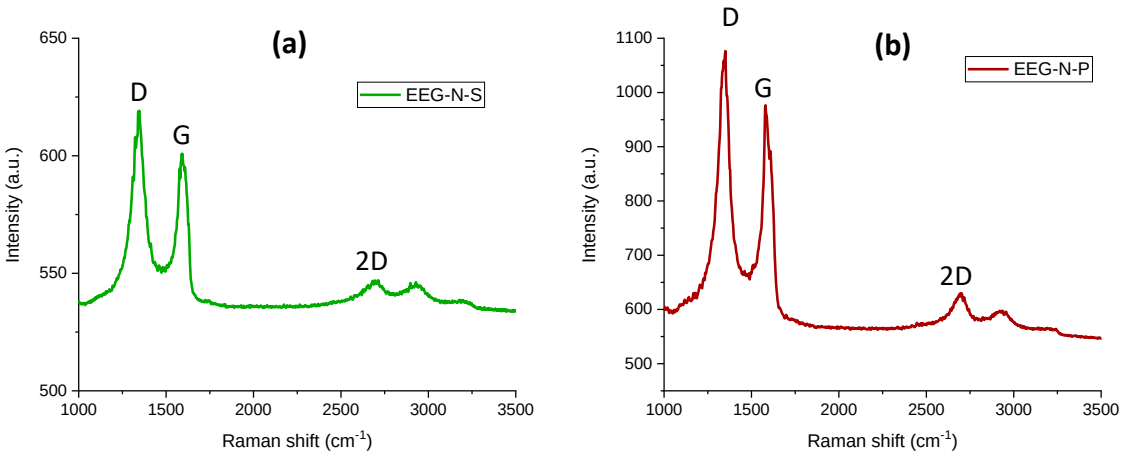


Figure 4.4: Raman spectra of (a) EEG-N-S and (b) EEG-N-P.

### *4.3.2 Accelerated corrosion tests in acidic media*

#### *4.3.2.1 Cyclic voltammetry*

The CV for the doped-graphene samples were compared before and after the accelerated corrosion as shown in figure 4.5. Changes in the CV were observed for the doped-graphene, with an increase in the redox peaks at a potential of around 0.33 V vs. SCE after corrosion. These peaks are associated with quinone/hydroquinone (Q/HQ) redox reactions (Kinoshita, K., 1973). The magnitude of the peaks is related to the oxygen functional groups present on the graphene surface. The increase in the current response of the CV could also be a result of increased electrode wetting (Shao *et al.*, 2009a), the amount of surface functional groups, and the development of micropores (Forouzandeh *et al.*, 2018).

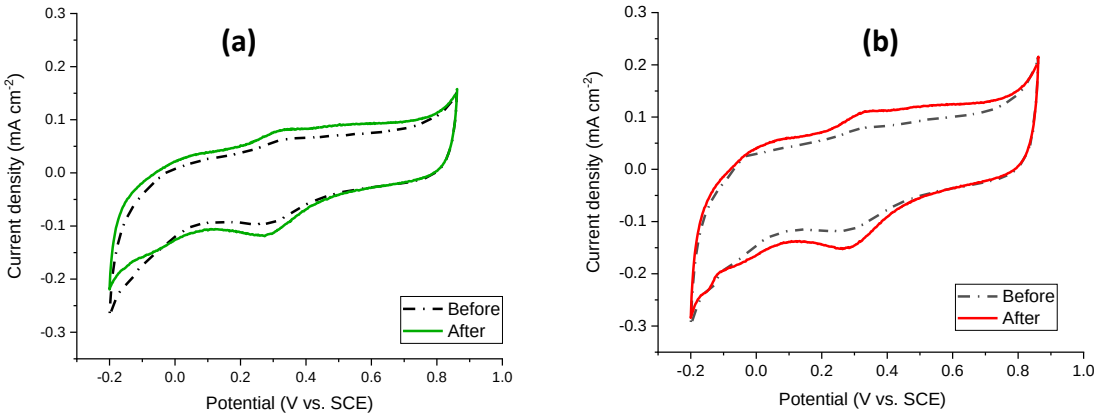


Figure 4.5: CV before and after accelerated corrosion test (a) EEG-N-S (b) EEG-N-P in acidic media 0.5 M $H_2SO_4$ at a scan rate of 10 mV $s^{-1}$.

The calculated increase in gravimetric capacitance obtained using equation 4.1 for the CV before and after potential steps (Table 4.2), showed a higher increase for the EEG-N-P capacitance as compared to the EEG-N-S, this can be seen directly from figure 4.5 where EEG-N-P increase in peaks related to of electroactive oxygen functional groups is more evident. Another possible reason for the higher increase of gravimetric capacitance of EEG-N-P may be related to the properties of the dual-doping of nitrogen and phosphorus on graphene - carbon nanosheets (Li *et al*., 2015) .

Table 4.2: Capacitance EEG samples obtained from CV (–0.2 to 0.85 V vs. SCE, 10 mV $s^{-1}$) before and after corrosion tests by potential steps in 0.5 M $H_sSO_4$.

| **EEG sample** | **Before Corrosion** | | **After Corrosion** | **Percentage increase in the gravimetric capacitance** |
|---|---|---|---|---|
| Units | $C_{G,i}$ (F/g) | $C_{G,i}$ ($F/m^2$) | $C_{G,f}$ (F/g) | (($C_{G,i}$ -$C_{G,f}$)/$C_{G,i}$) x100 (%) |
| EEG-N-S | 13±1.08 | 0.72 | 15±1.13 | 15 ±1.33 |
| EEG-N-P | 18± 2.5 | 1.73 | 22± 3.37 | 23 ± 2.32 |

*4.3.2.2 Corrosion calculations from chronoamperometry tests (potential steps)*

From figure 4.6 the current response after each anodic potential was a current peak followed by a rapid decrease in current. It was assumed that the initial positive current is the result of double layer charging which is expected to be fast with a timescale of order milliseconds, and for most of the time that the electrode is held at 1.4 V vs. SCE the current is associated with carbon oxidation / corrosion, where carbon surface oxides and possibly CO and $CO_2$ are produced. In the case of the cathodic potential steps, the negative current peak shows a very rapid decrease in current due to the double layer discharging. Hence, the cathodic charge is considered to be proportional to the ECSA as a function of corrosion time (Forouzandeh *et al.*, 2015).

This trend of current/charge decay in both anodic and cathodic steps is similar to the findings for different types of carbons such as Vulcan carbon and ordered mesoporous carbons (Forouzandeh *et al.*, 2015).

The first few potential steps present the highest anodic charges, and the anodic charge decreases with the number of potential cycles. Figure 4.6 shows that the anodic currents in the last few potential steps at 1.4 V were similar. The decrease in the anodic current suggests that the rate of corrosion of the graphene decreased with the number of potential steps.

The formation of different surface functional groups and oxides has been suggested and this decrease in corrosion current until stabilization can be explained by the

creation of CO surface groups that passivate the graphene surface, and are followed by slow evolution of CO and $CO_2$ (Castanheira *et al.*, 2015).

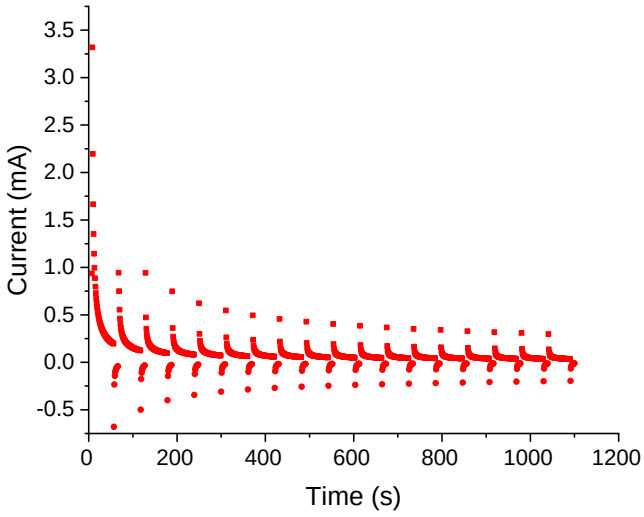


Figure 4.6: Current versus time data obtained from potential steps for EEG-N-P.

The carbon corrosion is believed to take place with different reactions as follows (Forouzandeh *et al.*, 2018):

Step 1: $C_s \rightarrow C_s^+ + e^-$ (4.7)

Step 2: $C_s^+ + H_2O \rightarrow C_sO + 2H^+ + e^-$ (4.8)

Step 3: $2C_sO + H_2O \rightarrow C_sO + CO_2 + 2H^+ + 2e^-$ (4.9)

Step one represents the oxidation of the carbon surface (Cs), while step two shows the oxidized sites being hydrolyzed and forming oxidized carbon intermediates such as (CsO), quinone/hydroquinone. These surface groups can be oxidized once again with water being present and finally produce carbon dioxide in step 3 (Forouzandeh *et al.*, 2018).

The oxidation of graphene is likely similar to other carbon materials and as such, we adopted the proposed mechanism of corrosion for multiwall carbon nanotubes (MWCNTs) in acidic media (Yi *et al.*, 2015). The initial oxidation starts at the defective amorphous carbon on the surface of MWCNTs. After the oxidation of the disordered

structures, the graphitic layers are exposed and they experience oxidation until the carbon saturates with stable surface oxides preventing the creation of new oxides; this creates a passivation by surface oxides that protect the inner graphitic structure against more oxidation (Yi *et al.*, 2015). An identical mechanism was reported in the corrosion of high surface area carbon when potentials between 0.4 and 1.0 V vs. RHE were applied in a 0.1 M $H_2SO_4$ electrolyte; corrosion occurred on the disordered domains and defects, and when potentials higher than 1.0 V vs. RHE were applied, the ordered graphitic structures were also corroded (Castanheira *et al.*, 2014).

The charge during the positive and negative potential steps was integrated to obtain the anodic and cathodic gravimetric charge. From the difference of both charges, the corrosion mass loss was calculated assuming that all the carbon converts to $CO_2$ as shown in equation the following equation considering corrosion of carbon in acid medium (Kinoshita, K., 1988):

$$C + 2H_2O \leftrightarrow CO_2 + 4H^+ + 4e^- \quad E = 0.207 \text{ V vs. RHE} \qquad (4.10)$$

The $CO_2$ produced from corrosion of carbon was not measured in this study. CV data shows the evolution of products such as oxygen functional groups, this suggests that not only corrosion is happening; however the formation of these groups is neglected in this analysis. In reality, the assumed corrosion charge obtained is an oxidation charge. In addition, the increase in capacitance obtained from CV could have been influenced by morphology changes, flake roughening and wettability changes apart from oxidation/corrosion. For this reason, the charges obtained from potential steps were considered to more accurately reflect the corrosion resistance of carbons compared to CV data (Forouzandeh *et al.*, 2018).

The corrosion mass loss calculated from the charge passed during the potential steps (table 4.3) indicates that the mass loss observed for EEG-N-P was almost twice that for EEG-N-S. The trend observed is consistent with the change in capacity obtained from CV, which indicated that a larger increase in surface area occurred for EEG-N-P than EEG-N-S, indicating increased electrochemical corrosion. This result is the opposite of what was expected based on TGA data, since EEG-N-P showed higher thermal stability in air, and was expected to be more resistant to oxidation.

This accelerated corrosion method by using rapid changes in voltage (i.e. potential steps) with analysis of the current - time data may be a better option than CV for comparison of the corrosion resistance of different carbons (Forouzandeh *et al.*, 2015). With CV, other changes that may not be related to corrosion can affect the findings.

The corrosion gravimetric charge normalized with the real time ECSA has no units, since the corrosion gravimetric charge was divided by the cathodic gravimetric charge (assumed to be proportional to the real time ECSA), as shown in equation 4.6. Normalization to the ECSA is a useful indicator of corrosion rate, especially for electrochemical applications.

The corrosion gravimetric charge normalized to the ECSA was higher for EEG-N-P than EEG-N-S, however its value is not two times higher than EEG-N-S as suggested by corrosion mass loss. Thus the rate of corrosion is significantly higher for EEG-N-P than EEG-N-S, partly due to a higher ECSA (indicated by the larger cathodic gravimetric charge) and partly due to faster corrosion kinetics, indicating lower corrosion resistance.

Table 4.3: charges passed for EEG-N-S and EEG- N-P during 18 potential steps between 1.4 and 0.55 V vs. SCE, accelerated corrosion experiments carried out in an acidic solution.

| **Carbon** | **Anodic gravimetric charge** | **Cathodic gravimetric charge** | **Corrosion gravimetric charge** | **Corrosion mass loss** | **$S_{BET}$ normalized Corrosion charge** | **Corrosion gravimetric charge per real time ECSA** |
|---|---|---|---|---|---|---|
| Units | C/g | C/g | C/g | % | $C/m^2$ | |
| EEG-N-S | 1687 ± 69 | 1372 ± 73 | 315 ± 47 | 0.98±0.14 | 17.55 | 0.23± 0.03 |
| EEG-N-P | 2685 ± 603 | 2078 ± 651 | 606 ± 185 | 1.88±0.58 | 58.55 | 0.31± 0.12 |

*4.3.2.3 Sample characterization before and after corrosion*

From the electrochemical experiments, the corrosion resistance of carbons was calculated as well as the corrosion mass loss. The results were used to compare the corrosion resistance of EEG-N-P and EEG-N-S. Some results may not be comparable with studies of the corrosion resistance of high surface area porous carbons.

Differences in ink preparation may also affect the results, as a result of differences in the wettability (Forouzandeh *et al.*, 2015; Forouzandeh *et al.*, 2018).

In order to study the corrosion resistance Raman was one of the characterization techniques chosen to identify the two samples before and after the corrosion protocol. The $I_D/I_G$ ratio and $I_{2D}/I_G$ of the two samples was calculated before and after the corrosion and the results are shown in table.

Fewer defects were found on the graphene after corrosion. A greater decrease is found in EEG-N-P with a relatively high decrease in $I_D/I_G$ ratio. The EEG-N-S presented a smaller change on $I_D/I_G$ ratio as shown in in table 4.4. This result is consistent with the previous tests showing bigger corrosion impact on EEG-N-P.

Table 4.4: Raman $I_D/I_G$ ratio before and after corrosion studies in acidic media.

| **EEG** | **$I_D/I_G$ before corrosion** | **$I_D/I_G$ after corrosion** |
|---|---|---|
| EEG-N-P | 1.85 ± 0.16 | 1.18 ± 0.13 |
| EEG-N-S | 1.14 ± 0.20 | 1.11 ± 0.08 |

The EEG deposited on the glassy carbon was analyzed before and after the corrosion experiments using SEM, as shown in figure 4.7. With careful analysis it was possible to locate the same area of the electrode and observe changes in the morphology of the EEG. The images show that some flakes become detached after the accelerated corrosion experiments, as shown in figure 4.7 (b). In addition, a change in the morphology of a graphene flake can be observed by comparing figure 4.7 (c) and (d). Corrosion studies usually show TEM images (Borup *et al.*, 2007; Castanheira *et al.*, 2015; Yi *et al.*, 2015) of the carbons before and after the corrosion, however, observations of the morphology at the same location has not been studied before and after corrosion.

The changes in graphene before and after corrosion can be due to different processes. New oxygen functional groups may be formed under anodic potentials, and corrosion mass loss can lead to increases in surface area and hence an increase in the charge passed during CV. In addition, it is evident from the figure 4.7 that loss of carbon surface can occur, in this case by a flake detaching from the glassy carbon surface.

Thus corrosion can lead to both an increase surface area (due to increased roughness or porosity) or loss of carbon surface due to mass loss by detachment or oxidation to $CO_2$.

Surface modifications as a result of oxidation could have caused the flakes to detach from the glassy carbon, and morphology changes can be related to corrosion of the graphene as well.

Changes observed at higher magnification such as surface roughening or corrosion at the edges of graphene flakes were not possible observe by SEM, however, it has been reported that surface roughening and graphitic structure loss occurs on MWCNTs when they were exposed to electrochemical oxidation (Yi *et al.*, 2015).

The multiple processes happening during corrosion of graphene can affect the measurements. The detachment of flakes will decrease the amount of graphene in the glassy carbon surface and therefore will impact the measured surface area.

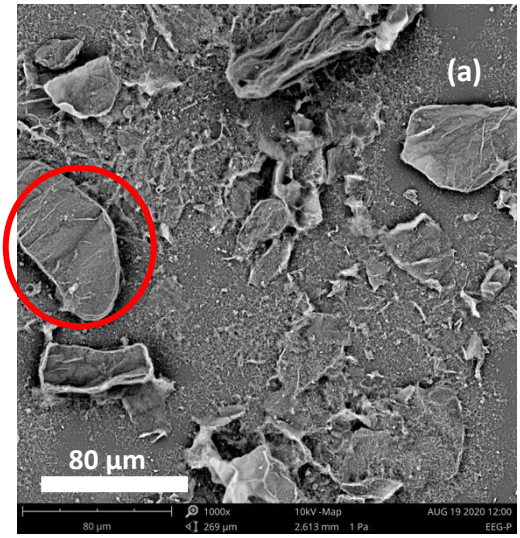


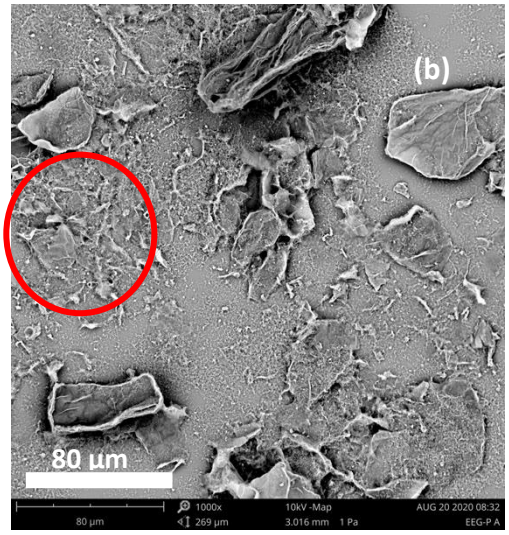

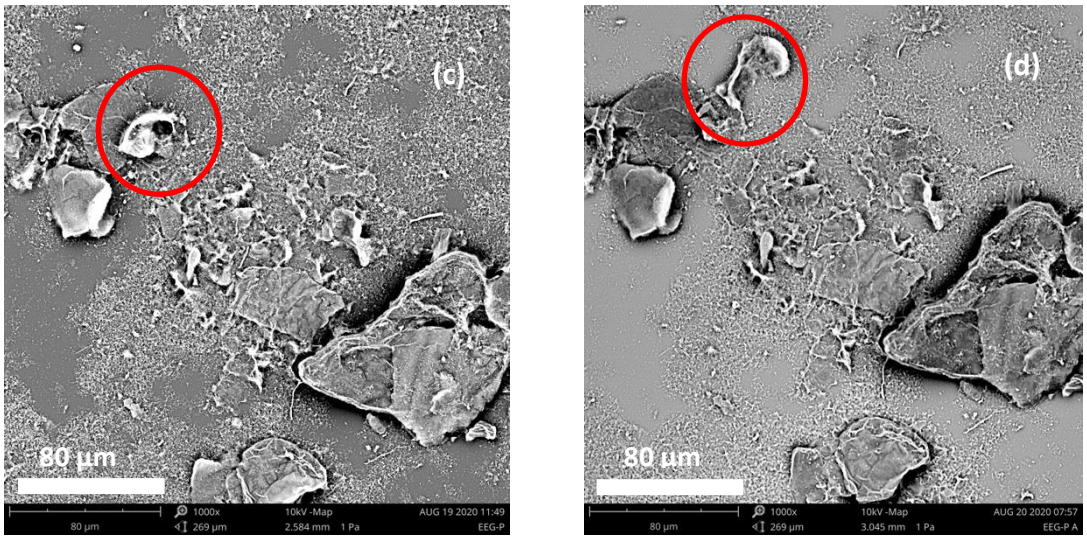


Figure 4.7: SEM images of the glassy carbon surface with dropcasted EEG-N-P (a,c) before, and (b,d) after corrosion, at the same location.

These SEM images also show that the glassy carbon surface may have been exposed during the accelerated corrosion test; appendix 23 and 24 shows the capacitance and charges obtained by the different EEG and a blank glassy carbon electrode (without graphene dropcasted on its surface).

The values of the glassy carbon charges suggest that the glassy carbon contributes significantly to the capacitance and charges considered to be due to corrosion. The contribution from the glassy carbon is more evident on capacitance data from cyclic voltammetry measurements. In addition, the corrosion charge of EEG-N-S and glassy carbon only was found to be very close, suggesting that the contribution of the glassy carbon electrode is considerable. Further experiments are needed to evaluate the glassy carbon impact on the corrosion resistance differences of the two studied EEG materials.

X-ray diffraction (XRD) analysis was performed in order to study the crystallinity of the samples and study changes before and after corrosion. Appendix 19 shows the diffraction spectrum and the peak shifts are shown in Appendix 20.

EEG-N-S showed almost no shift in the 002 peak while EEG-N-P showed a new peak, likely due to corrosion/oxidation of the EEG. The decrease in intensity of the peaks observed was probably due to lower sample mass after corrosion. These results are

consistent with the findings from Raman spectroscopy (table 4.4), where the level of defects was stable for EEG-N-S with minimal change for EEG-N-S and it was reduced significantly for EEG-N-P after corrosion.

*4.3.3 Accelerated corrosion tests in neutral media*

For the ACTs in neutral media, a range of scan rates was studied in order to choose the best parameters that captured significant changes in the CV before and after corrosion. The expected peak due to the redox couple Fe $(CN)_6^{-3}/^{-4}$ at around 0.21 V vs. SCE can be seen in figure 4.8 (a) for EEG-N-S. After corrosion, Figure 4.8 (b), the Fe $(CN)_6^{-3}/^{-4}$ redox peak was still evident, but one or more shoulder peaks can be observed at the low scan rates. The peaks are better defined at low scan rates, when the scan rate was 20 mV $s^{-1}$ or higher, the peak at ~ 0.17 V vs. SCE combined with the peak at ~0.24 V vs. SCE making it difficult to distinguish one peak from another and therefore the changes on peak to peak separation. For this reason, a scan rate of 10 mV $s^{-1}$ was selected to study the changes before and after the corrosion of graphene, as shown in appendix 15.

After corrosion of graphene, a blue precipitate was observed at the surface of the glassy carbon, and it is likely the origin of the peak observed in the CV after corrosion.
It has been reported that ferricyanide can be unstable under certain conditions (Lounasvuori *et al.*, 2014). The graphene nanoflakes may contain carboxylic acid groups, and acid formation in the boundary layer during oxidation may be sufficient to protonate the ferricyanide. This can lead to the loss of the cyanide ligand and the deposition of films analogous to Prussian blue (Lounasvuori *et al.*, 2014).

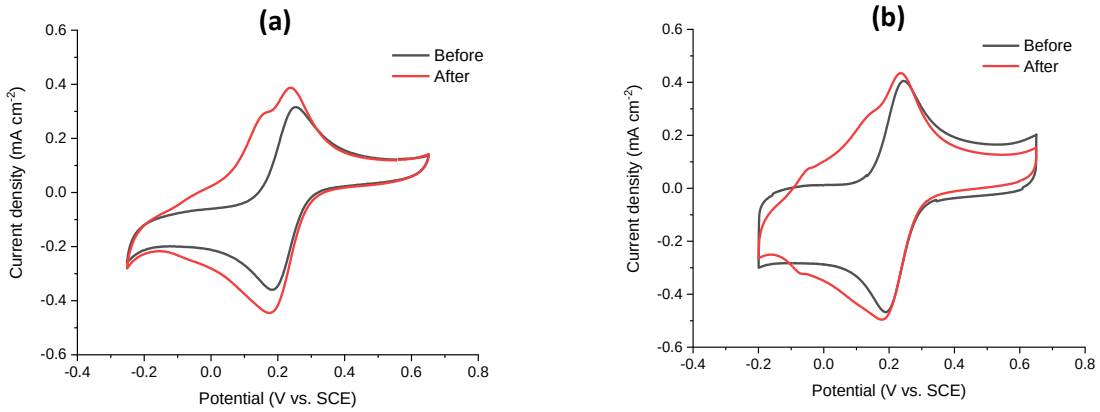


Figure 4.8: CV before and after accelerated corrosion test in 1 M $Na_2SO_4$ + 5 mM $K_3Fe(CN)_6$ electrolyte at 10 mV $s^{-1}$ (a) EEG-N-S (b) EEG-N-P.

New peaks are observed after corrosion of graphene, one new peak at ~ 0.17 V vs. SCE on EEG-N-S and two peaks at ~- 0.08 V vs. SCE and at ~ 0.12 V vs. SCE on EEG-N-P, this can be caused by new surface functional groups created as result of graphene oxidation. Appendix 16 shows the CV before and after corrosion of EEG-N-S in 1 M $Na_2SO_4$ electrolyte where no Fe $(CN)_6^{-3}/^{-4}$ redox couple was present. In this figure, the peaks from the CV are not shown, therefore, it can be assumed that they are related to changes on the redox couple Fe $(CN)_6^{-3}/^{-4}$ or possibly the changes were there but they were no visible as a result of the absence of it.

A peak separation analysis was performed for the before and after the corrosion test. In the case of EEG-N-P, the peak separation for the redox couple Fe $(CN)_6^{-3}/^{-4}$ increased from 69 mV to 70.75 mV, corresponding to an increase of 1.75 mV. For EEG-N-S, the peak separation increased by only 0.5 mV after corrosion.

These results suggests that carbon corrosion and the formation of oxides inhibits electron transfer as the peak to peak separation is related to the kinetics of heterogeneous electron transfer (Yi *et al.*, 2015). The change in the peak separation indicates a greater reduction of electrochemical activity for EEG-N-P in comparison to EEG-N-S.

Figure 4.9 (a) shows the Nyquist plot of EEG-N-S obtained from EIS during the corrosion experiments, in order to evaluate the changes to the EEG surface that occurred during the experiment. The Nyquist plot shows the variation of the

impedance from a high frequency of 100 kHz (high real impedance *Z'*) to a low frequency of 10 mHz (low *Z'*). At high frequency, a partial semicircle was observed, attributed to the dispersion effect (Wang *et al.*, 2014). The intersection of the impedance curve with the real axis (Z') at high frequency is the equivalent series resistance (ERS) value or solution resistance $R_1$ (Momodu *et al.*, 2015). This corresponds to the resistance of the electrolyte, contact resistance at the interface of the EEG and current collector, and the electrode internal resistance (Conway *et al*., 1997; Fan *et al.*, 2011).

The Nyquist plot of the EEG samples can be modeled using a modified Randles equivalent circuit (Randles, 1947) as shown in the image on figure 4.9. EIS data fitting was achieved by using the data fitting software ZFIT that uses the complex nonlinear square CNLS method (Conway, 1999) to fit the equivalent circuit elements to the EIS response of the electrode. The equivalent series resistance $R_1$ is in series with the constant phase element $Q_1$. The small semicircle observed in the high frequency region is associated with the charge transfer resistance $R_1$ and $Q_1$, which are connected in parallel (Momodu *et al.*, 2015).

The impedance of the constant phase element $Q_1$ can be expressed as follows:

$$Q_1 = 1/T(j\omega)^a \qquad (4.11)$$

Where

*T*: frequency independent constant (F $cm^{-2}$) $^a$.

$\omega$: angular frequency

*a*: exponent

The constant *T* is associated with the surface roughness and pseudocapacitive kinetics of the electrode; the exponent a can be within the range of $-1$ to 1, and is calculated from the slope of the log (Z') versus log (*f*) line at low frequency. When *a* is equal to 0, $Q_1$ is a pure resistor, when it is +1, $Q_1$ is as a pure capacitor, when it is –1 $Q_1$ is a pure inductor (Guan *et al.*, 2010). The charge transfer resistance ($R_1$) is a measure of the kinetic rate of the redox reaction at the electrolyte-electrode interface (Sluyters-Rehbach, 1994), and can be determined from the high frequency semicircle arc radius

(Wang *et al.*, 2014). A low value of $R_1$ indicates fast electron transfer and enhanced electrochemical kinetics. Figure 4.9 shows that the radius for the high frequency arc, and hence the value of $R_1$, increases with the number of cycles, indicating a decrease in the electrochemical kinetics for the redox couple.

The fitting of the Nyquist plot focused on the high frequency region as the aim of the study was to observe the changes in charge transfer resistance. The charge transfer resistance was observed to increase after each set of 6 potential steps for both EEG-N-P and EEG-N-S. This may be as a result of decrease in the number of active sites (i.e. lower ECSA), or the formation of an oxide layer at the surface, decreasing the charge transfer kinetics.

The data obtained from EIS is consistent with the changes of peak separation observed with cyclic voltammetry (see figure 4.8). EEG-N-P showed a higher change in peak separation than EEG-N-S, indicating slower kinetics. For the EEG-N-S the increase in the peak separation after corrosion was smaller than for EEG-N-P, indicating less corrosion /oxidation compared to EEG-N-P. The EIS data confirms this better corrosion resistance for EEG-N-S as there is a smaller increase in the electron transfer resistance compared to that observed for EEG-N-P.

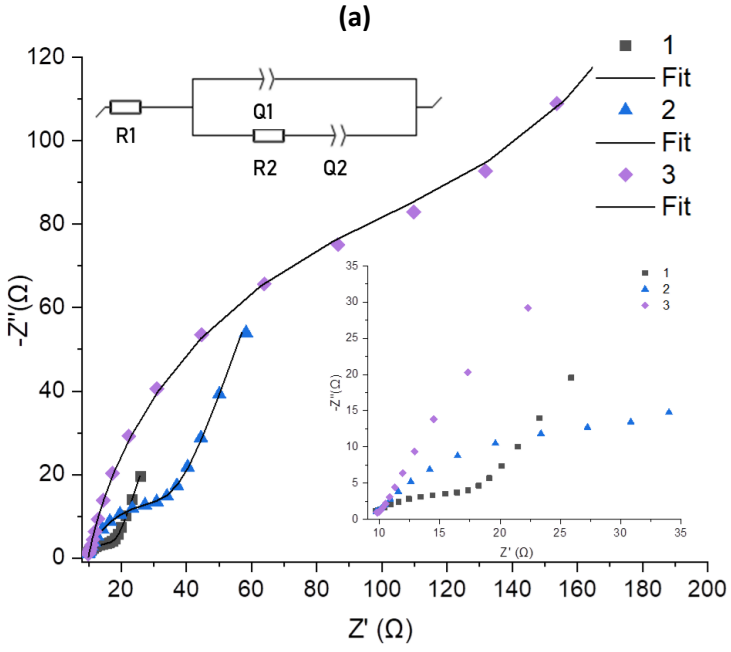

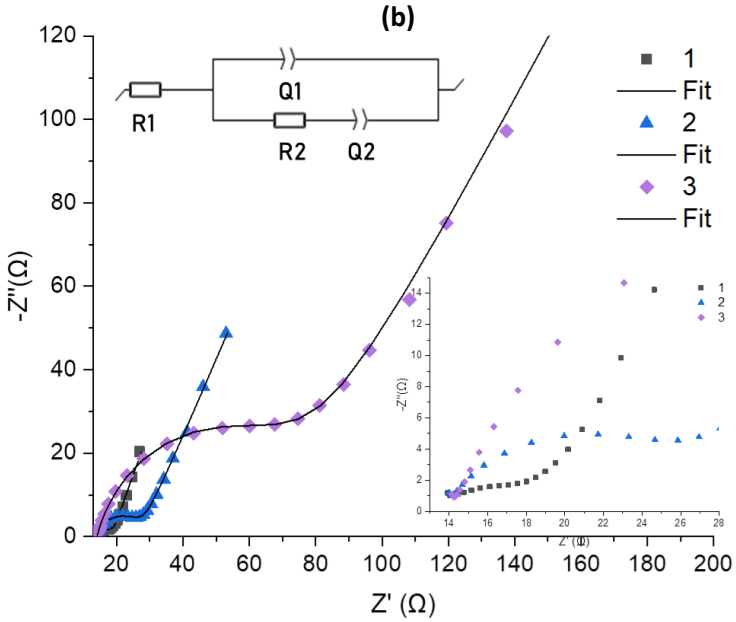


Figure 4.9: Nyquist plots from EIS in neutral media of (a) EEG-N-S (b) EEG-N-P performed at a fixed potential of 0.2 V vs. SCE, frequency range of 100 kHz - 10 mHz. Nyquist curve 1 was obtained after 6 cycles, curve 2 was after 12 cycles, and plot 3 was after 18 cycles of potential steps between 0.55 and 1.4 V vs. SCE. The inset plot shows a close-up of the Nyquist plot at the high frequency range.

### *4.3.4 Comparison between acidic and neutral media corrosion studies*

The corrosion studies of graphene in both acidic and neutral media indicated that the EEG-N-S has a slightly higher resistance to electrochemical corrosion / oxidation than EEG-N-P. The implication of these findings suggests that the large distortion caused by the additional P-doping in the carbon lattice allows open edge sites and produces wrinkles (Choi *et al.*, 2012; Li *et al.*, 2015); thus providing more defective sites and facilitating corrosion.

The main differences between the use of acidic and neutral electrolytes were observed in the CV data. The CV obtained in acidic media showed peaks related to an increase in capacitance due to the increase in surface groups on the surface. In neutral media, the peaks related to the redox couple Fe $(CN)_6^{-3}/^{-4}$ were studied.

The findings are consistent with a previous study that found an increase in capacitance and redox peaks around 0.55 V vs. RHE (0.306 V vs. SCE) during CV of glassy carbon in acidic media. The increased capacitance and redox peaks became more significant with increasing oxidation time (Yi *et al.*, 2017). In the case of neutral media, an increase in capacitance was observed, but no redox peaks were present (Yi *et al.*, 2017).

## 4.4 Conclusions

The corrosion study focused on the electrochemical corrosion resistance of two EEG materials doped with different heteroatoms. XPS analysis confirmed the doping of nitrogen, sulfur, and phosphorus in the EEG samples. A higher percentage of N-doping was observed in EEG-N-P than in the EEG-N-S.

The comparison of SEM images at the surface of the glassy carbon did not show evidence of significant mass loss by corrosion of the EEGs after cycling the potential between 0.55 and 1.4 V vs. SCE in an acid solution. This is consistent with the less than 2% mass loss estimated from the anodic corrosion charge passed. However, some evidence of EEG flakes detaching from the electrode, and this could affect the corrosion analysis. Further work is needed to investigate the cause and effect of flake detachment.

TGA studies confirmed that the reported increased thermal stability in air due to the doping of phosphorous was achieved for EEG-N-P. However, the high thermal stability of EEG-N-P did not lead to a higher resistance to electrochemical corrosion as compared to EEG-N-S. The electrochemical corrosion resistance of EEG-N-S was found to be better than EEG-N-P, based on the analysis of accelerated corrosion experiments using potential cycling and voltammetry.

The stability in air is believed to be due to phosphorous blocking the oxidation reaction by $O_2$. This inhibition effect is associated with oxygen containing P groups such as metaphosphates, C–O–PO3 groups and C–PO3 groups (Wu and Radovic, 2006). Inhibition of oxidation by phosphorus doping was not observed for electrochemical oxidation of EEG-N-P.

Surface-deposited P complexes that inhibit oxidation have been shown to be effective as site blockers (Wu and Radovic, 2006). During electrochemical corrosion these surface complexes may be attacked and no protection is obtained. The mechanism of electrochemical corrosion of EEGs and doped graphenes is not fully understood and further work is needed to determine the corrosion mechanism.

Cyclic voltammetry was used to determine the changes in capacitance of different carbons, before and after the accelerated corrosion tests. Potential steps provided

information about the charge related to corrosion, and a quantitative analysis of corrosion resistance was obtained. Doping of different elements provided the graphene with different properties, such as high thermal stability on EEG-N-P not seen in EEG-N-S. This demonstrates that graphene can be modified or tailored to different applications by doping with different heteroatoms. It has been reported (Li *et al.*, 2015) that the dual-doping of nitrogen and phosphorus in graphene- carbon nanosheets provide a good catalyst for the oxygen evolution reaction (OER) and the oxygen reduction reaction (ORR). It was also found that dual or multiple doping provided more benefits than single-element doping (Li *et al*., 2015). However, the present study suggests that the phosphorus doping may lead to lower corrosion resistance, and nitrogen- and sulfur co-doping may be preferable for OER and ORR. Further work on the properties of doped graphene with diverse heteroatoms is needed, including thermal stability, corrosion resistance, and electrochemical activity for different reactions.

Electrochemical oxidation of graphene can lead to changes on the material surface. Based on the cyclic voltammetry results, formation of oxygen functional groups occurred during potential cycling between 0.55 and 1.4 V vs. SCE. These changes will affect the wettability of the material, and the electrochemical kinetics as observed with EIS studies of the ferricyanide redox system, where the change transfer resistance increased with the number of potential cycles.

It is important to notice that the glassy carbon contributed significantly to the capacitance and corrosion charge data. Further work is needed to better understand the contribution of glassy carbon in the corrosion resistance results.

The loss of material calculated from the charge balance may be due to the oxidation of carbon to $CO_2$. SEM also showed that detachment of flakes can lead to the loss of material on the glassy carbon electrode. Raman results before and after corrosion suggest that the change of defects was more significant on EEG-N-P. The $I_D/I_G$ ratio decreased after corrosion, this may be due to the reduction of edges sites due to the loss of graphene or loss of doped heteroatoms.

**Chapter 5. Conclusions and future work**

- Higher yield was achieved with 16 $cm^2$ electrodes area compared to 4 $cm^2$ in this study. The incomplete exfoliation was suggested to be one of the reasons for higher yield, however further work is needed to investigate current distribution and current drop when a large graphite area is still in solution.

  This incomplete exfoliation of the graphite foil, observed when the electrode area was increased presents a challenge for scale-up. However, the remaining graphite area can be used for further exfoliation in a new electrolyte.
- Scale up-of graphene production requires modification of the cell and process design to achieve synthesis at industrial scale. Higher electrode area and different electrochemical cell designs should be investigated. One option may be to use multiple graphite anodes in smaller areas. The use of larger anode area and two cathodes on each side of the anode should be studied.
- The increase in temperature was recorded when larger areas were studied in a batch reactor. Evaporation of the electrolyte and changes on the quality of exfoliated graphene at with exfoliation time may affect the product quality. It may be possible to address these issues using a cooled batch reactor, or a continuous process where fresh electrolyte circulates during exfoliation.
- The types of electrodes reportedly used for electrochemical exfoliation of graphene include graphite foil (as used in this study), graphite rod, and graphite flakes. Further work on exfoliation is needed using these different graphite anodes and evaluate the yield and energy consumption. Electrochemical exfoliation has been reported (Achee *et al.*, 2018) with a cathode dimension ~10 x 10 cm, however more studies and larger areas are needed to achieve a cost effective industrial scale process.
- During exfoliation at constant current, towards the end of exfoliation the cell voltage increased due to the decrease in the electrode area, and this may affect the quality and consistency of the EEG produced. Future studies should evaluate the effect of the voltage limit used to terminate the exfoliation, or consider alternative control strategies, in order to obtain a consistent product quality.

- Doping of graphene with different heteroatoms was achieved during electrochemical exfoliation by selection of the electrolyte composition, providing the EEG with properties such as thermal stability, or enhanced activity for electrochemical reactions. Other electrolyte combinations should be explored in order to obtain graphene with enhanced performance, depending on the desired application. The properties of graphene can be altered depending on the conditions of exfoliation as well as the composition of the electrolyte.
- pH was found to have an effect on yield and energy consumption. However sample characterization of the obtained EEG was not carried out. Further work is needed to determine the graphene quality at different pH as well as the flake size obtained. pH can be easily adjusted and may be a simple way to modify graphene characteristics.
- EEG-N-P showed a higher adsorption capacity of both dyes methylene blue and methyl orange compared to EEG-N-P. The adsorption - regeneration tests of this study showed that the charge efficiency is higher for EEG-N-S compared to EEG-N-P. Significantly higher energy was required in order to regenerate the EEG-N-P adsorbent. Further work is needed to analyze the differences in regeneration. More characterization on the regenerated graphene can be done to obtain information about the anodic electrochemical regeneration mechanism and determine if the rapid regeneration is due to corrosion.
- Doped EEG was presented in this work as an adsorbent with the potential for electrochemical regeneration. A study (Krebsz *et al.*, 2021) has shown that a bio-graphene foam can achieve a high specific surface area (805 $m^2\ g^{-1}$) and can be used for a water treatment application. Therefore, one application of this EEG can be the preparation of foams to be used as adsorbent and be regenerated to be used for several cycles. Previous studies have reported the creation of nanocomposites with the objective of increasing stability and facilitating separation during adsorption processes. Graphene-$Fe_3O_4$ and GO-hydrogels are some examples (Kim *et al.*, 2018). Doped graphene can also be used for energy conversion application: electrodes drop-casted with graphene

increase the kinetics of electrochemical reactions used in batteries and fuel cells (Li *et al*., 2015)(Choi *et al.*, 2011).

- Comparison of corrosion/oxidation of doped exfoliated graphene (EEG-N-P and EEG-N-S) was presented in this study. Electrochemical techniques were used to estimate the corrosion rate of the graphene. EEG-N-S showed a higher corrosion resistance compared to EEG-N-P. This was unexpected as EEG-N-P showed a higher thermal stability in air; this suggests that the mechanism protecting EEG-N-P from oxidation in air is different from the mechanism of electrochemical corrosion. Further studies are needed understand the differences in corrosion resistance between EEG-N-P and EEG-N-S. XPS analysis can provide information to determine if surface groups were attacked during corrosion.
- SEM showed that detaching of the flakes may be one of the effects due to corrosion. However, further work is needed to understand and identify the corrosion mechanisms; characterization studies such as XPS and TEM before and after potential cycling should be carried. These characterisation techniques will provide useful information such as information on the changes in the oxygen functional groups present, the atomic composition, and roughening or other morphological changes to the exfoliated flakes.
- The corrosion products obtained from corrosion of EEG were not studied or identified in this work, further work will be needed in order to analyze this corrosion products obtained after regeneration of both EEGs.
- The capacitance increase after the corrosion tests and the carbon corrosion values were calculated neglecting the contribution of the glassy carbon. However, the contribution of this electrode is considerable. Further work is needed to determine the corrosion charge and capacitance increase of both EEGs only.

**References**

Abdelkader, A. M. A J Cooper, R A W Dryfe, and I A Kinloch (2015) 'How to get between the sheets : a review of recent works on the electrochemical exfoliation of graphene materials from bulk graphite'. Royal Society of Chemistry, pp. 6944–6956. doi: 10.1039/c4nr06942k.

Achee, Thomas C., Wanmei Sun, Joshua T. Hope, Samuel G. Quitzau, Charles Brandon Sweeney, Smit A. Shah, (2018) 'High-yield scalable graphene nanosheet production from compressed graphite using electrochemical exfoliation', *Scientific Reports*. Springer US, 8(1), pp. 1–8. doi: 10.1038/s41598-018-32741-3.

Acuña-bedoya, J., Comas-cabrales, J. A. and Alvarez-pugliese, C. E. (2020) 'Evaluation of electrolytic reactor configuration for the regeneration of granular activated carbon saturated with methylene blue', *Journal of Environmental Chemical Engineering*, 8(May).

Ali, I., Asim, M. and Khan, T. A. (2012) 'Low cost adsorbents for the removal of organic pollutants from wastewater', 113, pp. 170–183.

Ali, M. E. A. (2019) 'Preparation of graphene nanosheets by electrochemical exfoliation of a graphite-nanoclay composite electrode : Application for the adsorption of organic dyes', *Colloids and Surfaces A*. Elsevier, 570(January), pp. 107–116. doi: 10.1016/j.colsurfa.2019.02.063.

Allen, M. J., Tung, V. C. and Kaner, R. B. (2010) 'Honeycomb Carbon : A Review of Graphene', pp. 132–145.

Ambrosi, A., Chun K. C., Bonanni, A. and Pumera M. (2014) 'itrogen-doped carbon nanotubes and graphene composite structures for energy and catalytic applications'.

Amft, M., Lebègue, S., Eriksson, O., and Skorodumova, N.V. (2011) 'Adsorption of Cu, Ag, and Au atoms on graphene including van der Waals interactions', *Journal of Physics Condensed Matter*, 23(39). doi: 10.1088/0953-8984/23/39/395001.

Apul, O. G. Wang, Q., Zhou, Y., and Karanfil, T. (2013) 'Adsorption of aromatic organic contaminants by graphene nanosheets: Comparison with carbon nanotubes and

activated carbon', *Water Research*. Elsevier Ltd, 47(4), pp. 1648–1654. doi: 10.1016/j.watres.2012.12.031.

Bakunin, E. S., Obraztsova, E. Y. and Rukhov, A. V. (2019) 'Modern Methods for Synthesis of Few-Layer Graphene Structures by Electrochemical Exfoliation of Graphite', *Inorganic Materials: Applied Research*, 10(2), pp. 249–255. doi: 10.1134/S2075113319020047.

Bauer, M., Beratz,S., Ruhland, K., Horn,S., and Moosburger-will, J. (2020) 'Applied Surface Science Anodic oxidation of carbon fi bers in alkaline and acidic electrolyte : Quanti fi cation of surface functional groups by gas-phase derivatization', 506(November 2019). doi: 10.1016/j.apsusc.2019.144947.

Beless, B., Rifai, H. S. and Rodrigues, D. F. (2014) 'Efficacy of carbonaceous materials for sorbing polychlorinated biphenyls from aqueous solution', *Environmental Science and Technology*, 48(17), pp. 10372–10379. doi: 10.1021/es502647n.

Borup, R., Meyers, J., Pivovar, B. Seung Kim, Y., Mukundan, R. (2007) 'Scientific Aspects of Polymer Electrolyte Fuel Cell Durability and Degradation', pp. 3904–3951. doi: 10.1021/cr050182l.

Brown, N.W., Roberts, E.P.L., Garforth, A.A. and Dryfe, R.A.W. (2002) 'Treatment of dyehouse effluents with a carbon-based adsorbent using anodic oxidation regeneration', (1999), pp. 219–225.

Castanheira, L., Dubau, L., Mermoux, M., Berthomé, G., Caqué, N., Rossinot, E., Chatenet, M. and Maillard, F., (2014) 'Carbon Corrosion in Proton-Exchange Membrane Fuel Cells: From Model Experiments to Real-Life Operation in Membrane Electrode Assemblies'. doi: 10.1021/cs500449q.

Castanheira, L., Silva, W.O., Lima, F.H., Crisci, A., Dubau, L. and Maillard, F., (2015) 'Carbon corrosion in proton-exchange membrane fuel cells: Effect of the carbon structure, the degradation protocol, and the gas atmosphere', *ACS Catalysis*, 5(4), pp. 2184–2194. doi: 10.1021/cs501973j.

Chang, B.Y.S., Huang, N.M., An'amt, M.N., Marlinda, A.R., Norazriena, Y., Muhamad,

M.R., Harrison, I., Lim, H.N. and Chia, C.H., (2012) 'Facile hydrothermal preparation of titanium dioxide decorated reduced graphene oxide nanocomposite', *International Journal of Nanomedicine*, 7(June 2014), pp. 3379–3387. doi: 10.2147/IJN.S28189.

Chen, P., Fryling, M. A. and Mccreery, R. L. (1995) 'Electron Transfer Kinetics at Modified Carbon Electrode Surfaces : The Role of Specific Surface', 67, pp. 3115–3122. doi: 10.1021/ac00114a004.

Chen, P. and Mccreery, R. L. (1996) 'Control of Electron Transfer Kinetics at Glassy Carbon Electrodes by Specific Surface Modification', 68(22), pp. 3958–3965. doi: 10.1021/ac960492r.

Choi, C. H., Park, S. H. and Woo, S. I. (2011) 'Heteroatom doped carbons prepared by the pyrolysis of bio-derived amino acids as highly active catalysts for oxygen electro-reduction reactions †', pp. 406–412. doi: 10.1039/c0gc00384k.

Choi, C. H., Park, S. H. and Woo, S. I. (2012) 'Binary and ternary doping of nitrogen, boron, and phosphorus into carbon for enhancing electrochemical oxygen reduction activity', *ACS Nano*, 6(8), pp. 7084–7091. doi: 10.1021/nn3021234.

Chowdhury, S. and Balasubramanian, R. (2014) 'Recent advances in the use of graphene-family nanoadsorbents for removal of toxic pollutants from wastewater', *Advances in Colloid and Interface Science*. Elsevier B.V., 204, pp. 35–56. doi: 10.1016/j.cis.2013.12.005.

Conway, B. E., Birss, V. and Wojtowicz, J. (1997) 'The role and utilization of pseudocapacitance for energy storage by supercapacitors', *Journal of Power Sources*, 66(1–2), pp. 1–14. doi: 10.1016/S0378-7753(96)02474-3.

Crini, G. (2006) 'Non-conventional low-cost adsorbents for dye removal : A review', 97, pp. 1061–1085. doi: 10.1016/j.biortech.2005.05.001.

Crini, G. and Lichtfouse, E. (2020) 'Advantages and disadvantages of techniques used for wastewater treatment', *Environmental Chemistry Letters*. Springer International Publishing, 17(1), pp. 145–155. doi: 10.1007/s10311-018-0785-9.

Dresselhaus, M. S., Jorio, A. and Saito, R. (2010) 'Characterizing Graphene, Graphite,

and Carbon Nanotubes by Raman Spectroscopy', *Annual Review of Condensed Matter Physics*, 1(1), pp. 89–108. doi: 10.1146/annurev-conmatphys-070909-103919.

Eckmann, A., Felten, A., Verzhbitskiy, I., Davey, R. and Casiraghi, C., (2013) 'Raman study on defective graphene: Effect of the excitation energy, type, and amount of defects', *Physical Review B - Condensed Matter and Materials Physics*, 88(3), pp. 1–11. doi: 10.1103/PhysRevB.88.035426.

El-Khaiary, M. I. (2008) 'Least-squares regression of adsorption equilibrium data: Comparing the options', *Journal of Hazardous Materials*, 158(1), pp. 73–87. doi: 10.1016/j.jhazmat.2008.01.052.

Ersan, G., Kaya, Y., Apul, O.G. and Karanfil, T.(2015) 'Adsorption of organic contaminants by graphene nanosheets, carbon nanotubes and granular activated carbons under natural organic matter preloading conditions', *Science of the Total Environment*, 565, pp. 811–817. doi: 10.1016/j.scitotenv.2016.03.224.

Ersan, G., Apul, O.G., Perreault, F. and Karanfil, T. (2017) 'Adsorption of organic contaminants by graphene nanosheets: A review', *Water Research*, 126, pp. 385–398. doi: 10.1016/j.watres.2017.08.010.

Fan, X., Zhou, H. and Guo, X. (2011) 'Asymmetric supercapacitors based on graphene/MnO2 and activated carbon nanofiber electrodes with high power and energy density', *Advanced Functional Materials*, 21(12), pp. 2366–2375. doi: 10.1002/adfm.201100058.

Ferrari, A. C. and Basko, D. M. (2013) 'Raman spectroscopy as a versatile tool for studying the properties of graphene', *Nature Nanotechnology*. Nature Publishing Group, 8(4), pp. 235–246. doi: 10.1038/nnano.2013.46.

Forouzandeh, F., Li, X., Banham, D.W., Feng, F., Ye, S. and Birss, V., (2015) 'Evaluation of the Corrosion Resistance of Carbons for Use as PEM Fuel Cell Cathode Supports', 162(12). doi: 10.1149/2.0381512jes.

Forouzandeh, F., Li, X., Banham, D. W., Feng, F., Joseph Kakanat, A., *et al.* (2018) 'Improving the corrosion resistance of proton exchange membrane fuel cell carbon

supports by pentafluorophenyl surface functionalization', *Journal of Power Sources*. Elsevier, 378(November 2017), pp. 732–741. doi: 10.1016/j.jpowsour.2017.12.008.

Forouzandeh, F., Li, X., Banham, D.W., Feng, F., Ye, S. and Birss, V. (2018) 'Understanding the Corrosion Resistance of Meso- and Micro-Porous Carbons for Application in PEM Fuel Cells', *Journal of The Electrochemical Society*, 165(6), pp. F3230–F3240. doi: 10.1149/2.0261806jes.

Fu, F. and Wang, Q. (2011) 'Removal of heavy metal ions from wastewaters : A review', 92. doi: 10.1016/j.jenvman.2010.11.011.

Guan, H., Fan, L.Z., Zhang, H. and Qu, X. (2010) 'Electrochimica Acta Polyaniline nanofibers obtained by interfacial polymerization for high-rate supercapacitors', 56, pp. 964–968. doi: 10.1016/j.electacta.2010.09.078.

Hack, R., Correia, C.H.G., Zanon, R.A.D.S. and Pezzin, S.H. (2018) 'Characterization of graphene nanosheets obtained by a modified hummer's method', *Revista Materia*, 23(1). doi: 10.1590/s1517-707620170001.0324.

Htwe, Y.Z.N., Chow, W.S., Suda, Y., Thant, A.A. and Mariatti, M. (2019) 'Effect of electrolytes and sonication times on the formation of graphene using an electrochemical exfoliation process', *Applied Surface Science*. Elsevier, 469(September 2018), pp. 951–961. doi: 10.1016/j.apsusc.2018.11.029.

Jagtap, S., Yenkie, M.K., Labhsetwar, N. and Rayalu, S. (2012) 'Fluoride in Drinking Water and Defluoridation of Water', pp. 2454–2466.

Kangasniemi, K. H., Condit, D. A. and Jarvi, T. D. (2004) 'Characterization of Vulcan Electrochemically Oxidized under Simulated PEM Fuel Cell Conditions'. doi: 10.1149/1.1649756.

Kaniyoor, A. and Ramaprabhu, S. (2012) 'A Raman spectroscopic investigation of graphite oxide derived graphene', *AIP Advances*, 2(3). doi: 10.1063/1.4756995.

Khan, A.H., Ghosh, S., Pradhan, B., Dalui, A., Shrestha, L.K., Acharya, S. and Ariga, K (2017) 'Two-dimensional (2D) nanomaterials towards electrochemical nanoarchitectonics in energy-related applications', *Bulletin of the Chemical Society of*

*Japan*, 90(6), pp. 627–648. doi: 10.1246/bcsj.20170043.

Kim, S., Park, C.M., Jang, M., Son, A., Her, N., Yu, M., Snyder, S., Kim, D.H. and Yoon, Y (2018) 'Aqueous removal of inorganic and organic contaminants by graphene-based nanoadsorbents: A review', *Chemosphere*. Elsevier Ltd, 212, pp. 1104–1124. doi: 10.1016/j.chemosphere.2018.09.033.

Kinoshita, K., and J. A. S. B. (1973) 'Potentiodynamic analysis of surface oxides on carbon blacks', *Carbon*, 11, pp. 403–411.

Krebsz, M., Pasinszki, T., Tung, T.T., Nine, M.J. and Losic, D. (2021) 'Chemosphere Multiple applications of bio-graphene foam for ef fi cient chromate ion removal and oil-water separation', *Chemosphere*. Elsevier Ltd, 263, p. 127790. doi: 10.1016/j.chemosphere.2020.127790.

Kusmierek, E. (2019) 'Electrochemical and Corrosion Characterization of TiO 2 -RuO 2 / Ti Electrodes Modified with WO 3', pp. 499–515.

Kyzas, G.Z., Deliyanni, E.A., Bikiaris, D.N. and Mitropoulos, A. C. (2017) 'Chemical Engineering Research and Design Graphene composites as dye adsorbents : Review'. Institution of Chemical Engineers, 9, pp. 75–88.

Lee, W.J., Maiti, U.N., Lee, J.M., Lim, J., Han, T. H. and K. (2014) 'Nitrogen-doped carbon nanotubes and graphene composite structures for energy and catalytic applications', *Chemical Communications*, 50, pp. 6818–6830. doi: 10.1039/c4cc00146j.

Li, R., Wei, Z. and Gou, X. (2015) 'Nitrogen and Phosphorus Dual-Doped Graphene/Carbon Nanosheets as Bifunctional Electrocatalysts for Oxygen Reduction and Evolution', *ACS Catalysis*, 5(7), pp. 4133–4142. doi: 10.1021/acscatal.5b00601.

Li, Y., Du, Q., Liu, T., Peng, X., Wang, J., Sun, J., Wang, Y., Wu, S., Wang, Z., Xia, Y. and Xia, L (2013) 'Comparative study of methylene blue dye adsorption onto activated carbon, graphene oxide, and carbon nanotubes', *Chemical Engineering Research and Design*. Institution of Chemical Engineers, 91(2), pp. 361–368. doi: 10.1016/j.cherd.2012.07.007.

Liu, T., Li, Y., Du, Q., Sun, J., Jiao, Y., Yang, G., Wang, Z., Xia, Y., Zhang, W., Wang, K. and

Zhu, H. (2012) ‘Adsorption of methylene blue from aqueous solution by graphene’, *Colloids and Surfaces B: Biointerfaces*. Elsevier B.V., 90(1), pp. 197–203. doi: 10.1016/j.colsurfb.2011.10.019.

Long, D., Li, W., Ling, L., Miyawaki, J., Mochida, I. and Yoon, S.H., 2010. Preparation of nitrogen-doped graphene sheets by a combined chemical and hydrothermal reduction of graphene oxide. *Langmuir*, *26*(20), pp.16096-16102.

Lou, F., Buan, M.E.M., Muthuswamy, N., Walmsley, J.C., Rønning, M. and Chen, D. (2016) ‘One-step electrochemical synthesis of tunable nitrogen-doped graphene.’, *Journal of Materials Chemistry A*. Royal Society of Chemistry, 4, pp. 1233–1243. doi: 10.1039/c5ta08038j.

Lounasvuori, M.M., Rosillo-Lopez, M., Salzmann, C.G., Caruana, D.J. and Holt, K.B. (2014) ‘Electrochemical characterisation of graphene nano fl akes with functionalised edges’. Royal Society of Chemistry, (Cv), pp. 293–310. doi: 10.1039/c4fd00034j.

Meyer, J.C., Geim, A.K., Katsnelson, M.I., Novoselov, K.S., Obergfell, D., Roth, S., Girit, C. and Zettl, A. (2007) ‘On the roughness of single- and bi-layer graphene membranes’, 143, pp. 101–109. doi: 10.1016/j.ssc.2007.02.047.

Momodu, D., Madito, M.J., Singh, A., Sharif, F., Karan, K., Trifkovic, M., Bryant, S. and Roberts, E.P. (2021) ‘Mixed-acid intercalation for synthesis of a high conductivity electrochemically exfoliated graphene’, *Carbon*. Elsevier Ltd, 171, pp. 130–141. doi: 10.1016/j.carbon.2020.08.066.

Momodu, D.Y., Barzegar, F., Bello, A., Dangbegnon, J., Masikhwa, T., Madito, J. and Manyala, N. (2015) ‘Simonkolleite-graphene foam composites and their superior electrochemical performance’, *Electrochimica Acta*. Elsevier Ltd, 151, pp. 591–598. doi: 10.1016/j.electacta.2014.11.015.

De Moura, D.C., Quiroz, M.A., Da Silva, D.R., Salazar, R. and Martínez-Huitle, C. A. (2016) ‘Electrochemical degradation of Acid Blue 113 dye using TiO 2 -nanotubes decorated with PbO 2 as anode’, *Environmental Nanotechnology, Monitoring & Management*. Environmental Nanotechnology, Monitoring & Management, 5, pp. 13–20. doi: 10.1016/j.enmm.2015.11.001.

Nagyte, V., Kelly, D.J., Felten, A., Picardi, G., Shin, Y., Alieva, A., Worsley, R.E., Parvez, K., Dehm, S., Krupke, R. and Haigh, S.J. (2020) 'Raman Fingerprints of Graphene Produced by Anodic Electrochemical Exfoliation'. doi: 10.1021/acs.nanolett.0c00332.

Najafpoor, A. A., Davoudi, M. and Salmani, E. R. (2017) 'Decolorization of synthetic textile wastewater using electrochemical cell divided by cellulosic separator'. Journal of Environmental Health Science and Engineering, pp. 1–11. doi: 10.1186/s40201-017-0273-3.

Nicholson, R. S. (1965) 'Theory and Application of Cyclic Voltammetry for Measurement of Electrode Reaction Kinetics', 37(11), pp. 1351–1355. doi: 10.1021/ac60230a016.

Novoselov, K.S., Geim, A.K., Morozov, S.V., Jiang, D., Katsnelson, M.I., Grigorieva, I., Dubonos, S (2005) 'Two-dimensional gas of massless Dirac fermions in graphene', 438(November), pp. 197–200. doi: 10.1038/nature04233.

Oh, S.G. Rodriguez, N. M. (1993) 'In situ electron microscopy studies of the inhibition of graphite oxidation by phosphorus', *Journal of materials research*, pp. 2879–2888.

Panizza, M., Barbucci, A., Ricotti, R. and Cerisola, G. (2007) 'Electrochemical degradation of methylene blue', 54(October 2006), pp. 382–387. doi: 10.1016/j.seppur.2006.10.010.

Paredes, J. I. and Munuera, J. M. (2017) 'Recent advances and energy-related applications of high quality / chemically doped graphenes obtained by electrochemical exfoliation methods', pp. 7228–7242. doi: 10.1039/c7ta01711a.

Parvez, K., Rincón, R.A., Weber, N.E., Cha, K.C. and Venkataraman, S. S. (2016) 'One-step electrochemical synthesis of nitrogen and sulfur co-doped, high-quality graphene oxide', *Chemical Communications*, pp. 5714–5717. doi: 10.1039/c6cc01250g.

Parvez, K., Wu, Z.S., Li, R., Liu, X., Graf, R., Feng, X. and Mullen, K. (2014) 'Exfoliation of graphite into graphene in aqueous solutions of inorganic salts', *Journal of the American Chemical Society*, 136(16), pp. 6083–6091. doi: 10.1021/ja5017156.

Pérez-Rodríguez, S., Sebastián, D. and Lázaro, M. J. (2019) 'Electrochemical oxidation

of ordered mesoporous carbons and the influence of graphitization', *Electrochimica Acta*, 303, pp. 167–175. doi: 10.1016/j.electacta.2019.02.065.

Pinto, H., Jones, R., Goss, J.P. and Briddon, P.R., 2010. Mechanisms of doping graphene. *physica status solidi (a)*, *207*(9), pp.2131-2136.

Qiao, M.X., Zhang, Y., Zhai, L.F. and Sun, M (2018) 'Corrosion of graphite electrode in electrochemical advanced oxidation processes: Degradation protocol and environmental implication', *Chemical Engineering Journal*. Elsevier, 344(January), pp. 410–418. doi: 10.1016/j.cej.2018.03.105.

Ramesha, G.K., Kumara, A.V., Muralidhara, H.B. and Sampath, S. (2011) 'Graphene and graphene oxide as effective adsorbents toward anionic and cationic dyes', *Journal of Colloid and Interface Science*. Elsevier Inc., 361(1), pp. 270–277. doi: 10.1016/j.jcis.2011.05.050.

Randles, J. E. B. (1947) 'Kinetics of rapid electrode reactions', *Discussions of the faraday society*, 1, pp. 11–19.

Ren, P.G., Yan, D.X., Ji, X., Chen, T. and Li, Z.M. (2011) 'Temperature dependence of grapheme oxide reduced by hydrazine hydrate', *Nanotechnology*, 22(5). doi: 10.1088/0957-4484/22/5/055705.

Robinson, T., McMullan, G., Marchant, R. and Nigam, P. (2001) 'Remediation of dyes in textile e , uent : a critical review on current treatment technologies with a proposed alternative', 77, pp. 247–255.

Roscher, S., Hoffmann, R. and Ambacher, O. (2019) 'Determination of the graphene-graphite ratio of graphene powder by Raman 2D band symmetry analysis', *Analytical Methods*, 11(9), pp. 1180–1191. doi: 10.1039/c8ay02619j.

Shao, Y., Yin, G., Zhang, J. and Gao, Y (2006) 'Comparative investigation of the resistance to electrochemical oxidation of carbon black and carbon nanotubes in aqueous sulfuric acid solution', *Electrochimica Acta*, 51, pp. 5853–5857. doi: 10.1016/j.electacta.2006.03.021.

Shao, Y., Wang, J., Kou, R., Engelhard, M., Liu, J., Wang, Y. and Lin, Y. (2009b) 'The

corrosion of PEM fuel cell catalyst supports and its implications for developing durable catalysts', *Electrochimica Acta*, 54(11), pp. 3109–3114. doi: 10.1016/j.electacta.2008.12.001.

Sharif, F., Gagnon, L.R., Mulmi, S. and Roberts, E.P. (2017) 'Electrochemical regeneration of a reduced graphene oxide/magnetite composite adsorbent loaded with methylene blue', *Water Research*. Elsevier Ltd, 114, pp. 237–245. doi: 10.1016/j.watres.2017.02.042.

Sharif, F., Zeraati, A.S., Ganjeh-Anzabi, P., Yasri, N., Perez-Page, M., Holmes, S.M., Sundararaj, U., Trifkovic, M. and Roberts, E.P. (2020) 'Synthesis of a high-temperature stable electrochemically exfoliated graphene', *Carbon*. Elsevier Ltd, 157(3), pp. 681–692. doi: 10.1016/j.carbon.2019.10.042.

Sharif, F. and Roberts, Edward P.L. (2020) 'Anodic electrochemical regeneration of a graphene/titanium dioxide composite adsorbent loaded with an organic dye', *Chemosphere*. Elsevier Ltd, 241, p. 125020. doi: 10.1016/j.chemosphere.2019.125020.

Sharif, F. and Roberts, Edward P L (2020) 'Chemosphere Anodic electrochemical regeneration of a graphene / titanium dioxide composite adsorbent loaded with an organic dye', *Chemosphere*. Elsevier Ltd, 241, p. 125020. doi: 10.1016/j.chemosphere.2019.125020.

Shen, Q., Zhu, J., Cheng, L., Zhang, J., Zhang, Z. and Xu, X. (2011) 'Enhanced algae removal by drinking water treatment of chlorination coupled with coagulation', *DES*. Elsevier B.V., 271(1–3), pp. 236–240. doi: 10.1016/j.desal.2010.12.039.

Shen, Y., Fang, Q. and Chen, B. (2015) 'Environmental Applications of Three-Dimensional Graphene-Based Macrostructures : Adsorption , Transformation , and Detection', pp. 67–84. doi: 10.1021/es504421y.

Singh, A.K., Yasri, N., Karan, K. and Roberts, E.P. (2019) 'Electrocatalytic Activity of Functionalized Carbon Paper Electrodes and Their Correlation to the Fermi Level Derived from Raman Spectra', *ACS Applied Energy Materials*. American Chemical Society, 2(3), pp. 2324–2336. doi: 10.1021/acsaem.9b00180.

Sluyters-Rehbach, M. (1994) 'Impedances of electrochemical systems: Terminology, nomenclature and representation-Part I: Cells with metal electrodes and liquid solutions', *Pure and applied chemistry*, 66(9), pp. 1831–1891.

Tamgadge, R. M. and Shukla, A. (2019) 'A pH-dependent partial electrochemical exfoliation of highly oriented pyrolytic graphite for high areal capacitance electric double layer capacitor electrode', *Electrochimica Acta*, 325, pp. 1–11. doi: 10.1016/j.electacta.2019.134933.

Tijani, J.O., Fatoba, O.O., Madzivire, G. and Petrik, L.F. (2014) 'A Review of Combined Advanced Oxidation Technologies for the Removal of Organic Pollutants from Water'. doi: 10.1007/s11270-014-2102-y.

Velizarov, S. (2005) 'Removal of inorganic anions from drinking water supplies by membrane bio / processes', (2004), pp. 361–380. doi: 10.1007/s11157-004-4627-9.

Wang, B., Liu, Q., Qian, Z., Zhang, X., Wang, J., Li, Z., Yan, H., Gao, Z., Zhao, F. and Liu, L (2014) 'Two steps in situ structure fabrication of Ni-Al layered double hydroxide on Ni foam and its electrochemical performance for supercapacitors', *Journal of Power Sources*. Elsevier B.V, 246, pp. 747–753. doi: 10.1016/j.jpowsour.2013.08.035.

Wang, C., Feng, C., Gao, Y., Ma, X., Wu, Q. and Wang, Z. (2011) 'Preparation of a graphene-based magnetic nanocomposite for the removal of an organic dye from aqueous solution', *Chemical Engineering Journal*. Elsevier B.V., 173(1), pp. 92–97. doi: 10.1016/j.cej.2011.07.041.

Wang, G., Jia, L.T., Zhu, Y., Hou, B., Li, D.B. and Sun, Y.H., 2012. Novel preparation of nitrogen-doped graphene in various forms with aqueous ammonia under mild conditions. *Rsc Advances*, *2*(30), pp.11249-11252.

Wang, J., Manga, K.K., Bao, Q. and Loh, K.P. (2011) 'High-Yield Synthesis of Few-Layer Graphene Flakes through Electrolyte', pp. 8888–8891. doi: 10.1021/ja203725d.

Wang, X., Li, W., Chen, Z., Waje, M. and Yan, Y. (2006) 'Durability investigation of carbon nanotube as catalyst support for proton exchange membrane fuel cell', 158, pp. 154–159. doi: 10.1016/j.jpowsour.2005.09.039.

Wu, X. and Radovic, L. R. (2006) 'Inhibition of catalytic oxidation of carbon / carbon composites by phosphorus', 44, pp. 141–151. doi: 10.1016/j.carbon.2005.06.038.

Xue, Z., Zhao, S., Zhao, Z., Li, P. and Gao, J. (2016) 'Thermodynamics of dye adsorption on electrochemically exfoliated graphene', *Journal of Materials Science*. Springer US, 51(10), pp. 4928–4941. doi: 10.1007/s10853-016-9798-6.

Yan, H., Tao, X., Yang, Z., Li, K., Yang, H., Li, A. and Cheng, R. (2014) 'Effects of the oxidation degree of graphene oxide on the adsorption of methylene blue', *Journal of Hazardous Materials*. Elsevier B.V., 268, pp. 191–198. doi: 10.1016/j.jhazmat.2014.01.015.

Yang, J., Park, S., Choi, K.Y., Park, H.S., Cho, Y.G., Ko, H. and Song, H.K. (2018) 'Activity-Durability Coincidence of Oxygen Evolution Reaction in the Presence of Carbon Corrosion: Case Study of MnCo2O4 Spinel with Carbon Black', *ACS Sustainable Chemistry and Engineering*, 6(8), pp. 9566–9571. doi: 10.1021/acssuschemeng.8b01879.

Yang, S., Brüller, S., Wu, Z.S., Liu, Z., Parvez, K., Dong, R., Richard, F., Samorì, P., Feng, X. and Müllen, K. (2015) 'Organic Radical-Assisted Electrochemical Exfoliation for the Scalable Production of High-Quality Graphene', *Journal of the American Chemical Society*, 137(43), pp. 13927–13932. doi: 10.1021/jacs.5b09000.

Yang, S., Lohe, M.R., Müllen, K. and Feng, X. (2016) 'New-Generation Graphene from Electrochemical Approaches : Production and Applications', pp. 6213–6221. doi: 10.1002/adma.201505326.

Yang, S.T., Chen, S., Chang, Y., Cao, A., Liu, Y. and Wang, H. (2011) 'Removal of methylene blue from aqueous solution by graphene oxide', *Journal of Colloid and Interface Science*. Elsevier Inc., 359(1), pp. 24–29. doi: 10.1016/j.jcis.2011.02.064.

Yang, Y., Lu, F., Zhou, Z., Song, W., Chen, Q. and Ji, X. (2013) 'Electrochimica Acta Electrochemically cathodic exfoliation of graphene sheets in room temperature ionic liquids N-butyl , methylpyrrolidinium bis ( trifluoromethylsulfonyl ) imide and their electrochemical properties', 113, pp. 9–16.

Yang, Y., Hou, H., Zou, G., Shi, W., Shuai, H., Li, J. and Ji, X. (2019) 'Electrochemical exfoliation of graphene-like two-dimensional nanomaterials', *Nanoscale*. Royal Society of Chemistry, 11(1), pp. 16–33. doi: 10.1039/c8nr08227h.

Yi, Y., Tornow, J., Willinger, E., Willinger, M.G., Ranjan, C. and Schlögl, R. (2015) 'Electrochemical Degradation of Multiwall Carbon Nanotubes at High Anodic Potential for Oxygen Evolution in Acidic Media', pp. 1929–1937. doi: 10.1002/celc.201500268.

Yi, Y., Weinberg, G., Prenzel, M., Greiner, M., Heumann, S., Becker, S. and Schlögl, R (2017) 'Electrochemical corrosion of a glassy carbon electrode', *Catalysis Today*. Elsevier, 295(July), pp. 32–40. doi: 10.1016/j.cattod.2017.07.013.

Yu, P., Lowe, S.E., Simon, G.P. and Zhong, Y.L. (2015) 'Electrochemical exfoliation of graphite and production of functional graphene', *Current Opinion in Colloid and Interface Science*. Elsevier B.V., 20(5–6), pp. 329–338. doi: 10.1016/j.cocis.2015.10.007.

Zafar, Z. and Ni, Z. H. (2013) 'Evolution of Raman spectra in nitrogen doped graphene', *Carbon*. Elsevier Ltd, 61, pp. 57–62. doi: 10.1016/j.carbon.2013.04.065.

Zeng, F., Sun, Z., Sang, X., Diamond, D., Lau, K.T., Liu, X. and Su, D.S. (2011) 'In Situ One-Step Electrochemical Preparation of Graphene Oxide Nanosheet-Modified Electrodes for Biosensors', pp. 1587–1591. doi: 10.1002/cssc.201100319.

Zhang, Y. I., Zhang, L. and Zhou, C. (2013) 'Graphene and Related Applications', pp. 2329–2339. doi: 10.1021/ar300203n.

Zhong, Y.L., Tian, Z., Simon, G.P. and Li, D. (2015) 'Scalable production of graphene via wet chemistry: Progress and challenges', *Materials Today*. Elsevier Ltd., 18(2), pp. 73–78. doi: 10.1016/j.mattod.2014.08.019.

Zhou, M. H. and Lei, L. C. (2006) 'Electrochemical regeneration of activated carbon loaded with p -nitrophenol in a fluidized electrochemical reactor', 51, pp. 4489–4496. doi: 10.1016/j.electacta.2005.12.028.

Zhou, M. and Lei, L. (2006) 'The role of activated carbon on the removal of p -nitrophenol in an integrated three-phase electrochemical reactor', 65, pp. 1197–1203.

doi: 10.1016/j.chemosphere.2006.03.054.

Zhu, Y., Murali, S., Cai, W., Li, X., Suk, J.W., Potts, J.R. and Ruoff, R.S (2010) 'Graphene and Graphene Oxide : Synthesis , Properties , and Applications', pp. 3906–3924. doi: 10.1002/adma.201001068.

## Supporting information

Appendix 1: yield and energy consumption of exfoliation at small scale at 200 mA $cm^{-2}$ and different initial pH using 0.1 M $(NH_4)_2SO_4$

| Electrolyte (0.1 M) | Applied current density | pH | Batch Exfoliation time | Average cell voltage | Current | Graphene obtained (calculated) | Yield | Energy |
|---|---|---|---|---|---|---|---|---|
| **Units** | **mA $cm^{-2}$** | | **hr** | **V** | **A** | **g** | **%** | **kWh $kg^{-1}$** |
| $(NH_4)_2SO_4$ | 200 | 4.04 | 1.55 | 9.05 | 0.8 | 0.1351 ± 0.003 | 53 ± 1.6 | 83 ± 2.60 |
| $(NH_4)_2SO_4$ | 200 | 7.03 | 1.46 | 8.86 | 0.8 | 0.1177 ± 0.012 | 49 ± 3.1 | 88 ± 12.81 |
| $(NH_4)_2SO_4$ | 200 | 9.95 | 1.48 | 8.56 | 0.8 | 0.1531 ± 0.009 | 64 ± 6.8 | 66 ± 5.52 |

Appendix 2: yield and energy consumption of exfoliation at 16 $cm^2$ electrodes area

| Electrolyte (0.1 M) | Applied current density | Applied cell voltage | Batch Exfoliation time | Average cell voltage | Current | Graphene obtained (calculated) | Yield | Energy |
|---|---|---|---|---|---|---|---|---|
| **Units** | **mA $cm^{-2}$** | **V** | **hr** | **V** | **A** | **g** | **%** | **kWh $kg^{-1}$** |
| $(NH_4)_2SO_4$ | 200 | - | 1.35 | 10.10 | 3.2 | 0.4762 ± 0.030 | 57 ± 0.76 | 92 ± 8.30 |
| $(NH_4)_2SO_4$ | - | 10 | 1.46 | - | 3.176 | 0.5175 ± 0.070 | 59 ± 7.42 | 90 ± 17.46 |
| $(NH_4)_2HPO_4$ | 200 | - | 1.09 | 12.62 | 3.2 | 0.4982 ± 0.044 | 58 ± 6.26 | 88 ± 11.12 |
| $(NH_4)_2HPO_4$ | - | 10 | 1.7 | - | 1.952 | 0.5623 ± 0.015 | 62 ± 1.78 | 59 ± 2.22 |

Appendix 3: yield and energy consumption of exfoliation at 4 $cm^2$ electrodes area

| Electrolyte (0.1 M) | Applied current density | Applied cell voltage | Batch Exfoliation time | Average cell voltage | Current | Graphene obtained (calculated) | Yield | Energy |
|---|---|---|---|---|---|---|---|---|
| **Units** | **mA $cm^{-2}$** | **V** | **hr** | **V** | **A** | **g** | **%** | **kWh $kg^{-1}$** |
| $(NH_4)_2SO_4$ | 200 | - | 1.327 | 8.59 | 0.8 | 0.0973 ± 0.0105 | 41 ± 3.5 | 94 ± 14 |
| $(NH_4)_2SO_4$ | - | 10 | 1.011 | - | 1.02 | 0.0923 ± 0.0118 | 39 ± 3.6 | 112 ± 20 |
| $(NH_4)_2HPO_4$ | 200 | - | 0.899 | 10.72 | 0.8 | 0.1048 ± 0.0197 | 44 ± 5.8 | 74 ± 20 |
| $(NH_4)_2HPO_4$ | - | 10 | 0.972 | - | 0.67 | 0.1054 ± 0.0125 | 45 ± 1.7 | 62 ± 10 |

Appendix 4: Yield and energy consumption of graphene produced at large scale with different current densities

| Electrolyte (0.1 M) | Current density | Average cell voltaje | Batch Exfoliation time | Current | Graphene obtained | Yield | Energy |
|---|---|---|---|---|---|---|---|
| | **mA $cm^{-2}$** | **V** | **hr** | **A** | **g** | **%** | **kWh/kg** |
| $(NH_4)_2SO_4$ | 100 | 7.39 | 3.05 | 1.6 | 0.4702 ±0.0274 | 58 ± 2.17 | 77 ± 6.34 |
| $(NH_4)_2SO_4$ | 200 | 10.10 | 1.35 | 3.2 | 0.4762 ±0.0304 | 57 ± 0.76 | 92 ± 8.30 |
| $(NH_4)_2SO_4$ | 300 | 12.25 | 0.95 | 4.8 | 0.4419 ±0.0295 | 52 ± 2.49 | 126 ± 11.98 |
| $(NH_4)_2HPO_4$ | 100 | 9.22 | 2.20 | 1.6 | 0.5655 ± 0.0791 | 65 ± 6.60 | 57 ± 11.58 |
| $(NH_4)_2HPO_4$ | 200 | 12.62 | 1.09 | 3.2 | 0.4982 ± 0.044 | 58 ± 6.26 | 88 ± 11.12 |
| $(NH_4)_2HPO_4$ | 300 | 16.44 | 0.76 | 4.8 | 0.5082 ± 0.0307 | 59 ± 2.98 | 118 ± 10.12 |

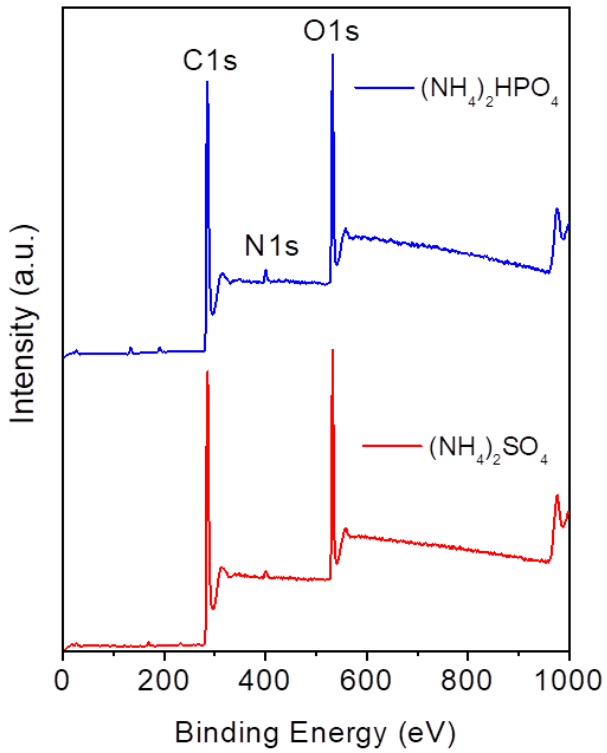


Appendix 5: XPS survey of EEG-N-P (blue) and EEG-N-S (red).

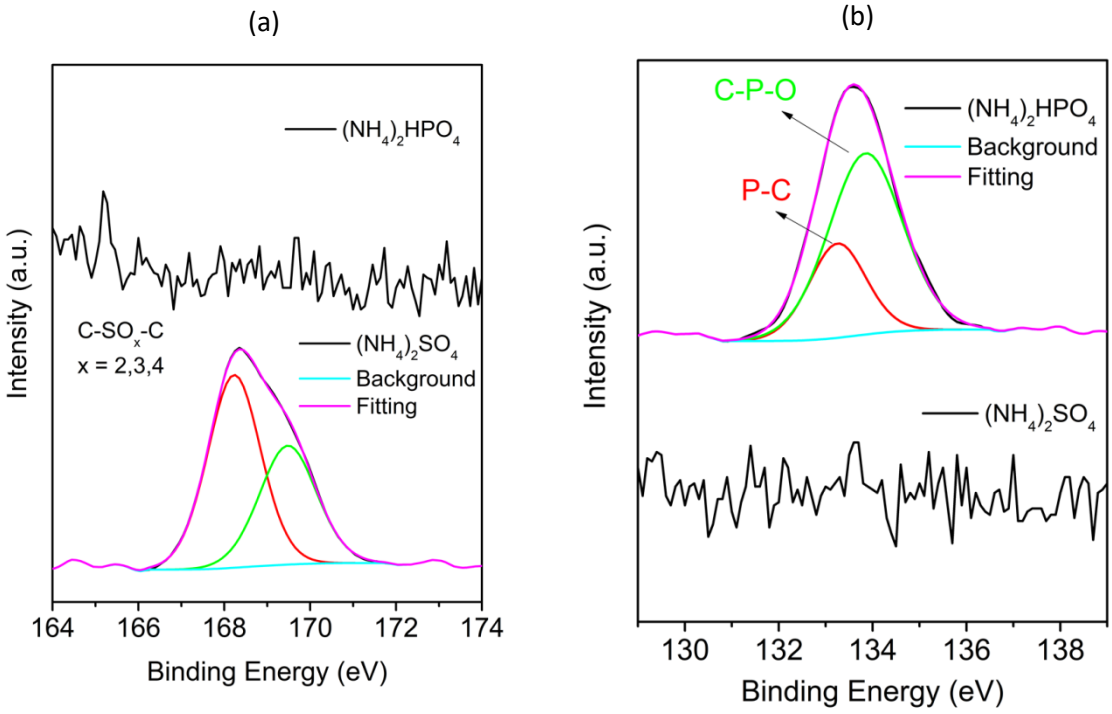


Appendix 6: (a) Sp2 deconvolution (b) P2p deconvolution

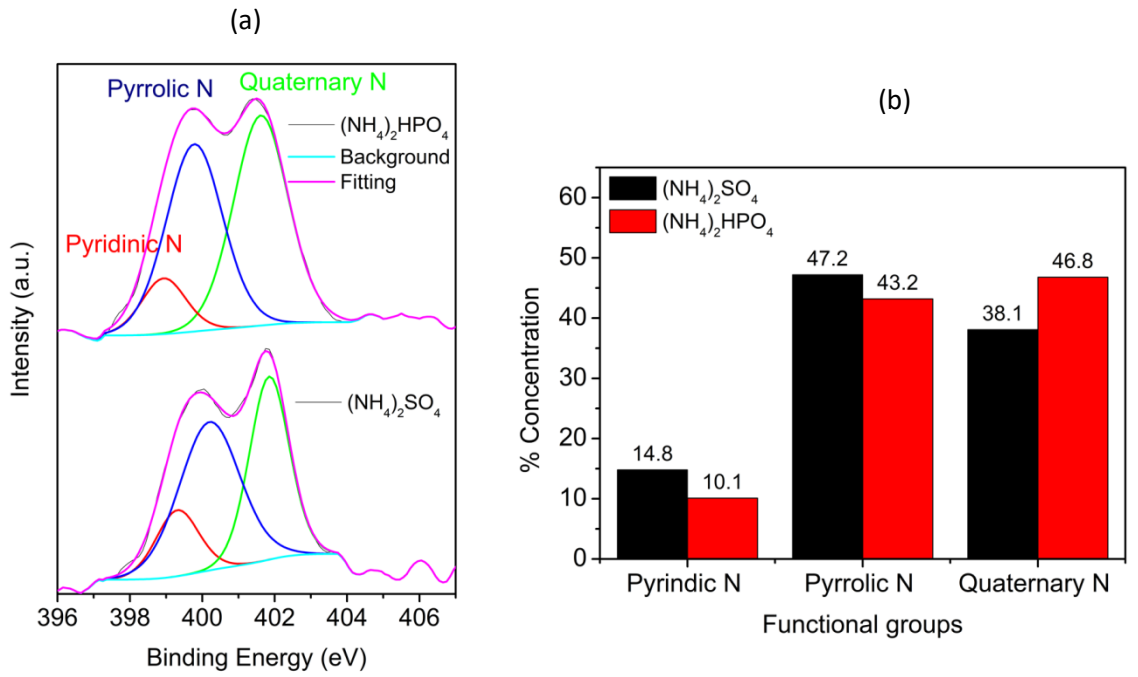


Appendix 7: (a) N1s peak deconvolution (b) functional groups

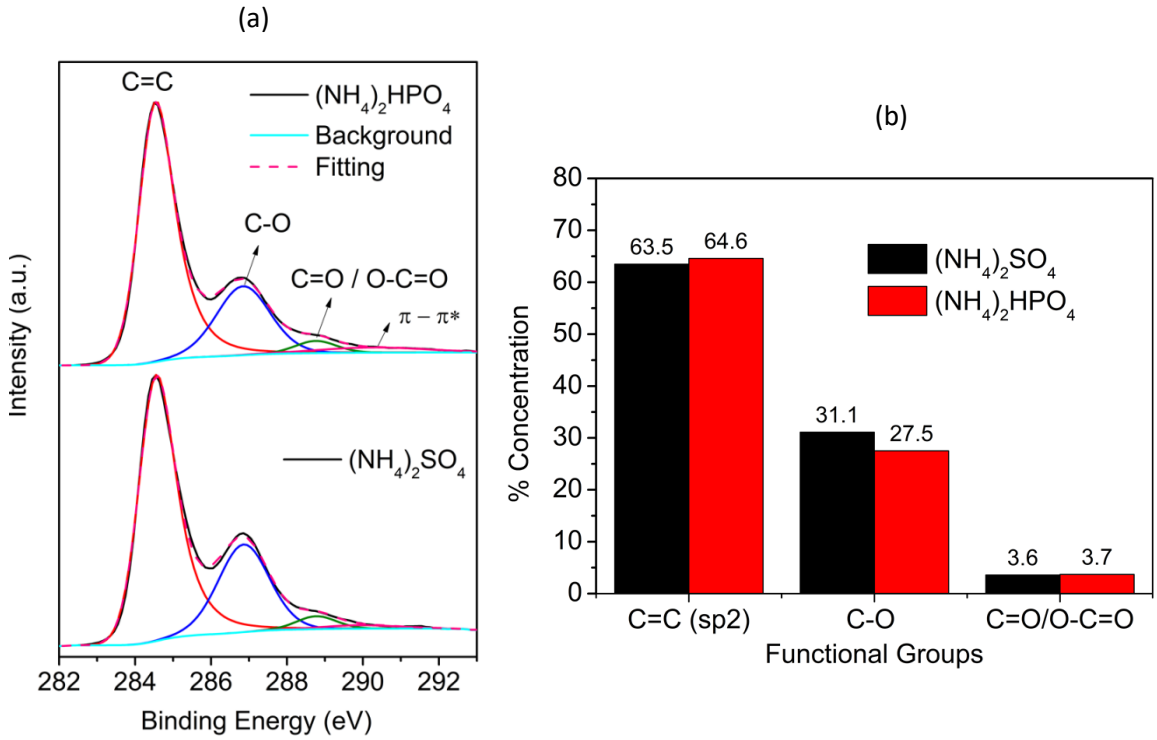


Appendix 8: (a) C1s peak deconvolution (b) functional groups

(a) (b)

Appendix 9: Graphite foil with an exposed surface area of 16 $cm^2$ (a) before exfoliation (b) after exfoliation, incomplete exfoliation of graphite foil.

(a) (b)

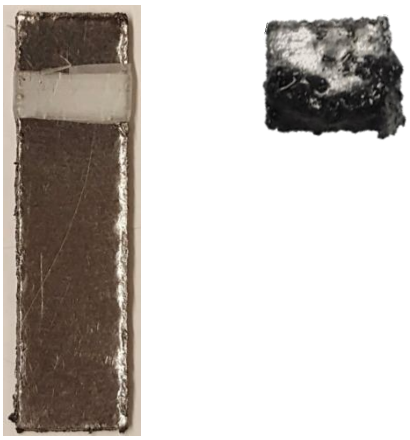

Appendix 10: Graphite foil with an exposed surface area of 4 $cm^2$ (a) before exfoliation (b) after exfoliation.

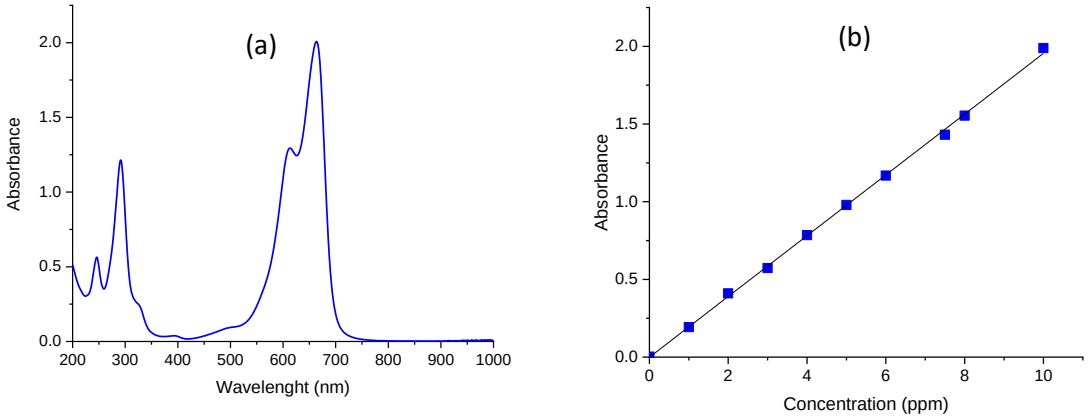


Appendix 11: (a) spectrum of Methylene blue dye (b) calibration curve of methylene blue used for adsorption tests.

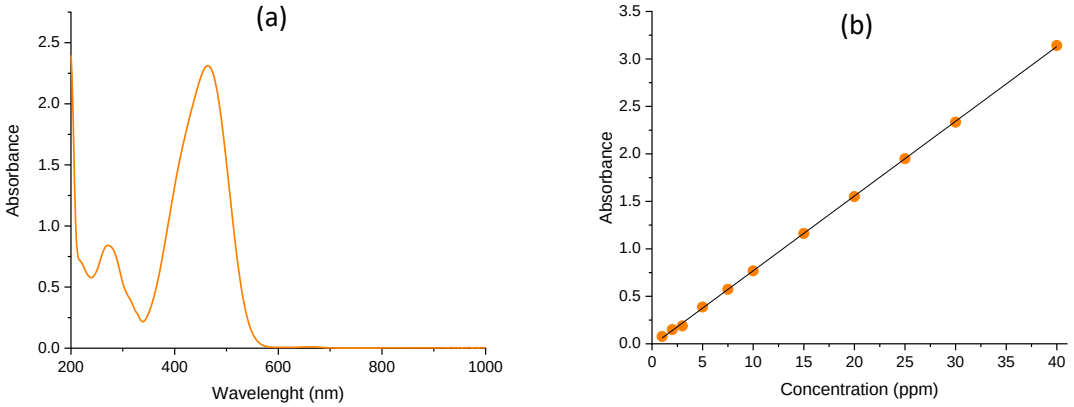


Appendix 12: (a) spectrum of Methyl orange dye (b) calibration curve of Methyl orange used for adsorption tests.

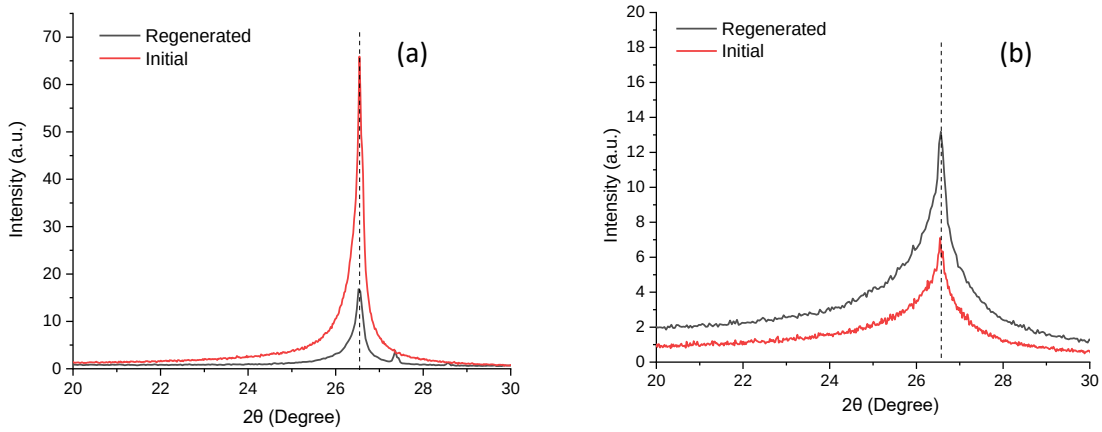


Appendix 13: XRD of (a) EEG-N-S and (b) EEG-N-P before and after adsorption and anodic electrochemical regeneration.

Appendix 14: XRD values of EEG-N-S and EEG-N-P before and after adsorption-regeneration test.

| | Initial Obs. Max* (2θ) | Obs. Max* after regeneration (2θ) | Initial FWHM (2θ) | FWHM after regeneration (2θ) |
|---|---|---|---|---|
| EEG-N-S | 26.547 | 26.544 | 0.204 | 0.212 |
| EEG-N-P | 26.555 | 26.563 | 0.746 | 0.666 |

*Angle corresponding to the maximum intensity

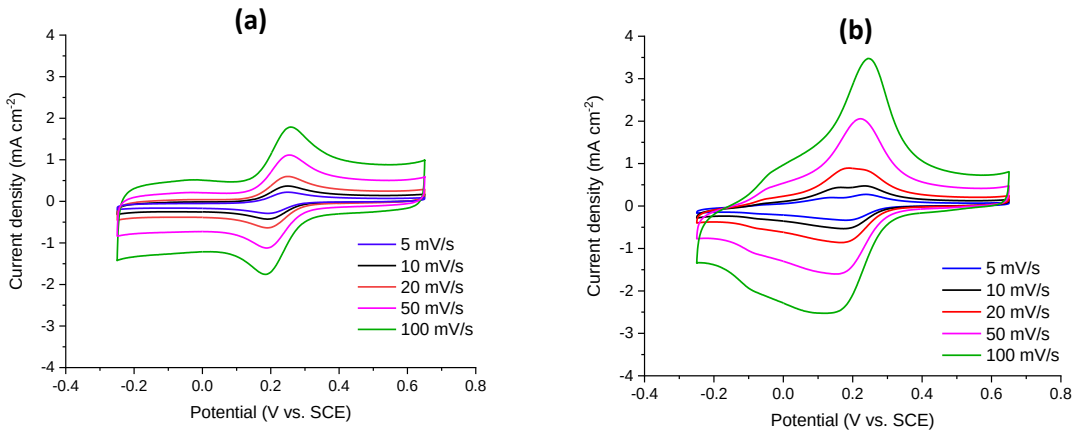


Appendix 15: CV of EEG-N-S (a) before and (b) after accelerated corrosion test in neutral media at different scan rates.

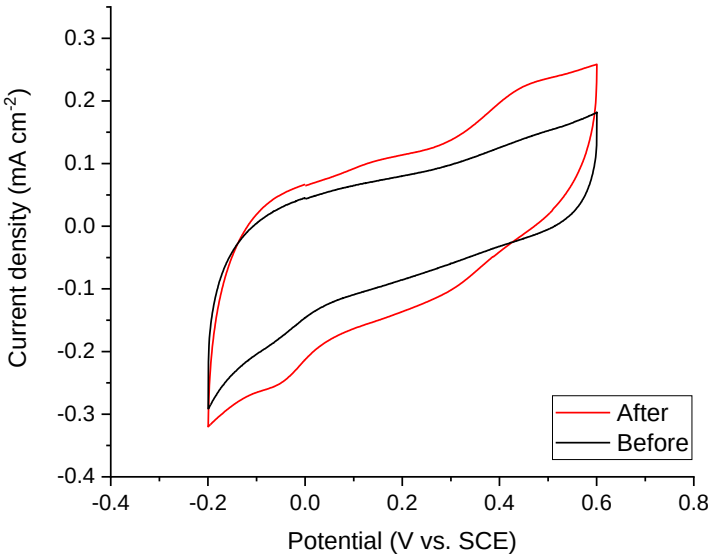


Appendix 16: EEG-N-S before and after accelerated corrosion in 1 M $Na_2SO_4$ at scan rate of 10 mV $s^{-1}$.

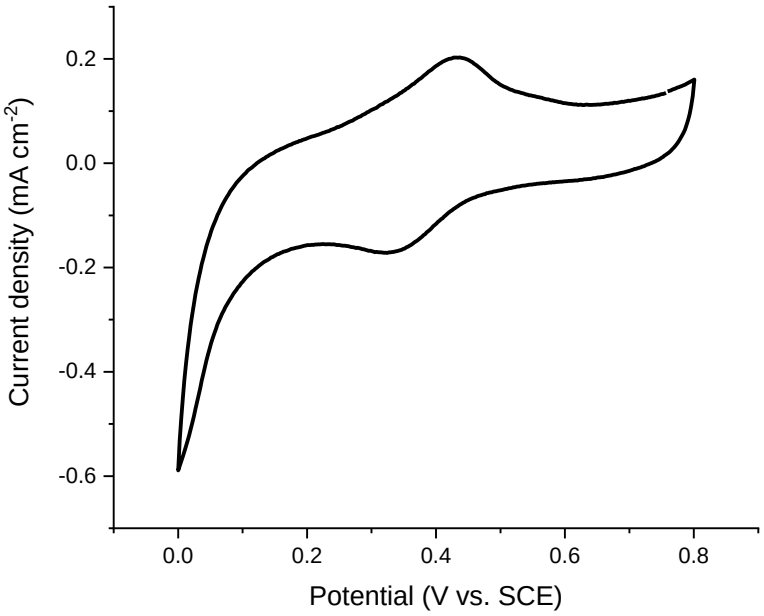


Appendix 17: CV of EEG-N-P in acidic media 0.5 M $H_2SO_4$ with added $K_3Fe(CN)_6$.

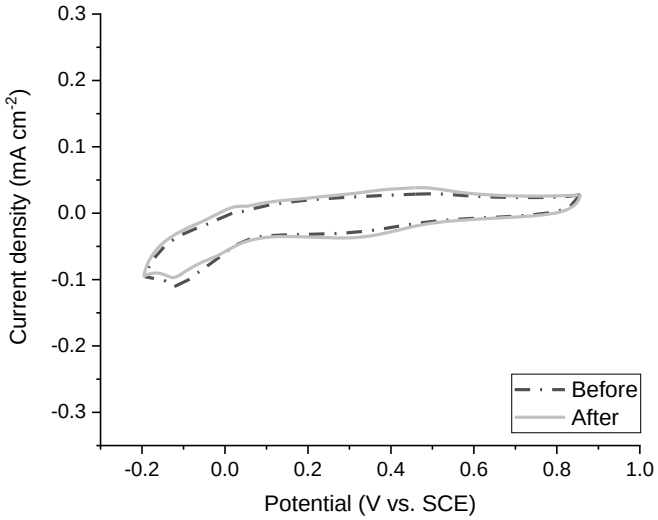


Appendix 18: CV before and after accelerated corrosion test in the absence of graphene, using acidic media 0.5 M $H_2SO_4$ at a scan rate of 10 mV $s^{-1}$.

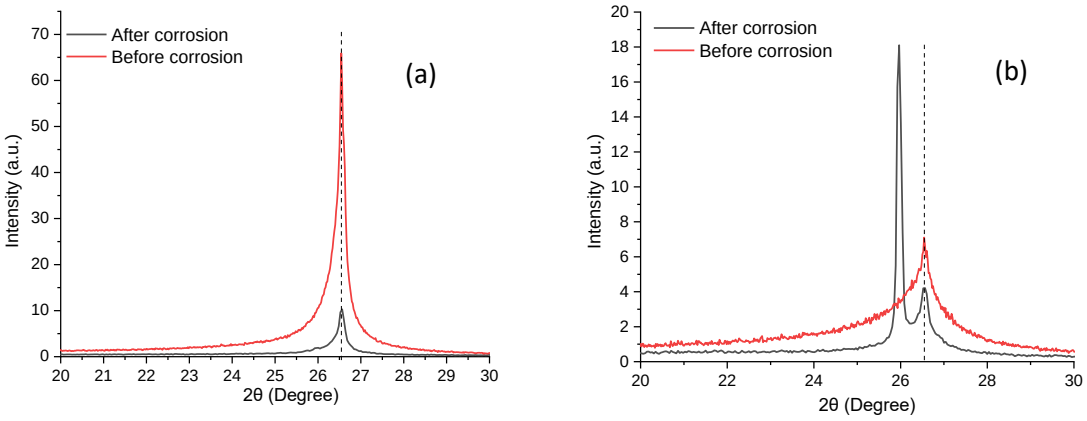


Appendix 19: XRD of (a) EEG-N-S and (b) EEG-N-P before and after corrosion tests.

Appendix 20: XRD values of EEG-N-S and EEG-N-P before and after corrosion tests.

| | Initial Obs. Max* (2θ) | Obs. Max* after corrosion (2θ) | Initial FWHM (2θ) | FWHM after corrosion (2θ) |
|---|---|---|---|---|
| EEG-N-S | 26.547 | 26.556 | 0.204 | 0.197 |
| EEG-N-P | 26.555 | 25.961 | 0.746 | 0.125 |

*Angle corresponding to the maximum intensity

Appendix 21: calculated values of fitted EIS parameters using CNLS fitting method based on the equivalent circuit shown in figure 4.9 (a) after 1: 1 to 6 steps, 2: 7 to 12 and 3: 13 to 18 steps for EEG-N-S exposed to accelerated corrosion.

| Units | $R_1$ Ω | $Q_1$ | $a_1$ | $R_2$ Ω | $Q_2$ | $a_2$ |
|---|---|---|---|---|---|---|
| 1 | 8.645 | 0.4025e-3 | 0.566 | 13.06 | 0.608 6e-3 | 0.783 |
| 2 | 9.446 | 75.86e-6 | 0.754 | 32.65 | 0.621 7e-3 | 0.739 |
| 3 | 9.852 | 45.21e-6 | 0.844 | 167.4 | 0.567 8e-3 | 0.658 |

Appendix 22: calculated values of fitted EIS parameters using CNLS fitting method based on the equivalent circuit shown in figure 4.9 (b) after 1: 1 to 6 steps, 2: 7 to 12 and 3: 13 to 18 steps for EEG-N-P exposed to accelerated corrosion.

| Units | $R_1$ Ω | $Q_1$ | $a_1$ | $R_2$ Ω | $Q_2$ | $a_2$ |
|---|---|---|---|---|---|---|
| 1 | 12.72 | 1.831e-3 | 0.450 | 8.684 | 1.471e-3 | 0.807 |
| 2 | 13.59 | 0.124 6e-3 | 0.713 | 14.88 | 3.264e-3 | 0.684 |
| 3 | 14.03 | 80.07e-6 | 0.795 | 65.21 | 2.374e-3 | 0.624 |

Appendix 23: Capacitance of glassy carbon and EEG samples obtained from CV (–0.2 to 0.85 V vs. SCE, 10 mV $s^{-1}$) before and after corrosion tests by potential steps in 0.5 M $H_sSO_4$.

| Carbon Units | Charge CV Before F | Charge CV After F |
|---|---|---|
| Glassy carbon | 5.84e-4 | 7.07e-4 |
| EEG-N-S | 6.55e-4 | 7.53e-4 |
| EEG-N-P | 8.92e-4 | 1.10e-3 |

Appendix 24: charge passed for glassy carbon, EEG-N-S and EEG- N-P during 18 potential steps between 1.4 and 0.55 V vs. SCE, accelerated corrosion experiments carried out in an acidic solution.

| Carbon Units | Anodic charge C | Cathodic charge C |
|---|---|---|
| Glassy carbon | 0.036 | 0.021 |
| EEG-N-S | 0.084 | 0.068 |
| EEG-N-P | 0.134 | 0.103 |